

1 **Impacts of Lower Thermospheric Atomic Oxygen on**
2 **Thermospheric dynamics and composition using the**
3 **Global Ionosphere Thermosphere Model**

4 **Garima Malhotra ¹, Aaron J. Ridley ¹, Daniel R. Marsh ², Chen Wu ¹, Larry**
5 **J. Paxton ³, Martin G. Mlynczak ⁴**

6 ¹Climate and Space Sciences and Engineering, University of Michigan, Ann Arbor, Michigan, USA.

7 ²National Center for Atmospheric Research, Boulder, Colorado, USA.

8 ³Applied Physics Laboratory, Johns Hopkins University, Laurel, Maryland, USA.

9 ⁴NASA Langley Research Center, Hampton, Virginia, USA.

10 **Key Points:**

- 11 • SABER data shows that O number density between 95-100 km is higher in sum-
12 mer mid-high latitudes, opposite to the MSIS distribution.
- 13 • The atomic oxygen distribution between 95-100 km affects the winds, tempera-
14 ture, composition and dynamics in the middle-upper thermosphere.
- 15 • Correct lower thermospheric specification of atomic oxygen is important in mod-
16 eling space weather and climate.

This is the author manuscript accepted for publication and has undergone full peer review but has not been through the copyediting, typesetting, pagination and proofreading process, which may lead to differences between this version and the [Version of Record](#). Please cite this article as doi: [10.1029/2020JA027877](https://doi.org/10.1029/2020JA027877)

Corresponding author: Garima Malhotra, garimam@umich.edu

Abstract

The exchange of energy between the lower atmosphere and the ionosphere-thermosphere system is not well understood. One of the parameters that is important in the lower thermosphere is atomic oxygen. It has recently been observed that atomic oxygen is higher in summer at ~ 95 km. In this study, we investigate the sensitivity of the upper thermosphere to lower thermospheric atomic oxygen using the Global Ionosphere Thermosphere Model (GITM). We use the Whole Atmosphere Community Climate Model with thermosphere and ionosphere extension (WACCM-X) to drive the lower atmospheric boundary of atomic oxygen in GITM between ~ 95 - 100 km and compare the results with the current Mass Spectrometer Incoherent Scatter (MSIS) driven GITM. MSIS has higher atomic oxygen in the winter hemisphere while WACCM-X has higher atomic oxygen in the summer hemisphere. The reversal of atomic oxygen distribution affects the pressure distribution between 100-120 km, such that the hemisphere with larger O number density has stronger equatorward winds, and lower temperature mainly due to adiabatic and radiative cooling. This affects thermospheric scale heights such that the hemisphere with more O has lower N_2 and thus enhanced O/N_2 . This behavior is observed in the opposite hemisphere when MSIS is used as the lower boundary for GITM. Overall, O/N_2 for WACCM-X driven GITM matches better with the Global Ultraviolet Imager (GUVI) data. We find that the impact of lower thermospheric atomic oxygen on upper thermosphere is not just through diffusive equilibrium, but also through secondary effects on winds and temperature.

1 Introduction

The coupling between the lower atmosphere and the ionosphere-thermosphere (IT) system remains one of the biggest challenges in understanding and observing space weather. Numerous studies have been conducted over the past few decades to understand the dynamical and compositional changes in the IT densities and temperature because of the lower atmosphere (e.g., Shimazaki, 1967, 1968; Hagan & Forbes, 2002; Immel et al., 2006; X. Zhang et al., 2010a, 2010b; Malhotra et al., 2016, and many others). The vertical coupling via gravity waves, planetary waves and atmospheric tides plays a crucial role in the momentum, energetics and composition of the IT system (Lindzen, 1981; Qian et al., 2009; Yamazaki & Richmond, 2013; Siskind et al., 2014). Because most space-based activities are in the thermosphere/ionosphere of either Earth or other planets, it is imperative to understand the physical processes affecting this region of the atmosphere. For example, ionospheric irregularities impacting communication systems (e.g., Kelly et al., 2014), such as equatorial bubbles, are thought to be seeded from the lower and middle atmosphere (Rottger, 1973; Hysell et al., 1990; Prakash, 1999).

In order to better understand how the lower atmospheric variability at various spatial and temporal scales propagates into the upper atmosphere, attempts have been made to develop whole atmosphere models, such as, the Whole Atmosphere Community Climate Model with Thermosphere and Ionosphere Extension (WACCM-X) (H.-L. Liu et al., 2018), the Ground to topside model of Atmosphere and Ionosphere for Aeronomy (GAIA) (Jin et al., 2011), the Whole Atmosphere Model (WAM) (Akmaev et al., 2008; Fuller-Rowell et al., 2008), and the Canadian Middle Atmosphere Model (CMAM) (Beagley et al., 1997). Apart from seamless atmospheric modeling, another approach to better understanding the lower atmospheric influences in the IT system is by coupling a lower atmosphere model with an IT/upper atmospheric model (e.g., Roble, 2013; Akmaev, 2011). While whole atmosphere models are more self-consistent, coupled models are better suited for isolating the effects of specific lower boundary conditions on the upper atmosphere (e.g., Hagan et al., 2009; Q. Wu et al., 2012).

For upper atmospheric models, lower boundary conditions are especially important for introducing compositional changes in the IT system, as the composition at 100-130

68 km map to higher altitudes because of diffusive equilibrium (Colegrove et al., 1966). Major
69 constituents in the MLT are atomic oxygen (O), molecular nitrogen (N₂), and molec-
70 ular oxygen (O₂). Between the altitudes 80-100 km, the lifetime of O changes from hours
71 to several months and therefore O in the lower thermosphere becomes highly suscepti-
72 ble to dynamical transport by winds (Brasseur & Solomon, 1984; Smith et al., 2010). Changes
73 in O concentration in this region map to total neutral densities at higher altitudes in the
74 thermosphere as O becomes the major species above 200 km. It is also known that the
75 electron density in the F region ionosphere is approximately proportional to O/N₂ be-
76 cause O acts as a source of free electrons while N₂ acts as the sink (Shimazaki, 1965, 1966).

77 In the upper thermosphere, a hemispheric asymmetry in the distribution of species
78 is observed in solstice conditions. Higher concentrations of lighter species, for example,
79 O and He are observed in the winter hemisphere, also called the 'winter bulge', whereas
80 heavier species (e.g., O₂ and N₂) are concentrated in the summer hemisphere (e.g., John-
81 son, 1964; King, 1964; Keating & Prior, 1968; Reber et al., 1968; Johnson & Gottlieb,
82 1970, 1973; Johnson, 1973; Mayr et al., 1978). Two processes that are thought to be re-
83 sponsible for this redistribution are horizontal transport across the hemispheres and ver-
84 tical transport. In the thermosphere, meridional wind circulation is dominated by in-
85 terhemispheric winds from summer to winter due to the temperature gradient arising
86 from asymmetrical solar heating between the hemispheres. Numerous studies (Mayr et
87 al., 1978; Cageao & Kerr, 1984) have put forward the horizontal transport of O into the
88 winter hemisphere by the meridional winds as the primary reason for the winter bulge.
89 In the middle thermosphere, the vertical winds in the summer are largely upward whereas
90 the vertical winds in the winter hemisphere are downward. This causes vertical trans-
91 port of the species such that in the summer hemisphere, upward winds result in decrease
92 of lighter species and increase of heavier species (Hays et al., 1973; Reber & Hays, 1973;
93 Burns et al., 1989; Rishbeth, 1998; X. Liu et al., 2014; Jones Jr. et al., 2018). The op-
94 posite happens in the winter hemisphere resulting in a relative increase of lighter species
95 and decrease of heavier species. The importance of one mechanism versus the other (i.e.,
96 horizontal vs vertical transport) is still under investigation. Fuller-Rowell (1998) linked
97 the two mechanisms by describing the mixing to be similar to a huge eddy, calling it the
98 'thermospheric spoon'. Sutton (2016) found that both phenomena are inherently linked
99 with one another with convergent horizontal motion increasing downwelling and diver-
100 gent motion increasing upwelling, thereby transporting light constituents both horizon-
101 tally and vertically simultaneously.

102 In the mesosphere, the meridional circulation is in the same direction, from sum-
103 mer to winter, but driven by a different mechanism. Large westward gravity wave drag
104 in the winter hemisphere and eastward gravity wave drag in the summer hemisphere causes
105 the circulation to be from summer to winter through Coriolis force (Qian & Yue, 2017).
106 Smith et al. (2010) used O mixing ratio at 0.0046 hPa (~84 km) from the Sounding of
107 the Atmosphere using Broadband Emission Radiometry (SABER) instrument to show
108 that there is a winter maximum in O which is likely linked to the above mentioned grav-
109 ity wave driven downwelling in the winter. However, they observed the opposite hemi-
110 spheric distribution at a lower pressure, 0.0008 hPa (~94 km) with higher O mixing ra-
111 tio in the summer hemisphere and lower in the winter hemisphere. The greatest vari-
112 ation was found to be at mid-latitudes with the phase of mid-latitude variation revers-
113 ing between 84 and 94 km. The level of reversal was found to be at 0.001 hPa (~93 km).
114 The higher summer atomic oxygen concentration may be an indication that the sum-
115 mer upwelling circulation cell has reversed and there is a downward circulation cell above
116 the mesopause (~ 83-89 km) (Smith et al., 2010). Another reason may be enhanced molec-
117 ular diffusion of O due to higher temperatures from higher altitudes (Smith et al., 2010).
118 A similar reversal was also observed by Russell et al. (2004) using Wind Imaging Inter-
119 ferometer (WINDII) data and Sheese et al. (2011) using Optical Spectrograph and In-
120 frared Imaging System (OSIRIS) data. Qian et al. (2017) found evidence of lower ther-
121 mospheric winter to summer circulation using WACCM-X and SABER CO₂ data cit-

ing convergence in summer and divergence in winter about 10 km above the mesopause. It was explained to be forced by gravity waves (Lindzen, 1981; Rezac et al., 2015; Smith et al., 2011; H.-L. Liu, 2007). It is possible that this circulation is responsible for the distribution of atomic oxygen observed by Smith et al. (2010). Qian and Yue (2017) studied the impact of the lower thermospheric winter-to-summer circulation on the upper thermosphere by forcing the meridional and vertical winds of the NCAR Thermosphere-Ionosphere-Electrodynamics General Circulation Model (TIE-GCM) (Richmond et al., 1992; Qian et al., 2014, and references therein) in the altitude range of ~ 97 -110 km towards a winter-to-summer circulation. They found that upwelling decreases the upper-thermospheric O/N₂ in the winter hemisphere, whereas, downwelling increases it in the summer hemisphere, thus reducing the gradient between the two hemispheres.

This study reports the impact of changing the distribution of the lower thermospheric atomic oxygen on the upper thermosphere. This is done by changing the lower boundary condition for atomic oxygen in the Global Ionosphere Thermosphere Model (GITM) from an empirical model (MSIS) to a whole atmosphere model (WACCM-X). MSIS and WACCM-X have oppositely oriented atomic oxygen distributions in latitude, with WACCM-X having a distribution that is more consistent with observations. This is done while keeping other species' number densities, temperature, winds constant at the model lower boundary. This is different from Qian and Yue (2017) because our goal is to explain the mechanisms that are involved in lower-upper thermospheric coupling in the context of lower thermospheric O concentration rather than the winter-to-summer circulation.

2 Methodology

2.1 Models

2.1.1 Global Ionosphere Thermosphere Model (GITM)

GITM is a physics based three-dimensional spherical model that simulates the thermosphere and ionosphere by determining the density, momentum, and energy self-consistently (Ridley et al., 2006). GITM explicitly solves for the neutral densities of O, O₂, N(²D), N(²P), N(⁴S), N₂, NO and He; and ion species O⁺(⁴S), O⁺(²D), O⁺(²P), O₂⁺, N⁺, N₂⁺, NO⁺ and He⁺. It uses a stretched altitude grid from 100 km to 600 km that allows for non hydrostatic conditions to exist (Deng et al., 2008). The vertical grid spacing is less than 3 km in the lower thermosphere, and over 10 km in the upper thermosphere. It allows different models of high-latitude electric fields, auroral particle precipitation, and solar EUV inputs to be used. Here, we use the Weimer model, (Weimer, 2005) for the high latitude potential, FISM EUV empirical model, (Chamberlin et al., 2008) and NOAA POES Hemispheric Power driven model (Fuller-Rowell & Evans, 1987) as an estimate of power deposited in the polar regions by energetic particles.

2.1.2 Mass Spectrometer and Incoherent Scatter radar (MSIS)

In its default configuration, GITM uses the Mass Spectrometer and Incoherent Scatter radar model, NRLMSISE-00 (Hedin, 1983, 1987, 1991; Picone et al., 2002) as the thermospheric lower boundary condition on the number densities and temperature. NRLMSISE-00 is an empirical model that uses Fourier-modulated spherical harmonics in latitude, longitude, and time, and Bates-Walker (Walker, 1965) and cubic spline fits in the vertical to numerous satellite, ground based and rocket observations. NRLMSISE-00 has been widely used to understand vertical coupling between the lower atmosphere and the IT system (Fuller-Rowell, 1998; H. Liu et al., 2010; Qian et al., 2018; Weimer et al., 2018; Yue et al., 2019). Since it is an empirical model, it gives a good estimate of neutral densities and temperature for average conditions where observations exist. The inputs to MSIS are the solar flux proxy, F10.7 and geomagnetic activity level (Ap).

2.1.3 Whole Atmosphere Community Climate Model with Thermosphere and Ionosphere extension (WACCM-X)

WACCM-X is also a physics based model, covering the whole atmosphere starting from the surface to 2.5×10^{-9} hPa or ~ 500 km in altitude (H. Liu et al., 2010; H.-L. Liu et al., 2018). It is based on the NCAR Whole Atmosphere Community Climate Model (WACCM) (Garcia et al., 2007; Marsh et al., 2013), which in turn is based on the NCAR Community Atmosphere Model (CAM) (S.-J. Lin, 2004). In this study, we use the Specified Dynamics configuration of WACCM-X, also known as SD-WACCM-X. In this configuration, dynamical fields (temperature, zonal and meridional winds and surface pressure) are specified in the troposphere and stratosphere from the Modern Era Retrospective Analysis for Research and Applications (MERRA) (Rienecker et al., 2011). WACCM-X can also be run without constraining the troposphere and stratosphere, also usually referred to as the free-running mode. Since we are only using the results from SD-WACCM-X here, we will refer to these simulations as WACCM-X. The horizontal resolution (latitude \times longitude) of the model is $1.9^\circ \times 2.5^\circ$, and the time step is 5 minutes. A detailed description of WACCM-X is given in H. Liu et al. (2010) and H.-L. Liu et al. (2018). Hourly averaged values are used in our study. WACCM-X is used as the lower boundary for GITM and the simulation results are compared with MSIS driven GITM. The version of Community Earth System Model (CESM) that is used in this study is 2.0.

WACCM-X solves the Navier Stokes equations in pressure coordinates whereas GITM solves them in altitude coordinates. WACCM-X outputs the mixing ratio for different species, whereas GITM uses number densities as boundary conditions. Therefore, the total neutral number density in WACCM-X is calculated from pressure and temperature fields (using the ideal gas law). WACCM-X also outputs the altitude corresponding to each pressure level at every grid cell. The total number densities and atomic oxygen mixing ratio in pressure coordinates are converted to altitude coordinates by linearly interpolating them to 95 km, 97.5 km and 100 km, thus putting them on a uniform altitude grid. The total number density is multiplied by the mixing ratio of atomic oxygen (also in altitude coordinates) to get number densities for atomic oxygen on the altitude grid.

2.2 GITM Simulations

Atomic oxygen number densities from MSIS and WACCM-X were used as inputs at the lower boundary of GITM. WACCM-X is expected to have significantly more variability owing to non-migrating tides, planetary waves and gravity waves that propagate through the lower atmosphere to the thermosphere. On the other hand, because MSIS is an empirical model, it should provide a good estimate of average conditions but may not be as accurate in representing the impact of forcing from above (e.g. magnetospheric inputs) or forcing from below (e.g. atmospheric gravity waves). Also, at these altitudes, MSIS has only the mean component and migrating tides with a small dependence on F10.7 and Ap. It should be noted that real time-varying geospace conditions are used as inputs in these simulations.

To specify the lower boundary condition in GITM, two ghost cells below 100 km are used. In these cells, state values are specified. In order to not drive constant acceleration, a hydrostatic solution is used, where the density is set in the cell closest to 100 km (second cell), and the density in the lower cell is derived. In both the simulations, the temperature in both cells and across the globe were held constant at 150 K, while all components of the winds were held to be zero. For O₂, N₂, and NO, the number densities in the second cell are constant across the globe and specified in Table 1. For the minor species, He and N(⁴S), MSIS is used to specify the number densities in both the simulations. For O, a zero gradient in altitude is used since O peaks in this region. There-

222 fore, the O number densities in the first cell are same as in the second cell. O is allowed
223 to have horizontal structure, such that, for the GITM w/ MSIS simulation, MSIS is used
224 to specify the O number densities, whereas, for the GITM w/ WACCM-X simulation,
225 the above mentioned linearly interpolated O number densities are used.

226 Hourly averaged WACCM-X O number densities are used. Since the timesteps in
227 GITM are much smaller than the 1 hour time resolution of WACCM-X output, WACCM-
228 X number densities are linearly interpolated in time between every hour. These num-
229 ber densities are linearly interpolated to GITM's second cell's altitude and grid locations.
230 MSIS O number density is computed at each GITM time step and location. The only
231 difference between the two runs, GITM w/ MSIS and GITM w/ WACCM-X is the atomic
232 oxygen between 95 - 100 km. This was specifically done to explore the effect of the O
233 number density in the lower thermosphere on the system.

234 Results from the two simulations spanning 21 days, Jan 15, 2010 to Feb 04, 2010
235 are discussed here. Since, it took around 9 days for the model to achieve a nearly steady
236 globally averaged O density at 200 km altitude, results from the last 12 days, Jan 24,
237 2010 to Feb 04, 2010 are discussed. The two simulations are referred to as GITM w/ MSIS
238 and GITM w/ WACCM-X. This time period is chosen because it is a geomagnetically
239 quiet time around solstice that results in a hemispherically asymmetric lower thermo-
240 spheric O number density between MSIS and WACCM-X. Simulations results from June
241 24, 2010 to July 5, 2010 are also discussed here.

242 **2.3 Data**

243 In this study, SABER data is used to validate the lower thermospheric atomic oxy-
244 gen in WACCM-X. We also use GUVI O/N₂ to validate the integrated thermospheric
245 O/N₂ in GITM once the lower boundary atomic oxygen is changed from MSIS to WACCM-
246 X. A brief description of the SABER and GUVI instruments is provided below for the
247 interested reader.

248 **2.3.1 SABER**

249 Sounding of the Atmosphere using Broadband Emission Radiometry (SABER) is
250 an instrument on Thermosphere-Ionosphere-Mesosphere Energetics and Dynamics (TIMED)
251 satellite. Its primary goal is to quantify the energy budget of mesosphere and lower ther-
252 mospheric (MLT) (Mlynczak, 1996, 1997). TIMED was launched in 2001 in a 74.1° in-
253 clination orbit at an altitude of 630 km (Russell III et al., 1999; Yee, 2003). It has a yaw
254 period of ~60 days in which the latitudinal coverage alternates between 82°N - 53°S and
255 53°N - 82°S. SABER has a vertical resolution of ~2 km and horizontal resolution of ~300
256 km depending on the limb geometry. SABER takes limb scan profiles of 10 spectral chan-
257 nels between 1.27 - 17μm, indicating the kinetic temperature of O and CO₂ in the MLT
258 region (~65-105 km) (Rezac et al., 2015).

259 O is generated by photodissociation of molecular oxygen by solar UV radiation and
260 has two very bright fine structure lines, 63.184 μm (4.75 THz) and 145.525 μm (2.06 THz).
261 However, both of these wavelengths are particularly hard to measure with the current
262 state-of-the-art satellites instruments. Past and present technologies require a detection
263 system cooled to cryogenic 4K temperatures, which poses a significant mission cost and
264 lifetime overhead. D. L. Wu et al. (2016) described an emerging technique, THz limb sounder
265 (TLS) using a Schottky-diode-based receiver which has good radiometric sensitivity at
266 non-cryogenic temperature. Studies over the last few decades have used balloons (F. J. Lin
267 et al., 1987; Mlynczak et al., 2004), rocket borne in-situ observations (von Zahn, 1967;
268 Offermann, 1974; K. Grossmann & Offermann, 1978; Gumbel, 1997) and space station
269 observations (K. U. Grossmann et al., 2000). Since there are no global observations made
270 by observing radiant emission of O directly, SABER calculates O using indirect meth-

ods (Mlynczak, 1996, 1997; Rezac et al., 2015). During the daytime, O is derived using the emission of ozone (O_3) at $9.6 \mu\text{m}$ assuming that there is an equilibrium between the photolysis of O_3 and the recombination of O and O_2 . During night, it is inferred from the emission of the vibrationally excited Meinel OH band, which is formed by the reaction between atomic hydrogen (H) and O_3 . This measurement assumes that there is an equilibrium between this reaction and the recombination of O and O_2 (Mlynczak et al., 2013, 2018).

2.3.2 GUVI

The Global Ultraviolet Imager (GUVI) is an FUV hyperspectral imager aboard the TIMED satellite, measuring the terrestrial airglow from 120 to 180 nm (Christensen et al., 2003). Some of the objectives of GUVI are to make accurate observations of thermospheric temperature and composition and to understand the response of thermosphere ionosphere system to various energy fluxes. It measures in five far ultraviolet bands corresponding to emission features of H (121.6), OI(130.4), OI(135.6), and the N_2 LBH bands (Christensen et al., 1994; Paxton et al., 1999; Christensen et al., 2003). In the imaging mode, a scan mirror subsystem (Humm et al., 1998, 1999) scans the instantaneous field of view cross-track of the satellite once every 15s. The scan begins on the limb and covers 140° , i.e., 80° from nadir above the limb on the cold side of the satellite (away from the Sun) to 60° toward the warm side (Paxton et al., 2004). Since December 2007 when the scan mirror failed, GUVI only operates in the spectral stare mode at about 47° from nadir. In this mode, data are recorded continuously from all 176 spectral pixels for each of the 14 spatial pixels (Meier et al., 2014). The height integrated O/ N_2 ratio referenced at a N_2 column integrated number density of 10^{17} cm^{-2} is obtained from the disk 135.6 nm and LBHS day glow data (Y. Zhang et al., 2004, 2014).

3 Results and Discussion

3.1 Lower Boundary Comparison

Figure 1 shows a comparison between atomic oxygen number densities of GITM w/ MSIS (Figure 1a) and GITM w/ WACCM-X (Figure 1b) at 100 km, averaged over the last 12 days of the simulation. For GITM w/ MSIS, O is higher in the northern winter whereas for GITM w/ WACCM-X, O is higher in the southern summer. Figure 1c shows the difference between panels b) and a) i.e., GITM w/ WACCM-X - GITM w/ MSIS. The absolute difference is larger in the summer hemisphere.

In order to determine which simulation result is closer to the observed O distribution, Figure 2a shows SABER atomic oxygen number densities at 100 km gridded in $4^\circ \times 4^\circ$ bins, averaged for January from 2002-2017. Figure 2b shows the number of measurements in each bin. The high latitudes have lower numbers of measurements compared to middle-lower latitudes, because of the inclination of TIMED satellite. Long term averaging is helpful in reducing the uncertainty associated with the decrease in abundance of daytime ozone due to photolysis. The atomic oxygen number densities are larger in the summer (southern) hemisphere which is similar to Figure 1b for GITM w/ WACCM-X. The summer hemisphere number density maximum is at different latitudes, with the SABER maximum occurring at higher latitudes than the WACCM-X maximum. Because of the lower number of SABER measurements at high summer latitudes, there is a greater statistical uncertainty associated with the measurements. Another source of uncertainty is the accuracy of the temperature at 100 km, through the recombination rate coefficient in the steady-state chemical expression used to derive atomic oxygen from ozone (Mlynczak et al., 2013). Lastly, SABER daytime ozone has a likely high bias as reported by Smith et al. (2013). Thus, the absolute magnitude of SABER data is different from both MSIS and WACCM-X. SABER values are ~ 3 times the model values, resulting in a larger gradient between the hemispheres. Using WACCM-X O number densities as an approxi-

321 mation for the true O number density distribution, this study focuses on explaining the
322 large-scale effects of the O number density distribution at the mesopause on the ther-
323 mosphere.

324 As an aside, MSIS was developed using data from a wide variety of in-situ satel-
325 lite measurements in the upper thermosphere (Hedin, 1987, 1991; Picone et al., 2002) and
326 did not include measurements of O in this region. At around 100 km, a hemispheric gra-
327 dient in the atomic oxygen number density in MSIS is predicted, with lower O number
328 density in the summer hemisphere, similar to the observations in the middle-upper ther-
329 mosphere (Reber & Hays, 1973). However, in the region between 90 - 150 km, limited
330 observations were available, primarily being temperature and total neutral density mea-
331 surements inferred from rockets and incoherent scatter radars. NRLMSISE-00 did not
332 include the SABER measurements in its fitting procedure because TIMED hadn't been
333 launched yet. In MSIS, below the turbopause (~ 105 km), the number densities were ex-
334 trapolated using the average molecular weight of the atmosphere assuming a perfectly
335 mixed atmosphere along with a correction factor to account for chemical and dynam-
336 ical flow effects on various species. Below the turbopause, these chemical dynamical cor-
337 rection factors imply that the atmosphere is not fully mixed until ~ 80 km or lower. Be-
338 tween 120 km and 105 km, the number densities are a meld of their fully mixed and dif-
339 fusively separated values along with the correction factor. The correction factor for O
340 does not take into account the dynamical/chemical effects that lead to larger summer
341 atomic oxygen, thus explaining the similar hemispheric gradient of atomic oxygen num-
342 ber density in the upper as well as the lower thermosphere.

343 However, O departs from diffusive and fully mixed equilibrium in the mesosphere
344 and lower thermosphere due to chemistry, eddy mixing and dynamic transport, which
345 is highlighted by the incorrect O distribution in MSIS, as compared to both WACCM-
346 X results and SABER observations. One of the reasons for the O reversal in SABER data
347 is suggested by Smith et al. (2010) through the effect of temperature and molecular dif-
348 fusion. Higher temperatures in the summer hemisphere may lead to molecular diffusion
349 of O from higher to lower altitudes resulting in high O concentration. The transport of
350 O via lower thermosphere winter to summer circulation suggested by Qian and Yue (2017)
351 and Rezac et al. (2015) may also be the reason for this reversal. Another contribution
352 to high summer O can be from the eddy turbulence or eddy diffusion. Eddy diffusion
353 is a macroscopic description of flow induced by the gravity wave motion (Hodges, 1969).
354 However, previous studies suggest that other tidal and wave activity can contribute to
355 the mixing and turbulence in this region (Salinas et al., 2016; Jones Jr. et al., 2017). Nu-
356 merous observational (e.g., Fukao et al., 1994; Kirchhoff & Clemesha, 1983; Sasi & Vi-
357 jayan, 2001) and modeling studies (e.g., Qian et al., 2009; Pilinski & Crowley, 2015; Sali-
358 nas et al., 2016) have found that eddy diffusion coefficient is larger in summer and smaller
359 in winter. However, the exact magnitude of the eddy diffusion term near the turbopause
360 still remains elusive. We have yet to achieve a universal model for specifying the eddy
361 diffusion coefficient. It is possible that larger eddy diffusion during summer leads to down-
362 ward transport of O into the lower thermosphere resulting in the increase of summer O/N₂.

363 3.2 Effect on Lower - Upper Thermosphere

364 Figure 3 shows GITM zonally averaged meridional winds in the thermosphere from
365 100 km to 275 km. Figure 3a and 3b are the winds for GITM w/ MSIS and GITM w/
366 WACCM-X, respectively. Winds vectors comprising of both vertical (scaled by 50) and
367 meridional winds components are overlaid on the contour plots. The general circulation
368 remains similar between the two simulations. Between 100 - 120 km, winds are equator-
369 ward and above 160 km the circulation is dominated by summer to winter winds with
370 upwelling in summer and downwelling in winter at mid-high latitudes.

Figure 3c is the difference between the zonally averaged meridional winds, GITM w/ WACCM-X - GITM w/ MSIS. As mentioned previously, the only difference between the two simulations is the atomic oxygen distribution below 100 km. The difference in Figure 3c is positive in the region between 100-120 km. This indicates that GITM w/ WACCM-X has larger equatorward winds in the summer (southern) hemisphere, whereas GITM w/ MSIS has larger equatorward winds in the winter (northern) hemisphere. This is because of the difference in latitudinal O number density gradient between the two simulations such that, the winds induced by the lower boundary O gradient superimpose on the main equatorward circulation cells. Thus, because of the opposite O distribution, the hemisphere with larger equatorward winds simply reverses.

The forces affecting the winds in the thermosphere can be understood by investigating the contribution of force terms of the horizontal momentum equation. The northward momentum equation in GITM is as follows (Ridley et al., 2006):

$$\frac{\partial u_\theta}{\partial t} = -u_r \frac{\partial u_\theta}{\partial r} - \frac{u_\theta}{r} \frac{\partial u_\theta}{\partial \theta} - \frac{u_\phi}{r \cos \theta} \frac{\partial u_\theta}{\partial \phi} - \frac{k_b}{\bar{m}_n r} \frac{\partial T}{\partial \theta} - \frac{T}{r \rho} \frac{k_b}{\bar{m}_n} \frac{\partial \rho}{\partial \theta} + \frac{\mathcal{F}_\theta}{\rho} - \frac{u_\phi^2 \tan \theta}{r} - \frac{u_\theta u_r}{r} - \Omega^2 r \cos \theta \sin \theta - 2\Omega u_\phi \sin \theta \quad (1)$$

where θ denotes the north latitude, ϕ denotes east longitude, r is the radial distance from the center of the Earth, u is the neutral velocity, Ω is the angular velocity of the planet, k_b is the Boltzmann constant, m_n is the number density weighted average mass, T is the neutral temperature and ρ is the mass density. \mathcal{F}_θ is the force due to ion-neutral friction and viscosity in θ direction. The superscript for each term is for notation purposes only. Terms (1), (2), and (3) on the right represent the advective terms from the total derivative of velocity. Terms (7) and (8) are the velocity terms due to the spherical coordinates. Terms (4) and (5) represent the force arising from pressure gradient. Terms (9) and (10) are the centrifugal and Coriolis force terms, respectively.

Figure 4 shows the zonally and temporally averaged centrifugal (4a), Coriolis (4b), pressure gradient (4c), and ion drag (4d) forces from GITM w/ MSIS. It should be noted that these figures represent the force terms on the right side of equation 1 with the appropriate sign. Clearly, on average, the centrifugal and pressure gradient forces dominate this region of the thermosphere. Below 120 km, near the boundary of the model, the pressure gradient force in Figure 4c is weak owing to a nearly constant boundary condition on number densities (except O), temperatures, and winds. Thus, the two equatorward circulation cells between 100 - 120 km are driven by centrifugal force shown in Figure 4a. In the middle thermosphere, between 125 - 200 km, the winds can develop creating a pressure bulge and can cause a redistribution of the temperature and densities to create oppositely directed forces that cancel the centrifugal force. A more-precise boundary condition on the pressure would have a bulge at the equator, such that the latitudinal gradient in pressure more closely balances the centrifugal force (i.e., an oblate spheroid atmosphere instead of a perfect sphere). We refer to this as the poleward directed pressure gradient force. Above this altitude range, the pressure gradient force is from the summer to winter because of the temperature gradient, driving the main circulation. Coriolis force shown in Figure 4b is weak and acts opposite to the centrifugal force. Ion drag shown in Figure 4b is also weak and has a significant magnitude only above 200 km, where it acts mostly against the main circulation.

Figure 4e shows the difference between the pressure gradient forces of GITM w/ WACCM-X and GITM w/ MSIS. The differences corresponding to other force terms are negligible and are not shown here. Between 100-120 km, a small difference exists between the simulations which can be largely attributed to the density gradient difference. This difference results in the wind differences shown in Figure 3c. GITM w/ WACCM-X (GITM

417 w/ MSIS) has weaker pressure gradient force in the summer (winter) hemisphere. More
418 O at summer high latitudes in GITM w/ WACCM-X weakens the poleward directed pres-
419 sure gradient force which increases the acceleration due to centrifugal force, resulting in
420 stronger winds as compared to GITM w/ MSIS. Similarly, GITM w/ MSIS has weaker
421 poleward directed pressure gradient force and larger acceleration due to centrifugal force
422 in the winter hemisphere. The wind difference between 140 and 200 km altitude will be
423 discussed later. It is important to note that the change in lower boundary O only changes
424 the magnitude of the winds and does not change the direction of the wind. The tran-
425 sition to the upper thermospheric summer to winter circulation starts above 120 km, re-
426 sulting in high atomic oxygen in the winter hemisphere above this altitude in both the
427 simulations. This was also observed by K. U. Grossmann et al. (2000) at an altitude of
428 140 km using CRISTA experiments.

429 Figure 5 shows the zonally averaged temperature for the two simulations. Figures
430 5a and 5b are the temperature plots for GITM w/ MSIS and GITM w/ WACCM-X, re-
431 spectively while 5c is the percent difference between the two. The temperature shows
432 a similar pattern between Figures 5a and 5b. The temperatures are the lowest in the high
433 latitude region in the 100-120 km altitude range. This can be attributed to the adiabatic
434 and advective cooling due to the equatorward circulation cells as shown previously in
435 Figure 3. Above this altitude, there is a sharp increase in the temperature with temper-
436 atures rising up to 1000 K in summer (southern) hemisphere. As seen in Figure 5c, the
437 temperature difference between the two simulations starts at altitudes slightly above 100
438 km. In the summer hemisphere, GITM w/ WACCM-X has a lower temperature, while
439 in the winter hemisphere, GITM w/ MSIS has a lower temperature. The temperature
440 difference is as high as 5% (35 K) in the southern hemisphere. Thus, reversing the O num-
441 ber density distribution at the lower boundary leads to a change in lower thermospheric
442 temperature, i.e., lower thermospheric temperatures occur at latitudes with higher O con-
443 centrations.

444 Figures 6a and 6b show the zonally averaged percent adiabatic heating per day (nor-
445 malized by temperature) for GITM w/ MSIS and GITM w/ WACCM-X, respectively.
446 For both the simulations the overall heating pattern remains similar. In the lower ther-
447 mosphere, between 100-120 km, the high latitudes have adiabatic cooling, and the lower
448 latitudes have adiabatic heating. The reason for this is the equatorward wind cells as
449 mentioned before and shown in Figure 3. Above 125 km, the summer hemisphere expe-
450 riences adiabatic cooling (due to diverging winds), and the winter hemisphere gets warmer
451 (due to converging winds) because of the summer to winter circulation. The difference
452 between the two simulations is shown in Figure 6c. Between 100-120 km, in the sum-
453 mer hemisphere, GITM w/ WACCM-X has more adiabatic cooling because of larger equa-
454 torward winds. Similarly, in the winter hemisphere, GITM w/ MSIS has a tiny bit more
455 adiabatic cooling. Above this altitude region, the adiabatic heating difference shows a
456 roughly similar pattern as the wind difference of Figure 3c. In the summer hemisphere,
457 except at middle-high latitudes, GITM w/ WACCM-X has more adiabatic cooling while
458 in the winter hemisphere, GITM w/ MSIS has more adiabatic cooling. It should be noted
459 that adiabatic heating differences in Figure 6c do not exactly correspond to the temper-
460 ature difference of Figure 5c. This is because of the contribution of other terms of the
461 energy equation.

462 Figures 7a and 7b show the percent difference between the two simulations for ad-
463 vective and radiative heating per day (normalized by temperature), respectively. For both
464 GITM w/ MSIS and GITM w/ WACCM-X, advective heating shows similar heating pat-
465 terns (not shown here), and largely follows the meridional wind patterns of Figure 3. Merid-
466 ional winds in the upper thermosphere advect fluid parcels of higher temperature from
467 summer to winter, resulting in heating in the winter hemisphere, whereas equatorward
468 winds in the lower thermosphere advect fluid parcels of lower temperature from higher
469 latitudes, resulting in cooling at lower latitudes. The difference between the two simu-

470 lations as shown in Figure 7a is small relative to the adiabatic heating differences, and
 471 largely follows the meridional wind differences at mid-latitudes of Figure 3. The radiative
 472 cooling comes from a combination of CO₂ cooling in the 100-120 km altitude range,
 473 NO cooling in the 100-150 km range and O cooling above that. In the summer hemisphere,
 474 GITM w/ WACCM-X has larger O and therefore, less total radiative heating (more cool-
 475 ing), and in the winter hemisphere, GITM w/ MSIS has larger O and thus less radiative
 476 heating. The sum of these three terms, Figures 6c, 7a and 7b largely explains the
 477 temperature difference observed in Figure 5c, as the radiative heating mostly compen-
 478 sates for the anomalous differences (e.g., GITM w/ MSIS has larger adiabatic cooling
 479 in summer mid-high latitudes) in Figure 6c. The contribution of other terms of the energy
 480 equation are analyzed as well (not shown here) : (a) the difference between the two
 481 simulations for auroral heating is negligible in comparison to the above mentioned terms,
 482 (b) chemical heating difference has a significant magnitude and reinforces the temper-
 483 ature differences in Figure 5c, (c) the molecular conduction heating and Joule heating
 484 differences have an opposite distribution as the other terms and mainly contribute in re-
 485 ducing the magnitude of the overall heating difference. The sum of these individual heat-
 486 ing terms do not exactly correspond to the temperature distribution of Figure 5c, indi-
 487 cating the non-linearity of the thermospheric dynamics.

488 Figure 8 shows the mean height profiles of temperature, O, N₂, and O/N₂ sepa-
 489 rated into northern and southern hemispheres averaged poleward of ± 30° latitude. The
 490 red and blue curves are for GITM w/ WACCM-X and GITM w/ MSIS simulations, respec-
 491 tively. Larger differences between the curves exist in the summer (southern) hemi-
 492 sphere for all parameters. Figure 9 shows the percentage difference between the two sim-
 493 ulations for temperature, O, N₂ and the electron density. Figures 8a and 9 show that
 494 the difference in temperature between the two simulations remains roughly constant with
 495 altitude. The effect of the change in temperature on neutral number densities can be un-
 496 derstood using diffusive equilibrium as a rough guide (e.g., Schunk & Nagy, 2009).

$$n_s(z) = n_s(z_o) \times \frac{T_s(z_o)}{T_s(z)} \times e^{-\int_{z_o}^z \frac{(dz')}{H_s}}, \quad (2)$$

$$H_s = \frac{k_B T_s}{m_s g} \quad (3)$$

497 where $n_s(z)$ and $T_s(z)$ are the number density and temperature at altitude z , respec-
 498 tively. $n_s(z_o)$ and $T_s(z_o)$ are the number density and temperature at a reference alti-
 499 tude z_o , respectively. H_s is the scale height for each species and is directly proportional
 500 to temperature, T_s and inversely proportional to the mass of the species, m_s . k_B is the
 501 Boltzmann constant and g is the acceleration due to gravity. We can break equation 2
 502 into two contributing terms, the temperature ratio term, $\frac{T_s(z_o)}{T_s(z)}$ and the scale height term
 503 $e^{-\int_{z_o}^z \frac{(dz')}{H_s}}$ (This is just for nomenclature; the scale height term depends on temperature
 504 too).

505 For N₂ (assuming z_o to be at 100 km), number densities are the same between the
 506 two simulations at 100 km ($n_s(z_o)$) and the entire difference arises because of different
 507 distributions of O at the boundary. The temperature at the lower boundary ($T_s(z_o)$) is
 508 also the same between the simulations. In the southern hemisphere, GITM w/ WACCM-
 509 X has lower temperature ($T_s(z)$) (Figure 5) resulting in larger temperature ratio term,
 510 causing an increase in N₂ number densities. Whereas, the scale height term is smaller
 511 causing a decrease in N₂ number densities. The effect of these two terms cancel each other
 512 and as a result, the difference in N₂ number densities between the two simulations is small
 513 in the lower thermosphere. In the upper thermosphere, the difference in the tempera-
 514 ture ratio terms between the simulations remains the same, while the difference in the
 515 scale height terms becomes larger because of the integrated effect of exponential. As a

516 result, N_2 decreases faster for GITM w/ WACCM-X in the southern hemisphere, because
 517 of lower temperature and smaller scale height. Therefore, the difference in N_2 between
 518 the two simulations increases with height as seen in Figure 9. The percentage difference
 519 of N_2 reaches about $\sim 10\%$ in the northern hemisphere and $\sim 30\%$ in the southern hemi-
 520 sphere.

521 For the atomic oxygen profile in Figure 8b, the lower boundary number density term
 522 ($n_s(z_o)$) is important because the two simulations have different O at the lower bound-
 523 ary. The difference is as large as $\sim 50\%$ at 100 km as seen in Figure 9. Moreover, the con-
 524 tribution of the temperature ratio term reinforces the difference in $n_s(z_o)$ between the
 525 two simulations. In the lower thermosphere, at southern latitudes, GITM w/ WACCM-
 526 X has larger $n_s(z_o)$ and larger temperature ratio term because of the lower temperature,
 527 which results in increased O. However, in the upper thermosphere, as the scale height
 528 term becomes important, a lower temperature and thus a lower scale height has the op-
 529 posite effect on O as it acts to decrease the O number densities faster (also observed for
 530 N_2 above). Similarly, GITM w/ MSIS has higher temperature in this hemisphere result-
 531 ing in larger scale height and a slower decrease. Therefore, the difference between the
 532 simulations reduces in magnitude with altitude in Figure 9. For the northern hemisphere,
 533 the difference between $n_s(z_o) \times \frac{T_s(z_o)}{T_s(z)}$ at lower altitudes is small as also shown in Fig-
 534 ure 1. In the lower thermosphere, this term dominates. However, with increasing alti-
 535 tude, the effect of scale height causes the O number densities for the two simulations to
 536 become very close in magnitude and eventually at higher altitudes causes the difference
 537 to reverse. It should also be noted that the lower thermosphere is dominated by dynam-
 538 ics and the diffusive equilibrium reasoning here is used as a rough guide to understand
 539 the vertical profiles of different species.

540 Figure 8d shows the height profiles for O/N_2 . O/N_2 increases with altitude due to
 541 larger rate of decrease of N_2 as compared to O (N_2 has smaller scale height because of
 542 its larger mass). In the southern hemisphere, GITM w/ WACCM-X has larger O and
 543 smaller N_2 resulting in larger O/N_2 which affects the electron density. In the northern
 544 hemisphere, the situation is reversed where GITM w/ MSIS has larger O/N_2 and elec-
 545 tron density. Figure 9 also shows the percentage difference in height profile of electron
 546 density between the two simulations. The difference ranges between 10 - 40% at F-region
 547 altitudes and follows the O/N_2 difference in both the hemispheres.

548 Contour plots for O/N_2 are shown in Figure 10. Above ~ 120 km, both simulations
 549 show similar patterns in O/N_2 with larger values in the winter hemisphere. This is in-
 550 dicative of the summer to winter circulation shown in Figure 3. Figure 10c shows the
 551 percent difference between the two simulations. The difference is as large as 60% between
 552 the two simulations in the lower thermosphere in the southern hemisphere. The effect
 553 of lower thermospheric O distribution superimposes on the overall O/N_2 distribution in
 554 the upper thermosphere, leading to increases in O/N_2 in the hemisphere with larger lower
 555 thermospheric O. The effect of using O number densities from WACCM-X is to decrease
 556 the overall O/N_2 gradient between the two hemispheres. This result is similar to that
 557 observed by Qian and Yue (2017). When comparing the global averages, GITM w/ WACCM-
 558 X has higher O/N_2 , resulting in larger electron density.

559 Above 125 km, as shown in Figure 3, the winds are dominated by northward in-
 560 terhemispheric winds. Figure 3c showed that the winds in the upper thermosphere are
 561 slower for GITM w/ WACCM-X in the southern hemisphere and faster in the northern
 562 hemisphere. From Figure 10c, GITM w/ WACCM-X has ~ 20 - 30% more O/N_2 than GITM
 563 w/ MSIS in the equatorial region. This mainly comes from $+\sim 20\%$ in O and $-\sim 10\%$ dif-
 564 ference in N_2 . It can be observed from Figure 4e that GITM w/ WACCM-X has smaller
 565 northward directed pressure gradient in most of the summer and winter hemisphere at
 566 mid-latitudes and larger at higher latitudes in the winter hemisphere. The latitudinal
 567 gradient of higher equatorial O in GITM w/ WACCM-X leads to slower northward winds
 568 in the summer hemisphere and faster northward winds in the winter hemisphere as com-

569 pared to GITM w/ MSIS which has higher winter O. This change in interhemispheric
 570 winds is in equilibrium with the reduced O/N₂ gradient for GITM w/ WACCM-X. Be-
 571 cause the thermosphere is a non-linear system, changes in densities, temperatures, and
 572 winds further affect the transport and density distribution. Only the first order impact
 573 of lower thermospheric O distribution on the upper thermosphere is considered here.

574 Figure 11 shows a comparison between integrated O/N₂ for the two simulations
 575 and GUVI observations. As mentioned previously, using GITM w/ WACCM-X decreases
 576 the gradient in O/N₂ between the two hemispheres. Figure 11 shows O/N₂ is higher for
 577 GITM w/ WACCM-X in the southern hemisphere and lower in the northern hemisphere
 578 as compared to GITM w/ MSIS. In both hemispheres, GITM w/ WACCM-X matches
 579 with GUVI observations (Figure 11c) better. We would expect the correction of N₂ and
 580 other parameters in the lower thermosphere to bring the model results even closer to the
 581 observations. It was shown by Perlongo et al. (2018) that GITM has lower summer elec-
 582 tron densities than the GPS TEC observations in both the northern and southern mid-
 583 latitudes. Using GITM w/ WACCM-X at the lower boundary, this will potentially be
 584 corrected as the electron density depends on the O/N₂.

585 When the opposite solstice (i.e., June) is considered, the opposite behavior is ob-
 586 served. Figure 12 shows atomic oxygen distributions and O/N₂ for the month of June.
 587 GITM w/ WACCM-X and SABER number densities are similar in O distribution, al-
 588 though they are off in magnitude, while the MSIS driven simulation has the opposite gra-
 589 dient in O. Figure 12d shows the height profile of difference in O/N₂ between the two
 590 simulations. This is opposite of Figure 10c. Thus, the opposite O distribution in the lower
 591 thermosphere affects both solstices in a similar, but opposite, way.

592 As mentioned above, the decrease in O/N₂ gradient in GITM w/ WACCM-X is
 593 consistent with the results obtained by Qian and Yue (2017). They explained the mech-
 594 anism via vertical mixing due to lower thermospheric winter to summer circulation but
 595 did not show the species distribution in the lower thermosphere as a result of this cir-
 596 culation. Whereas this work starts with the species distribution in the lower thermosphere
 597 to observe the impact on the upper thermosphere. It is found that the O distribution
 598 at the mesopause affects the upper thermosphere in a more direct way than just through
 599 molecular diffusion : it impacts the wind and temperature distributions which subsequently
 600 changes the scale heights of molecular species. It is also found that using this distribu-
 601 tion increases the global O/N₂ which is opposite to the result obtained by Qian and Yue
 602 (2017). However, this difference depends on the lower thermospheric species distribu-
 603 tion from WACCM-X in our study and thus will change depending on the variability of
 604 the phenomena leading to this distribution.

605 4 Conclusions

606 Variations in O in the mesosphere and the lower thermosphere affect the compo-
 607 sition and dynamics of the upper thermosphere as it becomes a major species above 200
 608 km. Previous studies (Russell et al., 2004; Smith et al., 2010; Rezac et al., 2015) have
 609 shown that the summer hemisphere has higher atomic oxygen concentration in the lower
 610 thermosphere (90-100 km). Qian et al. (2017) suggested that the lower thermosphere win-
 611 ter to summer circulation is responsible for the high summer concentration of CO₂ in
 612 this region. In this study, we investigate the effect of the MLT O distribution on the com-
 613 position and dynamics of the middle-upper thermosphere using an ionosphere-thermosphere
 614 model, GITM. Conventionally, GITM uses O distribution that is higher in winter from
 615 MSIS at its lower boundary. We change the lower boundary O distribution to be higher
 616 in summer, as specified by WACCM-X, which also matches better with the observations
 617 from SABER. We find that the reversal of O hemispheric concentration changes the mag-
 618 nitudes of the winds between 100-120 km due to the differences in pressure gradients.
 619 The hemisphere with larger O number densities has larger equatorward winds resulting

in adiabatic cooling in that hemisphere. Larger radiative cooling in that hemisphere also leads to the cooling of that hemisphere. Other terms of the temperature equation such as advective, chemical, auroral, Joule and molecular conduction heating also change and affect the temperature distribution. Overall, the lower temperature decreases the scale height of N_2 and other molecular species in the hemisphere with more lower thermospheric O, resulting in a reduction of their number densities at higher altitudes. We also find that the averaged O densities at 100 km in both MSIS and WACCM-X are much lower than SABER. If these O densities would have been much closer to SABER, we would expect higher O in the thermosphere in both the simulations. We would also expect a net lower temperature in the thermosphere due to larger radiative cooling, which would then also change the wind magnitudes.

In January, the southern hemisphere has larger atomic oxygen in GITM w/ WACCM-X (and SABER data) as compared to GITM w/ MSIS, larger equatorward winds, more adiabatic and radiative cooling, lower temperature and lower N_2 . This results in an increased O/N_2 and electron densities in the southern (summer) hemisphere in the GITM w/ WACCM-X simulation. The opposite behaviour is observed in the northern (winter) hemisphere. The change in O/N_2 is as large as 63% in the summer hemisphere in the lower thermosphere. This also slows down the northward interhemispheric winds in the summer hemisphere and speeds them up in the winter hemisphere. It is found that the vertical column integrated O/N_2 in GITM w/ WACCM-X matches the TIMED GUVI O/N_2 measurements better in both the hemispheres, as GITM w/ MSIS tends to underestimate O/N_2 in the summer and overestimate it in the winter hemisphere. We would expect the correction of other mesopause boundary drivers within GITM such as N_2 and temperature to further improve the agreement between model results and the observations.

Acknowledgments

This work was supported by DoD grant #FA9550-16-1-0071. High computing resources were provided through Pleiades supercomputer by NASA Advanced Supercomputing (NAS) housed at NASA Ames Research Center and through Cheyenne supercomputer (doi:10.5065/D6RX99HX) by NCAR's Computational and Information Systems Laboratory sponsored by the National Science Foundation and other agencies. The atomic oxygen used in this study is from SABER data Version 2.0 and was downloaded from <http://saber.gats-inc.com/data.php>. The level 3 O/N_2 GUVI data was downloaded from <http://guvitimed.jhuapl.edu/>. The GITM runs that were used in this study can be accessed at <https://doi.org/10.7302/yagm-xv95>

References

- Akmaev, R. A. (2011). Whole atmosphere modeling: Connecting terrestrial and space weather. *Reviews of Geophysics*, 49(4). Retrieved from <https://agupubs.onlinelibrary.wiley.com/doi/abs/10.1029/2011RG000364> doi: 10.1029/2011RG000364
- Akmaev, R. A., Rowell, T. J. F., Wu, F., Forbes, J. M., Zhang, X., Anghel, A. F., ... Juang, H. (2008). Tidal variability in the lower thermosphere: Comparison of Whole Atmosphere Model (WAM) simulations with observations from TIMED. *Geophysical Research Letters*, 35(3). Retrieved from <https://agupubs.onlinelibrary.wiley.com/doi/abs/10.1029/2007GL032584> doi: 10.1029/2007GL032584
- Beagley, S., de Grandpr, J., Koshyk, J., McFarlane, N., & Shepherd, T. (1997). Radiative dynamical climatology of the first generation Canadian middle atmosphere model. *Atmosphere-Ocean*, 35(3), 293-331. Retrieved from <https://doi.org/10.1080/07055900.1997.9649595> doi: 10.1080/07055900.1997.9649595

- 671 Brasseur, G., & Solomon, S. (1984). *Aeronomy of the middle atmosphere*. D.Reidel,
672 Dordrecht.
- 673 Burns, A. G., Killeen, T. L., & Roble, R. G. (1989). Processes responsible for
674 the compositional structure of the thermosphere. *Journal of Geophysical*
675 *Research: Space Physics*, 94(A4), 3670-3686. Retrieved from [https://](https://agupubs.onlinelibrary.wiley.com/doi/abs/10.1029/JA094iA04p03670)
676 agupubs.onlinelibrary.wiley.com/doi/abs/10.1029/JA094iA04p03670
677 doi: 10.1029/JA094iA04p03670
- 678 Cageao, R., & Kerr, R. (1984). Global distribution of helium in the upper atmo-
679 sphere during solar minimum. *Planetary and Space Science*, 32(12), 1523 -
680 1529. Retrieved from [http://www.sciencedirect.com/science/article/](http://www.sciencedirect.com/science/article/pii/0032063384900199)
681 [pii/0032063384900199](http://www.sciencedirect.com/science/article/pii/0032063384900199) doi: [https://doi.org/10.1016/0032-0633\(84\)90019-9](https://doi.org/10.1016/0032-0633(84)90019-9)
- 682 Chamberlin, P. C., Woods, T. N., & Eparvier, F. G. (2008). Flare irradiance spec-
683 tral model (FISM): Flare component algorithms and results. *Space Weather*,
684 6(5). Retrieved from [https://agupubs.onlinelibrary.wiley.com/doi/abs/](https://agupubs.onlinelibrary.wiley.com/doi/abs/10.1029/2007SW000372)
685 [10.1029/2007SW000372](https://agupubs.onlinelibrary.wiley.com/doi/abs/10.1029/2007SW000372) doi: 10.1029/2007SW000372
- 686 Christensen, A. B., Paxton, L. J., Avery, S., Craven, J., Crowley, G., Humm,
687 D. C., ... Zhang, Y. (2003). Initial observations with the Global Ultra-
688 violet Imager (GUVI) in the NASA TIMED satellite mission. *Journal of*
689 *Geophysical Research: Space Physics*, 108(A12). Retrieved from [https://](https://agupubs.onlinelibrary.wiley.com/doi/abs/10.1029/2003JA009918)
690 agupubs.onlinelibrary.wiley.com/doi/abs/10.1029/2003JA009918 doi:
691 10.1029/2003JA009918
- 692 Christensen, A. B., Walterscheid, R. L., Ross, M. N., Meng, C.-I., Paxton, L. J.,
693 Jr., D. E. A., ... Strickland, D. J. (1994). Global Ultraviolet Imager (GUVI)
694 for the NASA Thermosphere-Ionsphere-Mesosphere Energetics and Dynamics
695 (TIMED) mission. In J. Wang & P. B. Hays (Eds.), *Optical spectroscopic tech-*
696 *niques and instrumentation for atmospheric and space research* (Vol. 2266, pp.
697 451 – 466). SPIE. Retrieved from <https://doi.org/10.1117/12.187583> doi:
698 10.1117/12.187583
- 699 Colegrove, F. D., Johnson, F. S., & Hanson, W. B. (1966). Atmospheric composi-
700 tion in the lower thermosphere. *Journal of Geophysical Research (1896-1977)*,
701 71(9), 2227-2236. Retrieved from [https://agupubs.onlinelibrary.wiley](https://agupubs.onlinelibrary.wiley.com/doi/abs/10.1029/JZ071i009p02227)
702 [.com/doi/abs/10.1029/JZ071i009p02227](https://agupubs.onlinelibrary.wiley.com/doi/abs/10.1029/JZ071i009p02227) doi: 10.1029/JZ071i009p02227
- 703 Deng, Y., Richmond, A. D., Ridley, A. J., & Liu, H.-L. (2008). Assessment of the
704 non-hydrostatic effect on the upper atmosphere using a general circulation
705 model (GCM). *Geophysical Research Letters*, 35(1). Retrieved from [https://](https://agupubs.onlinelibrary.wiley.com/doi/abs/10.1029/2007GL032182)
706 agupubs.onlinelibrary.wiley.com/doi/abs/10.1029/2007GL032182 doi:
707 10.1029/2007GL032182
- 708 Fukao, S., Yamanaka, M. D., Ao, N., Hocking, W. K., Sato, T., Yamamoto, M., ...
709 Kato, S. (1994). Seasonal variability of vertical eddy diffusivity in the middle
710 atmosphere: 1. three year observations by the middle and upper atmosphere
711 radar. *Journal of Geophysical Research: Atmospheres*, 99(D9), 18973-18987.
712 Retrieved from [https://agupubs.onlinelibrary.wiley.com/doi/abs/](https://agupubs.onlinelibrary.wiley.com/doi/abs/10.1029/94JD00911)
713 [10.1029/94JD00911](https://agupubs.onlinelibrary.wiley.com/doi/abs/10.1029/94JD00911) doi: 10.1029/94JD00911
- 714 Fuller-Rowell, T. J. (1998). The thermospheric spoon: A mechanism for the semi-
715 annual density variation. *Journal of Geophysical Research: Space Physics*,
716 103(A3), 3951-3956. Retrieved from [https://agupubs.onlinelibrary.wiley](https://agupubs.onlinelibrary.wiley.com/doi/abs/10.1029/97JA03335)
717 [.com/doi/abs/10.1029/97JA03335](https://agupubs.onlinelibrary.wiley.com/doi/abs/10.1029/97JA03335) doi: 10.1029/97JA03335
- 718 Fuller-Rowell, T. J., Akmaev, R. A., Wu, F., Anghel, A., Maruyama, N., Anderson,
719 D. N., ... Millward, G. (2008). Impact of terrestrial weather on the upper
720 atmosphere. *Geophysical Research Letters*, 35(9). Retrieved from [https://](https://agupubs.onlinelibrary.wiley.com/doi/abs/10.1029/2007GL032911)
721 agupubs.onlinelibrary.wiley.com/doi/abs/10.1029/2007GL032911 doi:
722 10.1029/2007GL032911
- 723 Fuller-Rowell, T. J., & Evans, D. S. (1987). Height-integrated Pedersen and Hall
724 conductivity patterns inferred from the TIROS-NOAA satellite data. *Jour-*
725 *nal of Geophysical Research: Space Physics*, 92(A7), 7606-7618. Retrieved

- 726 from [https://agupubs.onlinelibrary.wiley.com/doi/abs/10.1029/](https://agupubs.onlinelibrary.wiley.com/doi/abs/10.1029/JA092iA07p07606)
727 [JA092iA07p07606](https://agupubs.onlinelibrary.wiley.com/doi/abs/10.1029/JA092iA07p07606) doi: 10.1029/JA092iA07p07606
- 728 Garcia, R. R., Marsh, D. R., Kinnison, D. E., Boville, B. A., & Sassi, F. (2007).
729 Simulation of secular trends in the middle atmosphere, 1950 - 2003. *Journal*
730 *of Geophysical Research: Atmospheres*, 112(D9). Retrieved from [https://](https://agupubs.onlinelibrary.wiley.com/doi/abs/10.1029/2006JD007485)
731 agupubs.onlinelibrary.wiley.com/doi/abs/10.1029/2006JD007485 doi:
732 10.1029/2006JD007485
- 733 Grossmann, K., & Offermann, D. (1978). Atomic oxygen emission at 63 μm as a
734 cooling mechanism in the thermosphere and ionosphere. *Nature*, 276, 594-595.
735 doi: 10.1038/276594a0
- 736 Grossmann, K. U., Kaufmann, M., & Gerstner, E. (2000). A global measurement
737 of lower thermosphere atomic oxygen densities. *Geophysical Research Letters*,
738 27(9), 1387-1390. Retrieved from [https://agupubs.onlinelibrary.wiley](https://agupubs.onlinelibrary.wiley.com/doi/abs/10.1029/2000GL003761)
739 [.com/doi/abs/10.1029/2000GL003761](https://agupubs.onlinelibrary.wiley.com/doi/abs/10.1029/2000GL003761) doi: 10.1029/2000GL003761
- 740 Gumbel, J. (1997). *Rocket-borne optical measurements of minor constituents in the*
741 *middle atmosphere* (Unpublished doctoral dissertation). Stockholm University,
742 Department of Meteorology. (S. 1-44: sammanfattning, s. 45-271: 6 uppsatser)
- 743 Hagan, M. E., & Forbes, J. M. (2002). Migrating and nonmigrating diurnal tides in
744 the middle and upper atmosphere excited by tropospheric latent heat release.
745 *Journal of Geophysical Research: Atmospheres*, 107(D24), ACL 6-1-ACL 6-
746 15. Retrieved from [https://agupubs.onlinelibrary.wiley.com/doi/abs/](https://agupubs.onlinelibrary.wiley.com/doi/abs/10.1029/2001JD001236)
747 [10.1029/2001JD001236](https://agupubs.onlinelibrary.wiley.com/doi/abs/10.1029/2001JD001236) doi: 10.1029/2001JD001236
- 748 Hagan, M. E., Maute, A., & Roble, R. G. (2009). Tropospheric tidal effects on
749 the middle and upper atmosphere. *Journal of Geophysical Research: Space*
750 *Physics*, 114(A1). Retrieved from [https://agupubs.onlinelibrary.wiley](https://agupubs.onlinelibrary.wiley.com/doi/abs/10.1029/2008JA013637)
751 [.com/doi/abs/10.1029/2008JA013637](https://agupubs.onlinelibrary.wiley.com/doi/abs/10.1029/2008JA013637) doi: 10.1029/2008JA013637
- 752 Hays, P., Jones, R., & Rees, M. (1973). Auroral heating and the composition
753 of the neutral atmosphere. *Planetary and Space Science*, 21(4), 559 - 573.
754 Retrieved from [http://www.sciencedirect.com/science/article/pii/](http://www.sciencedirect.com/science/article/pii/0032063373900706)
755 [0032063373900706](http://www.sciencedirect.com/science/article/pii/0032063373900706) doi: [https://doi.org/10.1016/0032-0633\(73\)90070-6](https://doi.org/10.1016/0032-0633(73)90070-6)
- 756 Hedin, A. E. (1983). A revised thermospheric model based on mass spectrom-
757 eter and incoherent scatter data: Msis83. *Journal of Geophysical Re-*
758 *search: Space Physics*, 88(A12), 10170-10188. Retrieved from [https://](https://agupubs.onlinelibrary.wiley.com/doi/abs/10.1029/JA088iA12p10170)
759 agupubs.onlinelibrary.wiley.com/doi/abs/10.1029/JA088iA12p10170
760 doi: 10.1029/JA088iA12p10170
- 761 Hedin, A. E. (1987). Msis86 thermospheric model. *Journal of Geophysical*
762 *Research: Space Physics*, 92(A5), 4649-4662. Retrieved from [https://](https://agupubs.onlinelibrary.wiley.com/doi/abs/10.1029/JA092iA05p04649)
763 agupubs.onlinelibrary.wiley.com/doi/abs/10.1029/JA092iA05p04649
764 doi: 10.1029/JA092iA05p04649
- 765 Hedin, A. E. (1991). Extension of the msis thermosphere model into the middle and
766 lower atmosphere. *Journal of Geophysical Research: Space Physics*, 96(A2),
767 1159-1172. Retrieved from [https://agupubs.onlinelibrary.wiley.com/](https://agupubs.onlinelibrary.wiley.com/doi/abs/10.1029/90JA02125)
768 [doi/abs/10.1029/90JA02125](https://agupubs.onlinelibrary.wiley.com/doi/abs/10.1029/90JA02125) doi: 10.1029/90JA02125
- 769 Hodges, R. R. (1969). Eddy diffusion coefficients due to instabilities in internal grav-
770 ity waves. *Journal of Geophysical Research*, 74(16), 4087-4090. Retrieved
771 from [https://agupubs.onlinelibrary.wiley.com/doi/abs/10.1029/](https://agupubs.onlinelibrary.wiley.com/doi/abs/10.1029/JA074i016p04087)
772 [JA074i016p04087](https://agupubs.onlinelibrary.wiley.com/doi/abs/10.1029/JA074i016p04087) doi: 10.1029/JA074i016p04087
- 773 Humm, D. C., Ogorzalek, B. S., Elko, M. J., Morrison, D., & Paxton, L. J. (1999).
774 Optical calibration of the Global Ultraviolet Imager (GUVI). *Proc.SPIE*,
775 3818, 3818 - 3818 - 12. Retrieved from <https://doi.org/10.1117/12.364144>
776 doi: 10.1117/12.364144
- 777 Humm, D. C., Paxton, L. J., Christensen, A. B., Ogorzalek, B. S., Pardoe, C. T.,
778 Meng, C.-I., ... Ercol, C. J. (1998). Design and performance of the Global
779 Ultraviolet Imager (GUVI). *Proc.SPIE*, 3445, 3445 - 3445 - 11. Retrieved from
780 <https://doi.org/10.1117/12.330325> doi: 10.1117/12.330325

- 781 Hysell, D. L., Kelley, M. C., Swartz, W. E., & Woodman, R. F. (1990). Seeding
782 and layering of equatorial spread f by gravity waves. *Journal of Geophysical*
783 *Research: Space Physics*, 95(A10), 17253-17260. Retrieved from [https://](https://agupubs.onlinelibrary.wiley.com/doi/abs/10.1029/JA095iA10p17253)
784 agupubs.onlinelibrary.wiley.com/doi/abs/10.1029/JA095iA10p17253
785 doi: 10.1029/JA095iA10p17253
- 786 Immel, T. J., Sagawa, E., England, S. L., Henderson, S. B., Hagan, M. E., Mende,
787 S. B., ... Paxton, L. J. (2006). Control of equatorial ionospheric morphol-
788 ogy by atmospheric tides. *Geophysical Research Letters*, 33(15). Retrieved
789 from [https://agupubs.onlinelibrary.wiley.com/doi/abs/10.1029/](https://agupubs.onlinelibrary.wiley.com/doi/abs/10.1029/2006GL026161)
790 [2006GL026161](https://agupubs.onlinelibrary.wiley.com/doi/abs/10.1029/2006GL026161) doi: 10.1029/2006GL026161
- 791 Jin, H., Miyoshi, Y., Fujiwara, H., Shinagawa, H., Terada, K., Terada, N., ...
792 Saito, A. (2011). Vertical connection from the tropospheric activities to
793 the ionospheric longitudinal structure simulated by a new earth's whole at-
794 mosphere-ionosphere coupled model. *Journal of Geophysical Research: Space*
795 *Physics*, 116(A1). Retrieved from [https://agupubs.onlinelibrary.wiley](https://agupubs.onlinelibrary.wiley.com/doi/abs/10.1029/2010JA015925)
796 [.com/doi/abs/10.1029/2010JA015925](https://agupubs.onlinelibrary.wiley.com/doi/abs/10.1029/2010JA015925) doi: 10.1029/2010JA015925
- 797 Johnson, F. S. (1964). Composition changes in the upper atmosphere. *Electron Den-*
798 *sity Distribution in Ionosphere and Exosphere*. Thrane, 81, NorthHolland,
799 *Amsterdam*.
- 800 Johnson, F. S. (1973). Horizontal variations in thermospheric composi-
801 tion. *Reviews of Geophysics*, 11(3), 741-754. Retrieved from [https://](https://agupubs.onlinelibrary.wiley.com/doi/abs/10.1029/RG011i003p00741)
802 agupubs.onlinelibrary.wiley.com/doi/abs/10.1029/RG011i003p00741
803 doi: 10.1029/RG011i003p00741
- 804 Johnson, F. S., & Gottlieb, B. (1970). Eddy mixing and circulation at ionospheric
805 levels. *Planetary and Space Science*, 18(12), 1707 - 1718. Retrieved from
806 <http://www.sciencedirect.com/science/article/pii/0032063370900048>
807 doi: [https://doi.org/10.1016/0032-0633\(70\)90004-8](https://doi.org/10.1016/0032-0633(70)90004-8)
- 808 Johnson, F. S., & Gottlieb, B. (1973). Atomic oxygen transport in the thermo-
809 sphere. *Planetary and Space Science*, 21(6), 1001 - 1009. Retrieved from
810 <http://www.sciencedirect.com/science/article/pii/0032063373901463>
811 doi: [https://doi.org/10.1016/0032-0633\(73\)90146-3](https://doi.org/10.1016/0032-0633(73)90146-3)
- 812 Jones Jr., M., Emmert, J. T., Drob, D. P., Picone, J. M., & Meier, R. R. (2018).
813 Origins of the thermosphere-ionosphere semiannual oscillation: Refor-
814 mulating the thermospheric spoon mechanism. *Journal of Geophysi-*
815 *cal Research: Space Physics*, 123(1), 931-954. Retrieved from [https://](https://agupubs.onlinelibrary.wiley.com/doi/abs/10.1002/2017JA024861)
816 agupubs.onlinelibrary.wiley.com/doi/abs/10.1002/2017JA024861 doi:
817 10.1002/2017JA024861
- 818 Jones Jr., M., Emmert, J. T., Drob, D. P., & Siskind, D. E. (2017). Middle atmo-
819 sphere dynamical sources of the semiannual oscillation in the thermosphere
820 and ionosphere. *Geophysical Research Letters*, 44(1), 12-21. Retrieved
821 from [https://agupubs.onlinelibrary.wiley.com/doi/abs/10.1002/](https://agupubs.onlinelibrary.wiley.com/doi/abs/10.1002/2016GL071741)
822 [2016GL071741](https://agupubs.onlinelibrary.wiley.com/doi/abs/10.1002/2016GL071741) doi: 10.1002/2016GL071741
- 823 Keating, G. M., & Prior, E. J. (1968). The winter He bulge. *Space Res.*, 8, 982.
- 824 Kelly, M. A., Comberiate, J. M., Miller, E. S., & Paxton, L. J. (2014). Progress
825 toward forecasting of space weather effects on uhf satcom after operation
826 anaconda. *Space Weather*, 12(10), 601-611. Retrieved from [https://](https://agupubs.onlinelibrary.wiley.com/doi/abs/10.1002/2014SW001081)
827 agupubs.onlinelibrary.wiley.com/doi/abs/10.1002/2014SW001081 doi:
828 10.1002/2014SW001081
- 829 King, G. A. M. (1964). The dissociation of oxygen and high level circulation in the
830 atmosphere. *Journal of the Atmospheric Sciences*, 21(3), 231-237. doi: 10
831 .1175/1520-0469(1964)0210231:TDOOAH2.0.CO;2
- 832 Kirchhoff, V. W. J. H., & Clemesha, B. R. (1983). The atmospheric neutral sodium
833 layer: 2. diurnal variations. *Journal of Geophysical Research: Space Physics*,
834 88(A1), 442-450. Retrieved from [https://agupubs.onlinelibrary.wiley](https://agupubs.onlinelibrary.wiley.com/doi/abs/10.1029/JA088iA01p00442)
835 [.com/doi/abs/10.1029/JA088iA01p00442](https://agupubs.onlinelibrary.wiley.com/doi/abs/10.1029/JA088iA01p00442) doi: 10.1029/JA088iA01p00442

- 836 Lin, F. J., Chance, K. V., & Traub, W. A. (1987). Atomic oxygen in the lower
837 thermosphere. *Journal of Geophysical Research: Atmospheres*, *92*(D4), 4325-
838 4336. Retrieved from [https://agupubs.onlinelibrary.wiley.com/doi/abs/
839 10.1029/JD092iD04p04325](https://agupubs.onlinelibrary.wiley.com/doi/abs/10.1029/JD092iD04p04325) doi: 10.1029/JD092iD04p04325
- 840 Lin, S.-J. (2004). A vertically lagrangian finite-volume dynamical core for global
841 models. *Monthly Weather Review*, *132*(10), 2293-2307. Retrieved from
842 [https://doi.org/10.1175/1520-0493\(2004\)132<2293:AVLFDC>2.0.CO;2](https://doi.org/10.1175/1520-0493(2004)132<2293:AVLFDC>2.0.CO;2)
843 doi: 10.1175/1520-0493(2004)132<2293:AVLFDC>2.0.CO;2
- 844 Lindzen, R. S. (1981). Turbulence and stress owing to gravity wave and tidal
845 breakdown. *Journal of Geophysical Research: Oceans*, *86*(C10), 9707-9714.
846 Retrieved from [https://agupubs.onlinelibrary.wiley.com/doi/abs/
847 10.1029/JC086iC10p09707](https://agupubs.onlinelibrary.wiley.com/doi/abs/10.1029/JC086iC10p09707) doi: 10.1029/JC086iC10p09707
- 848 Liu, H., Foster, B. T., Hagan, M. E., McInerney, J. M., Maute, A., Qian, L., ...
849 Oberheide, J. (2010). Thermosphere extension of the Whole Atmosphere
850 Community Climate Model. *Journal of Geophysical Research: Space Physics*,
851 *115*(A12). Retrieved from [https://agupubs.onlinelibrary.wiley.com/
852 doi/abs/10.1029/2010JA015586](https://agupubs.onlinelibrary.wiley.com/doi/abs/10.1029/2010JA015586) doi: 10.1029/2010JA015586
- 853 Liu, H.-L. (2007). On the large wind shear and fast meridional transport above the
854 mesopause. *Geophysical Research Letters*, *34*(8). Retrieved from [https://
855 agupubs.onlinelibrary.wiley.com/doi/abs/10.1029/2006GL028789](https://agupubs.onlinelibrary.wiley.com/doi/abs/10.1029/2006GL028789) doi:
856 10.1029/2006GL028789
- 857 Liu, H.-L., Bardeen, C. G., Foster, B. T., Lauritzen, P., Liu, J., Lu, G., ... Wang,
858 W. (2018). Development and validation of the Whole Atmosphere Community
859 Climate Model With Thermosphere and Ionosphere Extension (WACCM-
860 X 2.0). *Journal of Advances in Modeling Earth Systems*, *10*(2), 381-402.
861 Retrieved from [https://agupubs.onlinelibrary.wiley.com/doi/abs/
862 10.1002/2017MS001232](https://agupubs.onlinelibrary.wiley.com/doi/abs/10.1002/2017MS001232) doi: 10.1002/2017MS001232
- 863 Liu, X., Wang, W., Thayer, J. P., Burns, A., Sutton, E., Solomon, S. C., ... Lucas,
864 G. (2014). The winter helium bulge revisited. *Geophysical Research Letters*,
865 *41*(19), 6603-6609. Retrieved from [https://agupubs.onlinelibrary.wiley
866 .com/doi/abs/10.1002/2014GL061471](https://agupubs.onlinelibrary.wiley.com/doi/abs/10.1002/2014GL061471) doi: 10.1002/2014GL061471
- 867 Malhotra, G., Ruohoniemi, J. M., Baker, J. B. H., Hibbins, R. E., & McWilliams,
868 K. A. (2016). Hf radar observations of a quasi-biennial oscillation in mid-
869 latitude mesospheric winds. *Journal of Geophysical Research: Atmospheres*,
870 *121*(21), 12,677-12,689. Retrieved from [https://agupubs.onlinelibrary
871 .wiley.com/doi/abs/10.1002/2016JD024935](https://agupubs.onlinelibrary.wiley.com/doi/abs/10.1002/2016JD024935) doi: 10.1002/2016JD024935
- 872 Marsh, D. R., Mills, M. J., Kinnison, D. E., Lamarque, J.-F., Calvo, N., & Polvani,
873 L. M. (2013). Climate change from 1850 to 2005 simulated in cesm1(waccm).
874 *Journal of Climate*, *26*(19), 7372-7391. Retrieved from [https://doi.org/
875 10.1175/JCLI-D-12-00558.1](https://doi.org/10.1175/JCLI-D-12-00558.1) doi: 10.1175/JCLI-D-12-00558.1
- 876 Mayr, H. G., Harris, I., & Spencer, N. W. (1978). Some properties of upper at-
877 mosphere dynamics. *Reviews of Geophysics*, *16*(4), 539-565. Retrieved
878 from [https://agupubs.onlinelibrary.wiley.com/doi/abs/10.1029/
879 RG016i004p00539](https://agupubs.onlinelibrary.wiley.com/doi/abs/10.1029/RG016i004p00539) doi: 10.1029/RG016i004p00539
- 880 Meier, R. R., Picone, J. M., Drob, D., Bishop, J., Emmert, J. T., Lean, J. L., ...
881 Gibson, S. T. (2014). Remote sensing of earth's limb by timed/guvi: Retrieval
882 of thermospheric composition and temperature. *Earth and Space Science*, *2*(1),
883 1-37. Retrieved from [https://agupubs.onlinelibrary.wiley.com/doi/abs/
884 10.1002/2014EA000035](https://agupubs.onlinelibrary.wiley.com/doi/abs/10.1002/2014EA000035) doi: 10.1002/2014EA000035
- 885 Mlynczak, M. G. (1996). Energetics of the middle atmosphere: Theory and ob-
886 servation requirements. *Advances in Space Research*, *17*(11), 117 - 126.
887 Retrieved from [http://www.sciencedirect.com/science/article/pii/
888 0273117795007392](http://www.sciencedirect.com/science/article/pii/S0273117795007392) doi: [https://doi.org/10.1016/0273-1177\(95\)00739-2](https://doi.org/10.1016/0273-1177(95)00739-2)
- 889 Mlynczak, M. G. (1997). Energetics of the mesosphere and lower thermosphere
890 and the SABER experiment. *Advances in Space Research*, *20*(6), 1177 -

1183. Retrieved from <http://www.sciencedirect.com/science/article/pii/S0273117797007692> (Coupling and Energetics in the Stratosphere-Mesosphere-Thermosphere-Ionosphere System) doi: [https://doi.org/10.1016/S0273-1177\(97\)00769-2](https://doi.org/10.1016/S0273-1177(97)00769-2)
- Mlynczak, M. G., Hunt, L. A., Mast, J. C., Thomas Marshall, B., Russell III, J. M., Smith, A. K., ... Gordley, L. L. (2013). Atomic oxygen in the mesosphere and lower thermosphere derived from SABER: Algorithm theoretical basis and measurement uncertainty. *Journal of Geophysical Research: Atmospheres*, 118(11), 5724-5735. Retrieved from <https://agupubs.onlinelibrary.wiley.com/doi/abs/10.1002/jgrd.50401> doi: 10.1002/jgrd.50401
- Mlynczak, M. G., Hunt, L. A., Russell III, J. M., & Marshall, B. T. (2018). Updated SABER Night Atomic Oxygen and implications for SABER Ozone and Atomic Hydrogen. *Geophysical Research Letters*, 45(11), 5735-5741. Retrieved from <https://agupubs.onlinelibrary.wiley.com/doi/abs/10.1029/2018GL077377> doi: 10.1029/2018GL077377
- Mlynczak, M. G., Martin-Torres, F. J., Johnson, D. G., Kratz, D. P., Traub, W. A., & Jucks, K. (2004). Observations of the O(3P) fine structure line at 63 μ m in the upper mesosphere and lower thermosphere. *Journal of Geophysical Research: Space Physics*, 109(A12). Retrieved from <https://agupubs.onlinelibrary.wiley.com/doi/abs/10.1029/2004JA010595> doi: 10.1029/2004JA010595
- Offermann, D. (1974). Composition variations in the lower thermosphere. *Journal of Geophysical Research (1896-1977)*, 79(28), 4281-4293. Retrieved from <https://agupubs.onlinelibrary.wiley.com/doi/abs/10.1029/JA079i028p04281> doi: 10.1029/JA079i028p04281
- Paxton, L. J., Christensen, A. B., Humm, D. C., Ogorzalek, B. S., Pardoe, C. T., Morrison, D., ... Meng, C.-I. (1999). Global Ultraviolet Imager (GUVI): measuring composition and energy inputs for the NASA Thermosphere Ionosphere Mesosphere Energetics and Dynamics (TIMED) mission. In A. M. Larar (Ed.), *Optical spectroscopic techniques and instrumentation for atmospheric and space research iii* (Vol. 3756, pp. 265 – 276). SPIE. Retrieved from <https://doi.org/10.1117/12.366380> doi: 10.1117/12.366380
- Paxton, L. J., Christensen, A. B., Morrison, D., Wolven, B., Kil, H., Zhang, Y., ... Meng, C.-I. (2004). GUVI: a hyperspectral imager for geospace. In C. A. Nardell, P. G. Lucey, J.-H. Yee, & J. B. Garvin (Eds.), *Instruments, science, and methods for geospace and planetary remote sensing* (Vol. 5660, pp. 228 – 240). SPIE. Retrieved from <https://doi.org/10.1117/12.579171> doi: 10.1117/12.579171
- Perlongo, N. J., Ridley, A. J., Cnossen, I., & Wu, C. (2018). A year-long comparison of gps tec and global ionosphere-thermosphere models. *Journal of Geophysical Research: Space Physics*, 123(2), 1410-1428. Retrieved from <https://agupubs.onlinelibrary.wiley.com/doi/abs/10.1002/2017JA024411> doi: 10.1002/2017JA024411
- Picone, J. M., Hedin, A. E., Drob, D. P., & Aikin, A. C. (2002). Nrlmsise-00 empirical model of the atmosphere: Statistical comparisons and scientific issues. *Journal of Geophysical Research: Space Physics*, 107(A12), SIA 15-1-SIA 15-16. Retrieved from <https://agupubs.onlinelibrary.wiley.com/doi/abs/10.1029/2002JA009430> doi: 10.1029/2002JA009430
- Pilinski, M. D., & Crowley, G. (2015). Seasonal variability in global eddy diffusion and the effect on neutral density. *Journal of Geophysical Research: Space Physics*, 120(4), 3097-3117. Retrieved from <https://agupubs.onlinelibrary.wiley.com/doi/abs/10.1002/2015JA021084> doi: 10.1002/2015JA021084
- Prakash, S. (1999). Production of electric field perturbations by gravity wave winds in the e region suitable for initiating equatorial spread f. *Journal of Geophysi-*

- 946 *cal Research: Space Physics*, 104(A5), 10051-10069. Retrieved from [https://](https://agupubs.onlinelibrary.wiley.com/doi/abs/10.1029/1999JA900028)
 947 agupubs.onlinelibrary.wiley.com/doi/abs/10.1029/1999JA900028 doi:
 948 10.1029/1999JA900028
- 949 Qian, L., Burns, A., & Yue, J. (2017). Evidence of the Lower Thermospheric
 950 Winter-to-Summer circulation from SABER CO₂ observations. *Geophys-*
 951 *ical Research Letters*, 44(20), 10,100-10,107. Retrieved from [https://](https://agupubs.onlinelibrary.wiley.com/doi/abs/10.1002/2017GL075643)
 952 agupubs.onlinelibrary.wiley.com/doi/abs/10.1002/2017GL075643 doi:
 953 10.1002/2017GL075643
- 954 Qian, L., Burns, A. G., Emery, B. A., Foster, B., Lu, G., Maute, A., ... Wang, W.
 955 (2014). The near tie-gcm. In *Modeling the ionospherethermosphere system*
 956 (p. 73-83). American Geophysical Union (AGU). Retrieved from [https://](https://agupubs.onlinelibrary.wiley.com/doi/abs/10.1002/9781118704417.ch7)
 957 agupubs.onlinelibrary.wiley.com/doi/abs/10.1002/9781118704417.ch7
 958 doi: 10.1002/9781118704417.ch7
- 959 Qian, L., Burns, A. G., Solomon, S. S., Smith, A. K., McInerney, J. M., Hunt,
 960 L. A., ... Vitt, F. M. (2018). Temporal Variability of Atomic Hydrogen
 961 From the Mesopause to the Upper Thermosphere. *Journal of Geophys-*
 962 *ical Research: Space Physics*, 123(1), 1006-1017. Retrieved from [https://](https://agupubs.onlinelibrary.wiley.com/doi/abs/10.1002/2017JA024998)
 963 agupubs.onlinelibrary.wiley.com/doi/abs/10.1002/2017JA024998 doi:
 964 10.1002/2017JA024998
- 965 Qian, L., Solomon, S. C., & Kane, T. J. (2009). Seasonal variation of thermospheric
 966 density and composition. *Journal of Geophysical Research: Space Physics*,
 967 114(A1). Retrieved from [https://agupubs.onlinelibrary.wiley.com/doi/](https://agupubs.onlinelibrary.wiley.com/doi/abs/10.1029/2008JA013643)
 968 [abs/10.1029/2008JA013643](https://agupubs.onlinelibrary.wiley.com/doi/abs/10.1029/2008JA013643) doi: 10.1029/2008JA013643
- 969 Qian, L., & Yue, J. (2017). Impact of the lower thermospheric winter-to-summer
 970 residual circulation on thermospheric composition. *Geophysical Research Let-*
 971 *ters*, 44(9), 3971-3979. Retrieved from [https://agupubs.onlinelibrary](https://agupubs.onlinelibrary.wiley.com/doi/abs/10.1002/2017GL073361)
 972 [.wiley.com/doi/abs/10.1002/2017GL073361](https://agupubs.onlinelibrary.wiley.com/doi/abs/10.1002/2017GL073361) doi: 10.1002/2017GL073361
- 973 Reber, C. A., Cooley, J. E., & Harpold, D. N. (1968). Upper atmosphere hydrogen
 974 and helium measurements from the explorer 32 satellite. *Space Res.*, 8, 993.
- 975 Reber, C. A., & Hays, P. B. (1973). Thermospheric wind effects on the distribution
 976 of helium and argon in the earth's upper atmosphere. *Journal of Geophys-*
 977 *ical Research (1896-1977)*, 78(16), 2977-2991. Retrieved from [https://](https://agupubs.onlinelibrary.wiley.com/doi/abs/10.1029/JA078i016p02977)
 978 agupubs.onlinelibrary.wiley.com/doi/abs/10.1029/JA078i016p02977
 979 doi: 10.1029/JA078i016p02977
- 980 Rezac, L., Jian, Y., Yue, J., Russell III, J. M., Kutepov, A., Garcia, R., ... Bernath,
 981 P. (2015). Validation of the global distribution of CO₂ volume mixing ratio in
 982 the mesosphere and lower thermosphere from SABER. *Journal of Geophysical*
 983 *Research: Atmospheres*, 120(23), 12,067-12,081. Retrieved from [https://](https://agupubs.onlinelibrary.wiley.com/doi/abs/10.1002/2015JD023955)
 984 agupubs.onlinelibrary.wiley.com/doi/abs/10.1002/2015JD023955 doi:
 985 10.1002/2015JD023955
- 986 Richmond, A. D., Ridley, E. C., & Roble, R. G. (1992). A thermosphere/ionosphere
 987 general circulation model with coupled electrodynamics. *Geophysical Research*
 988 *Letters*, 19(6), 601-604. Retrieved from [https://agupubs.onlinelibrary](https://agupubs.onlinelibrary.wiley.com/doi/abs/10.1029/92GL00401)
 989 [.wiley.com/doi/abs/10.1029/92GL00401](https://agupubs.onlinelibrary.wiley.com/doi/abs/10.1029/92GL00401) doi: 10.1029/92GL00401
- 990 Ridley, A., Deng, Y., & Tth, G. (2006). The global ionospherethermosphere
 991 model. *Journal of Atmospheric and Solar-Terrestrial Physics*, 68(8), 839 -
 992 864. Retrieved from [http://www.sciencedirect.com/science/article/pii/](http://www.sciencedirect.com/science/article/pii/S1364682606000071)
 993 [S1364682606000071](http://www.sciencedirect.com/science/article/pii/S1364682606000071) doi: <https://doi.org/10.1016/j.jastp.2006.01.008>
- 994 Rienecker, M. M., Suarez, M. J., Gelaro, R., Todling, R., Bacmeister, J., Liu, E.,
 995 ... Woollen, J. (2011). MERRA: NASA's modern-era retrospective anal-
 996 ysis for research and applications. *Journal of Climate*, 24(14), 3624-3648.
 997 Retrieved from <https://doi.org/10.1175/JCLI-D-11-00015.1> doi:
 998 10.1175/JCLI-D-11-00015.1
- 999 Rishbeth, H. (1998). How the thermospheric circulation affects the ionospheric
 1000 f₂-layer. *Journal of Atmospheric and Solar-Terrestrial Physics*, 60(14), 1385

- 1001 - 1402. Retrieved from <http://www.sciencedirect.com/science/article/pii/S1364682698000625> doi: [https://doi.org/10.1016/S1364-6826\(98\)00062-5](https://doi.org/10.1016/S1364-6826(98)00062-5)
- 1002
- 1003
- 1004 Roble, R. (2013). On the feasibility of developing a global atmospheric model extending from the ground to the exosphere. In *Atmospheric science across the stratopause* (p. 53-67). American Geophysical Union (AGU). Retrieved from
- 1005
- 1006 <https://agupubs.onlinelibrary.wiley.com/doi/abs/10.1029/GM123p0053>
- 1007 doi: 10.1029/GM123p0053
- 1008
- 1009 Rottger, J. (1973). Wave-like structures of large-scale equatorial spread-f irregularities. *Journal of Atmospheric and Terrestrial Physics*, 35(6), 1195 - 1206.
- 1010 Retrieved from <http://www.sciencedirect.com/science/article/pii/0021916973900160> doi: [https://doi.org/10.1016/0021-9169\(73\)90016-0](https://doi.org/10.1016/0021-9169(73)90016-0)
- 1011
- 1012
- 1013 Russell, J. P., Lowe, R., & Ward, W. (2004). Atomic oxygen annual and semi-annual variations in the mesopause region for mid and equatorial latitudes. *Journal of Atmospheric and Solar-Terrestrial Physics*, 66(6), 451 - 461. Retrieved from
- 1014
- 1015 <http://www.sciencedirect.com/science/article/pii/S1364682604000124>
- 1016 (Dynamics and Chemistry of the MLT Region - PSMOS 2002 International
- 1017 Symposium) doi: <https://doi.org/10.1016/j.jastp.2004.01.004>
- 1018
- 1019 Russell III, J., Mlynczak, M., Gordley, L., Tansock, J., & Esplin, R. (1999, 10). Overview of the SABER experiment and preliminary calibration results. *Proceedings of SPIE - The International Society for Optical Engineering*, 3756.
- 1020
- 1021
- 1022 Salinas, C. C. J. H., Chang, L. C., Liang, M. ., Yue, J., Russell, J., & Mlynczak, M. (2016). Impacts of SABER CO2 based eddy diffusion coefficients in the
- 1023
- 1024 lower thermosphere on the ionosphere/thermosphere. *Journal of Geophysical Research: Space Physics*, 121(12), 12,080-12,092. Retrieved from <https://agupubs.onlinelibrary.wiley.com/doi/abs/10.1002/2016JA023161> doi:
- 1025
- 1026 10.1002/2016JA023161
- 1027
- 1028 Sasi, M. N., & Vijayan, L. (2001). Turbulence characteristics in the tropical mesosphere as obtained by MST radar at Gadanki (13.5 n, 79.2 e). *Annales Geophysicae*, 19(8), 1019-1025. Retrieved from <https://www.ann-geophys.net/19/1019/2001/> doi: 10.5194/angeo-19-1019-2001
- 1029
- 1030
- 1031
- 1032 Schunk, R., & Nagy, A. (2009). *Ionospheres: Physics, plasma physics, and chemistry* (2nd ed.). Cambridge University Press. doi: 10.1017/CBO9780511635342
- 1033
- 1034 Sheese, P. E., McDade, I. C., Gattinger, R. L., & Llewellyn, E. J. (2011). Atomic oxygen densities retrieved from Optical Spectrograph and Infrared Imaging
- 1035
- 1036 System observations of O2 A-band airglow emission in the mesosphere and lower thermosphere. *Journal of Geophysical Research: Atmospheres*, 116(D1). Retrieved from <https://agupubs.onlinelibrary.wiley.com/doi/abs/10.1029/2010JD014640> doi: 10.1029/2010JD014640
- 1037
- 1038
- 1039
- 1040 Shimazaki, T. (1965). On the continuity equation for electron density in the ionosphere. *Journal of Atmospheric and Terrestrial Physics*, 27(5), 593 - 604. Retrieved from <http://www.sciencedirect.com/science/article/pii/0021916965901273> doi: [https://doi.org/10.1016/0021-9169\(65\)90127-3](https://doi.org/10.1016/0021-9169(65)90127-3)
- 1041
- 1042
- 1043
- 1044 Shimazaki, T. (1966). Nighttime variations of fregion electron density profiles at puerto rico: 2. an attempt to separate the effects of temperature variation and drift velocity. *Journal of Geophysical Research*, 71(13), 3177-3190. Retrieved from <https://agupubs.onlinelibrary.wiley.com/doi/abs/10.1029/JZ071i013p03177> doi: 10.1029/JZ071i013p03177
- 1045
- 1046
- 1047
- 1048
- 1049 Shimazaki, T. (1967). Dynamic effects on atomic and molecular oxygen density distributions in the upper atmosphere: a numerical solution to equations of motion and continuity. *Journal of Atmospheric and Terrestrial Physics*, 29(6), 723 - 747. Retrieved from <http://www.sciencedirect.com/science/article/pii/0021916967902164> doi: [https://doi.org/10.1016/0021-9169\(67\)90216-4](https://doi.org/10.1016/0021-9169(67)90216-4)
- 1050
- 1051
- 1052
- 1053
- 1054
- 1055 Shimazaki, T. (1968). Dynamic effects on height distributions of neutral con-

- stituents in the Earth's upper atmosphere: a calculation of atmospheric model between 70 km and 500 km. *Journal of Atmospheric and Terrestrial Physics*, 30(7), 1279 - 1292. Retrieved from <http://www.sciencedirect.com/science/article/pii/S0021916968911070> doi: [https://doi.org/10.1016/S0021-9169\(68\)91107-0](https://doi.org/10.1016/S0021-9169(68)91107-0)
- Siskind, D. E., Drob, D. P., Dymond, K. F., & McCormack, J. P. (2014). Simulations of the effects of vertical transport on the thermosphere and ionosphere using two coupled models. *Journal of Geophysical Research: Space Physics*, 119(2), 1172-1185. Retrieved from <https://agupubs.onlinelibrary.wiley.com/doi/abs/10.1002/2013JA019116> doi: 10.1002/2013JA019116
- Smith, A. K., Garcia, R. R., Marsh, D. R., & Richter, J. H. (2011). WACCM simulations of the mean circulation and trace species transport in the winter mesosphere. *Journal of Geophysical Research: Atmospheres*, 116(D20). Retrieved from <https://agupubs.onlinelibrary.wiley.com/doi/abs/10.1029/2011JD016083> doi: 10.1029/2011JD016083
- Smith, A. K., Harvey, V. L., Mlynczak, M. G., Funke, B., Garca-Comas, M., Hervig, M., ... Walker, K. A. (2013). Satellite observations of ozone in the upper mesosphere. *Journal of Geophysical Research: Atmospheres*, 118(11), 5803-5821. Retrieved from <https://agupubs.onlinelibrary.wiley.com/doi/abs/10.1002/jgrd.50445> doi: 10.1002/jgrd.50445
- Smith, A. K., Marsh, D. R., Mlynczak, M. G., & Mast, J. C. (2010). Temporal variations of atomic oxygen in the upper mesosphere from SABER. *Journal of Geophysical Research: Atmospheres*, 115(D18). Retrieved from <https://agupubs.onlinelibrary.wiley.com/doi/abs/10.1029/2009JD013434> doi: 10.1029/2009JD013434
- Sutton, E. K. (2016). Interhemispheric transport of light neutral species in the thermosphere. *Geophysical Research Letters*, 43(24), 12,325-12,332. Retrieved from <https://agupubs.onlinelibrary.wiley.com/doi/abs/10.1002/2016GL071679> doi: 10.1002/2016GL071679
- von Zahn, U. (1967). Mass spectrometric measurements of atomic oxygen in the upper atmosphere: A critical review. *Journal of Geophysical Research (1896-1977)*, 72(23), 5933-5937. Retrieved from <https://agupubs.onlinelibrary.wiley.com/doi/abs/10.1029/JZ072i023p05933> doi: 10.1029/JZ072i023p05933
- Walker, J. C. G. (1965). Analytic representation of upper atmosphere densities based on Jacchia's Static Diffusion Models. *Journal of the Atmospheric Sciences*, 22(4), 462-463. Retrieved from [https://doi.org/10.1175/1520-0469\(1965\)022<0462:AROUAD>2.0.CO;2](https://doi.org/10.1175/1520-0469(1965)022<0462:AROUAD>2.0.CO;2) doi: 10.1175/1520-0469(1965)022(0462:AROUAD)2.0.CO;2
- Weimer, D. R. (2005). Improved ionospheric electrodynamic models and application to calculating joule heating rates. *Journal of Geophysical Research: Space Physics*, 110(A5). Retrieved from <https://agupubs.onlinelibrary.wiley.com/doi/abs/10.1029/2004JA010884> doi: 10.1029/2004JA010884
- Weimer, D. R., Mlynczak, M. G., Emmert, J. T., Doornbos, E., Sutton, E. K., & Hunt, L. A. (2018). Correlations between the Thermosphere's Semiannual Density Variations and Infrared Emissions Measured With the SABER Instrument. *Journal of Geophysical Research: Space Physics*, 123(10), 8850-8864. Retrieved from <https://agupubs.onlinelibrary.wiley.com/doi/abs/10.1029/2018JA025668> doi: 10.1029/2018JA025668
- Wu, D. L., Yee, J.-H., Schlecht, E., Mehdi, I., Siles, J., & Drouin, B. J. (2016). The limb sounder (tls) for lower thermospheric wind, oxygen density, and temperature. *Journal of Geophysical Research: Space Physics*, 121(7), 7301-7315. Retrieved from <https://agupubs.onlinelibrary.wiley.com/doi/abs/10.1002/2015JA022314> doi: 10.1002/2015JA022314
- Wu, Q., Ortland, D., Foster, B., & Roble, R. (2012). Simulation of nonmigrat-

- 1111 ing tide influences on the thermosphere and ionosphere with a timed data
 1112 driven TIEGCM. *Journal of Atmospheric and Solar-Terrestrial Physics*,
 1113 *90-91*, 61 - 67. Retrieved from [http://www.sciencedirect.com/science/](http://www.sciencedirect.com/science/article/pii/S1364682612000429)
 1114 [article/pii/S1364682612000429](http://www.sciencedirect.com/science/article/pii/S1364682612000429) (Recent Progress in the Vertical Cou-
 1115 pling in the Atmosphere-Ionosphere System) doi: [https://doi.org/10.1016/](https://doi.org/10.1016/j.jastp.2012.02.009)
 1116 [j.jastp.2012.02.009](https://doi.org/10.1016/j.jastp.2012.02.009)
- 1117 Yamazaki, Y., & Richmond, A. D. (2013). A theory of ionospheric response to
 1118 upward-propagating tides: Electrodynamical effects and tidal mixing effects.
 1119 *Journal of Geophysical Research: Space Physics*, *118*(9), 5891-5905. Retrieved
 1120 from [https://agupubs.onlinelibrary.wiley.com/doi/abs/10.1002/](https://agupubs.onlinelibrary.wiley.com/doi/abs/10.1002/jgra.50487)
 1121 [jgra.50487](https://agupubs.onlinelibrary.wiley.com/doi/abs/10.1002/jgra.50487) doi: 10.1002/jgra.50487
- 1122 Yee, J. H. (2003). TIMED mission science overview. *John Hopkins APL Technical*
 1123 *Digest*, *24*(2), 136-141 Apr-Jun.
- 1124 Yue, J., Jian, Y., Wang, W., Meier, R., Burns, A., Qian, L., ... Mlynckzak, M.
 1125 (2019). Annual and Semiannual Oscillations of Thermospheric Compo-
 1126 sition in TIMED/GUVI Limb measurements. *Journal of Geophysical*
 1127 *Research: Space Physics*, *124*(4), 3067-3082. Retrieved from [https://](https://agupubs.onlinelibrary.wiley.com/doi/abs/10.1029/2019JA026544)
 1128 agupubs.onlinelibrary.wiley.com/doi/abs/10.1029/2019JA026544 doi:
 1129 [10.1029/2019JA026544](https://doi.org/10.1029/2019JA026544)
- 1130 Zhang, X., Forbes, J. M., & Hagan, M. E. (2010a). Longitudinal variation of tides in
 1131 the mlt region: 1. tides driven by tropospheric net radiative heating. *Journal*
 1132 *of Geophysical Research: Space Physics*, *115*(A6). Retrieved from [https://](https://agupubs.onlinelibrary.wiley.com/doi/abs/10.1029/2009JA014897)
 1133 agupubs.onlinelibrary.wiley.com/doi/abs/10.1029/2009JA014897 doi:
 1134 [10.1029/2009JA014897](https://doi.org/10.1029/2009JA014897)
- 1135 Zhang, X., Forbes, J. M., & Hagan, M. E. (2010b). Longitudinal variation of
 1136 tides in the MLT region: 2. relative effects of solar radiative and latent heat-
 1137 ing. *Journal of Geophysical Research: Space Physics*, *115*(A6). Retrieved
 1138 from [https://agupubs.onlinelibrary.wiley.com/doi/abs/10.1029/](https://agupubs.onlinelibrary.wiley.com/doi/abs/10.1029/2009JA014898)
 1139 [2009JA014898](https://agupubs.onlinelibrary.wiley.com/doi/abs/10.1029/2009JA014898) doi: 10.1029/2009JA014898
- 1140 Zhang, Y., Paxton, L., Morrison, D., Marsh, D., & Kil, H. (2014). Storm-
 1141 time behaviors of O/N₂ and NO variations. *Journal of Atmospheric*
 1142 *and Solar-Terrestrial Physics*, *114*, 42 - 49. Retrieved from [http://](http://www.sciencedirect.com/science/article/pii/S136468261400087X)
 1143 www.sciencedirect.com/science/article/pii/S136468261400087X doi:
 1144 <https://doi.org/10.1016/j.jastp.2014.04.003>
- 1145 Zhang, Y., Paxton, L. J., Morrison, D., Wolven, B., Kil, H., Meng, C., ... Immel,
 1146 T. J. (2004). O/N₂ changes during 14 october 2002 storms: IMAGE SI-13 and
 1147 TIMED/GUVI observations. *Journal of Geophysical Research: Space Physics*,
 1148 *109*(A10). Retrieved from [https://agupubs.onlinelibrary.wiley.com/](https://agupubs.onlinelibrary.wiley.com/doi/abs/10.1029/2004JA010441)
 1149 [doi/abs/10.1029/2004JA010441](https://agupubs.onlinelibrary.wiley.com/doi/abs/10.1029/2004JA010441) doi: 10.1029/2004JA010441

Table 1. Parameter values at the lower boundary - GITM w/ MSIS and GITM w/ WACCM-X

Parameter	Value
Temperature, T	150 K
Zonal Winds, U	0 m/s
Meridional Winds, V	0 m/s
Molecular Oxygen, O ₂	$1 \times 10^{18} \text{ m}^{-3}$
Molecular Nitrogen, N ₂	$1 \times 10^{19} \text{ m}^{-3}$
Nitric Oxide, NO	$1 \times 10^{14} \text{ m}^{-3}$

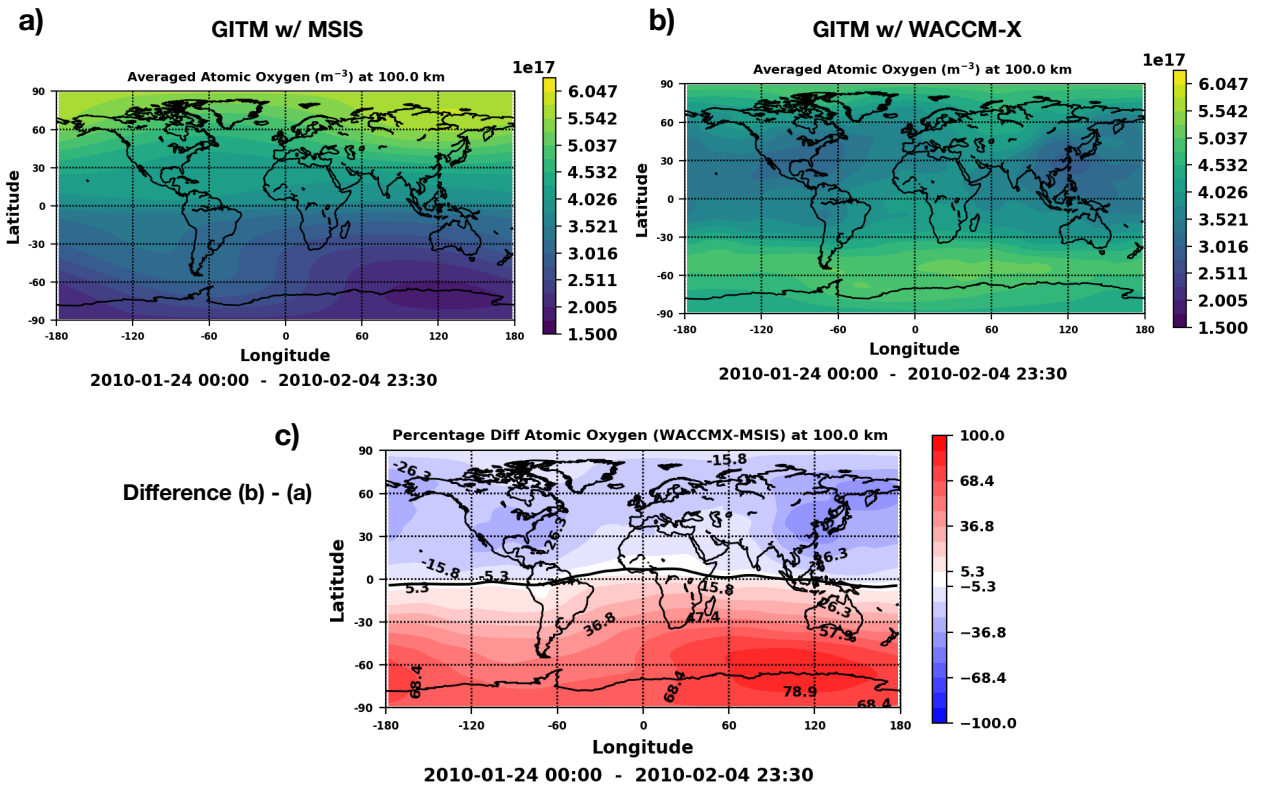


Figure 1. a) Atomic Oxygen for GITM w/ MSIS at 100 km averaged for time periods 01/24/2010 - 02/04/2010. b) Similar to a) but for GITM w/ WACCM-X. c) Averaged Difference in Atomic Oxygen at 100 km : GITM w/ WACCM-X (b) - GITM w/ MSIS (a). Note the thicker black line roughly parallel to the equator. This is the zero line where no difference is seen.

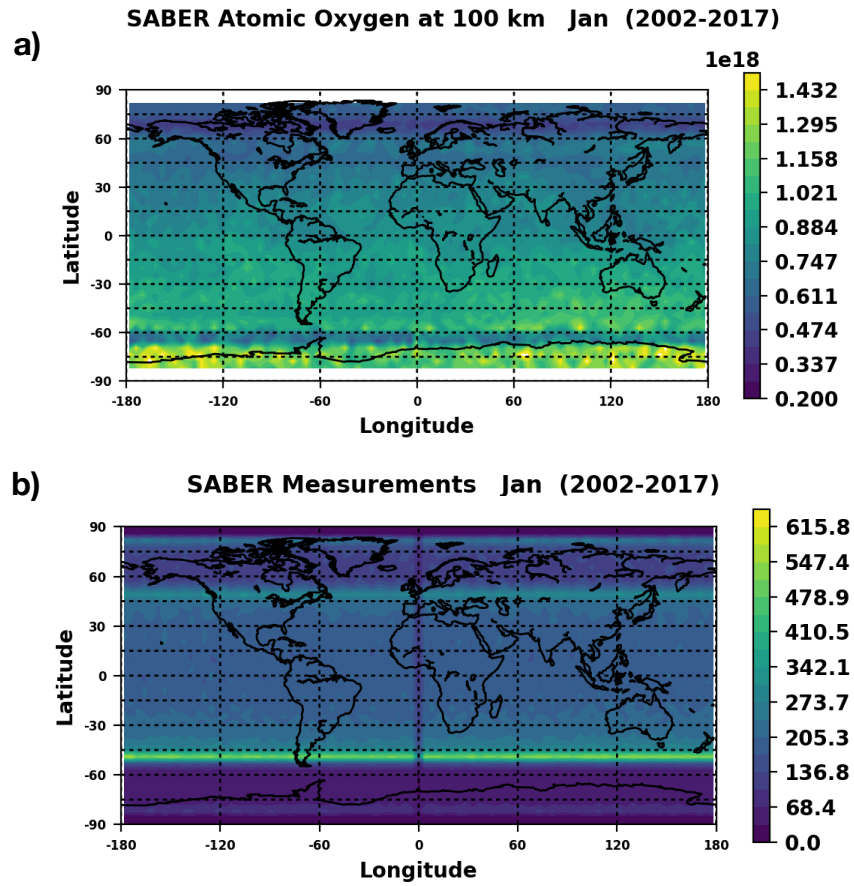


Figure 2. a) Atomic oxygen for SABER in number m^{-3} at 100 km for the month of January binned together for the years 2002-2017. The bin size is $4^\circ \times 4^\circ$. b) Number of measurements in each bin for the month of January for 2002-2017.

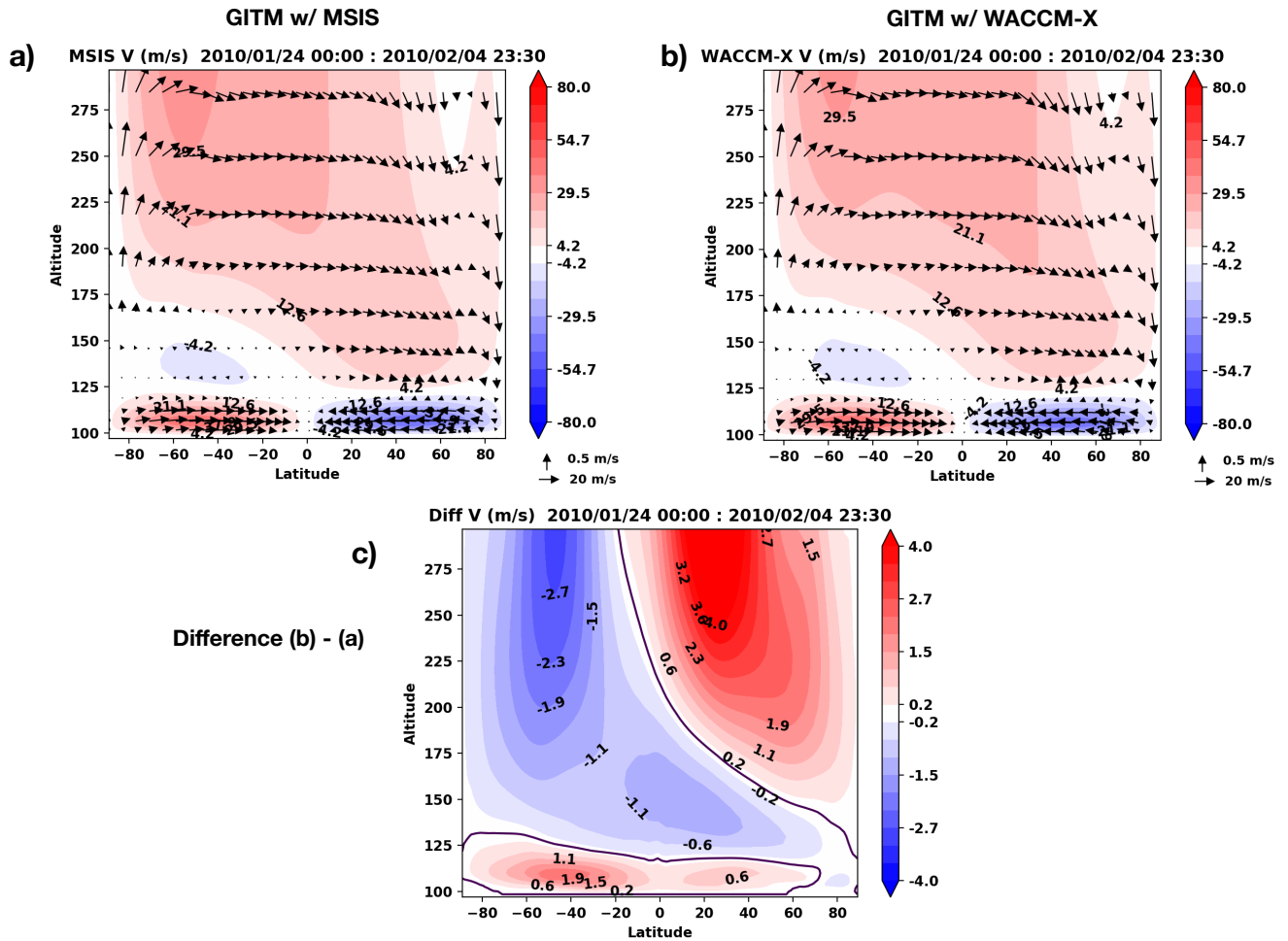


Figure 3. a) The contours indicate the zonally averaged meridional wind in m/s for GITM w/ MSIS averaged for 01/24/2010 - 02/04/2010. Positive values indicate northward wind while negative values indicate southward wind. The arrows signify a vector sum of meridional and vertical winds (scaled by $\times 50$). b) Similar to a) but for GITM w/ WACCM-X. c) Averaged difference in meridional winds, GITM w/ WACCM-X (b) - GITM w/ MSIS (a). Note the thicker black contour line. This is the zero line where no difference is seen.

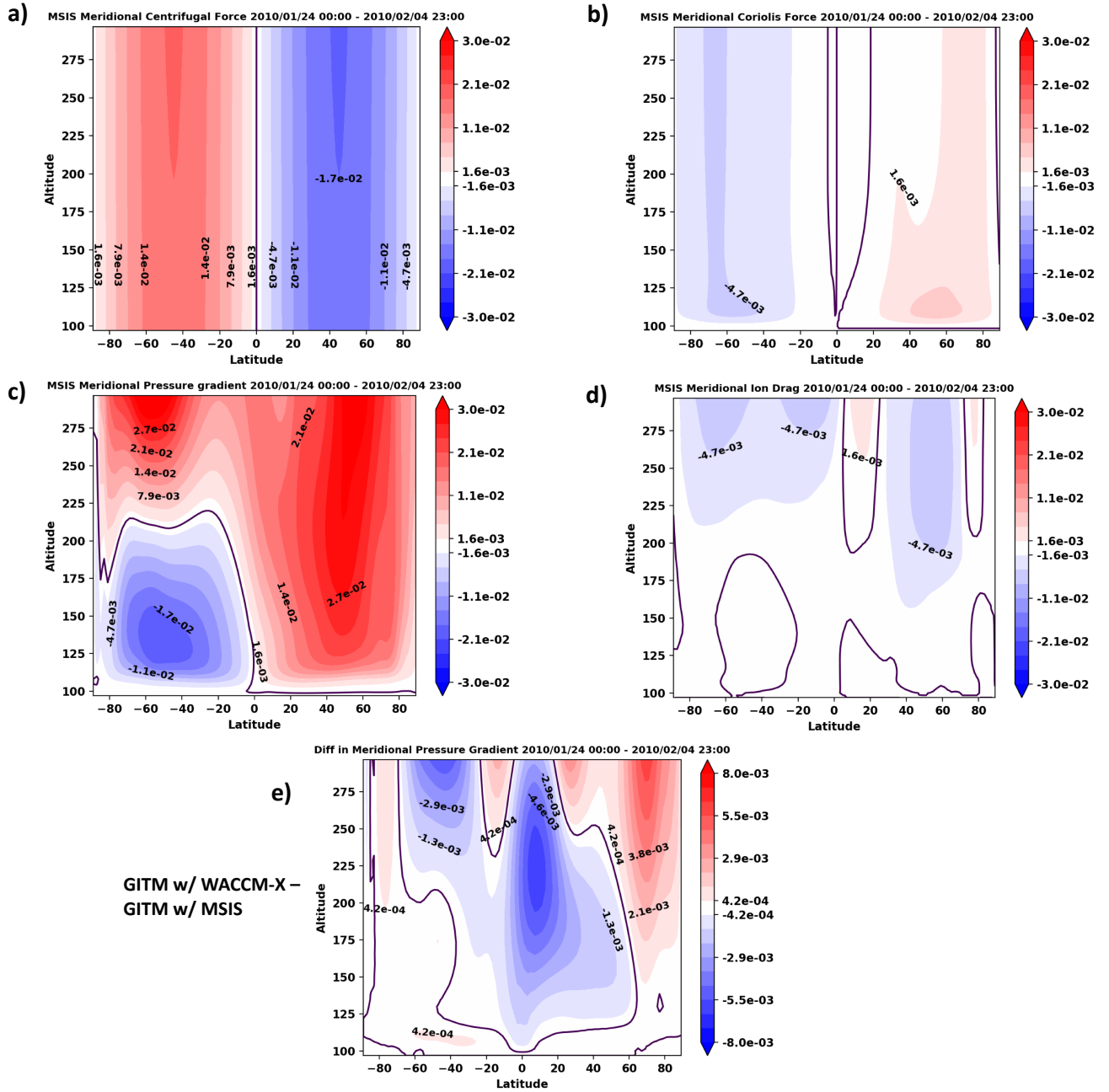


Figure 4. a) The contours indicate the force terms of northward momentum equation in m/s^2 for GITM w/ MSIS, zonally averaged for 01/24/2010 - 02/04/2010. b) Similar to a) but for Coriolis force. c) Similar to a) but for pressure gradient force. Positive values indicate that the pressure is increasing from north to south. d) Similar to a) but for Ion Drag. e) Averaged difference in meridional pressure gradient forces, GITM w/ WACCM-X - GITM w/ MSIS. Note the thicker black contour line. This is the zero line where no difference is seen.

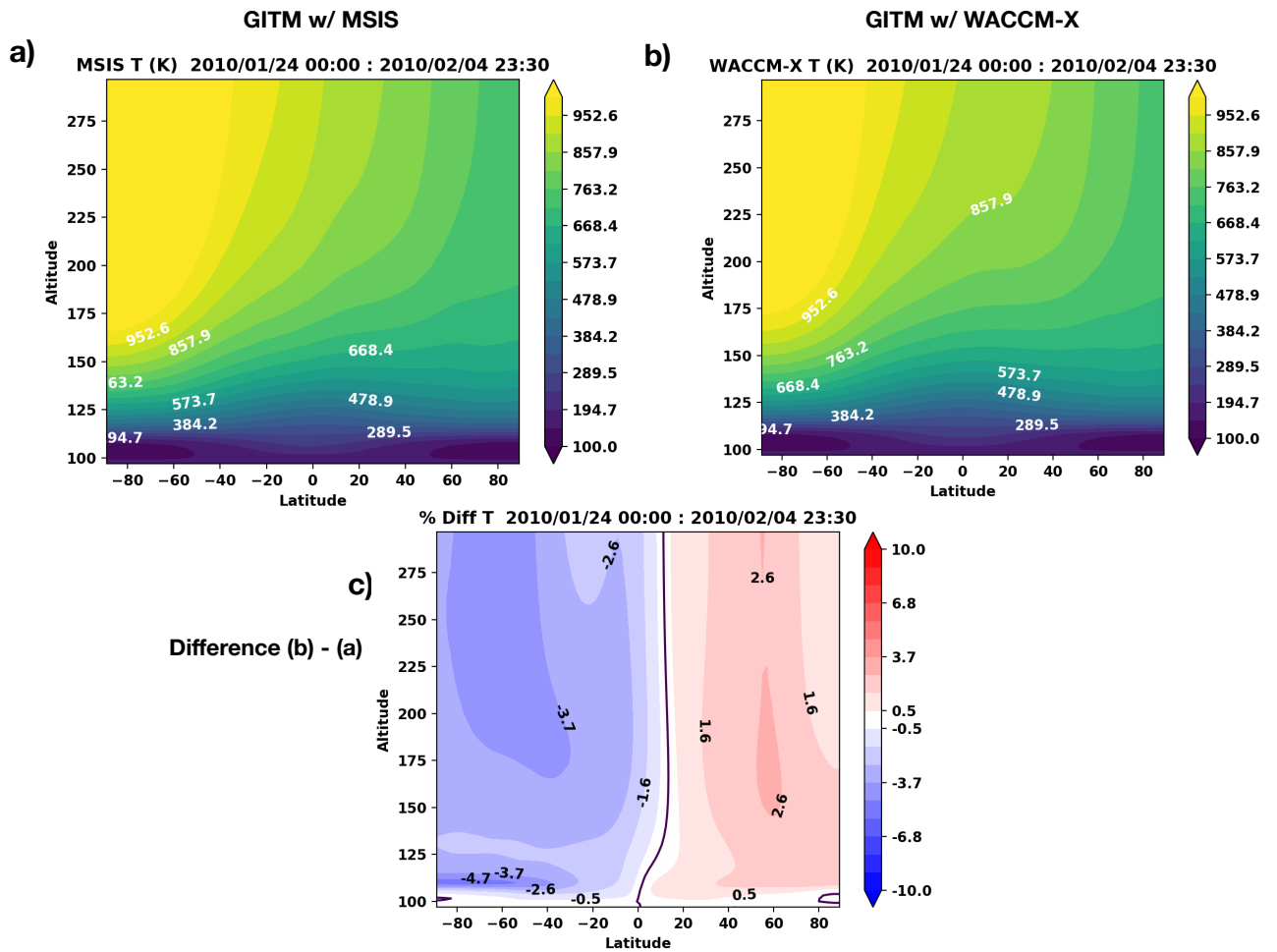


Figure 5. a) The contours indicate the temperature in K for GITM w/ MSIS zonally averaged for 01/24/2010 - 02/04/2010. b) Similar to a) but for GITM w/ WACCM-X. c) Zonally averaged percentage difference in temperatures GITM w/ WACCM-X (b) - GITM w/ MSIS (a). Note the thicker black contour line. This is the zero line where no difference is seen.

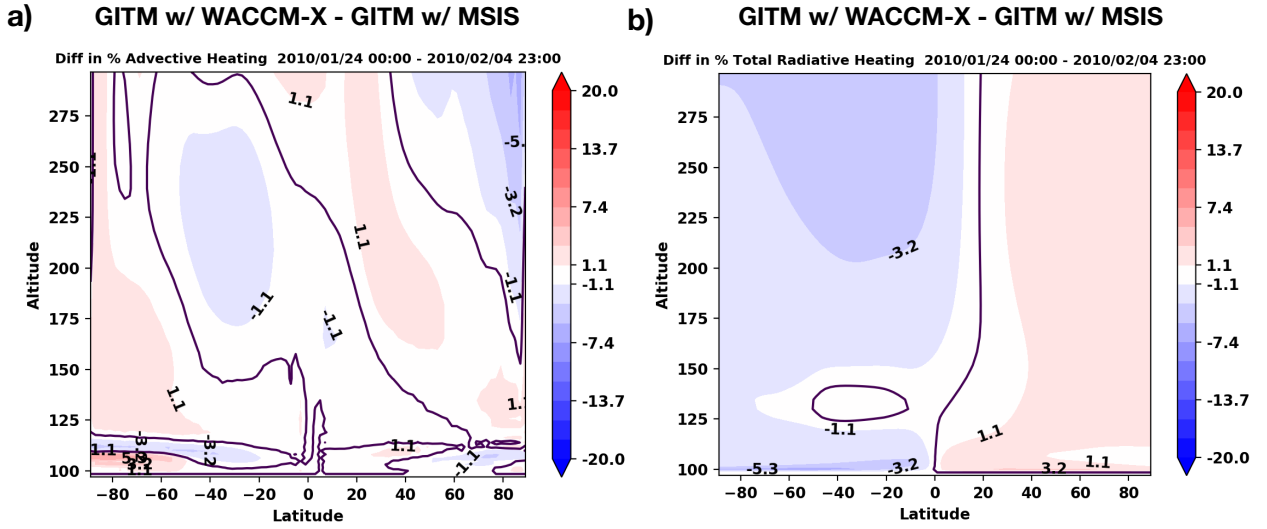


Figure 7. a) The contours indicate the difference in percent Advection heating per day (normalized by temperature), GITM w/ WACCM-X - GITM w/ MSIS, zonally averaged for 01/24/2010 - 02/04/2010. b) Similar to a) but for Radiative heating. Note the thicker black contour line. This is the zero line where no difference is seen.

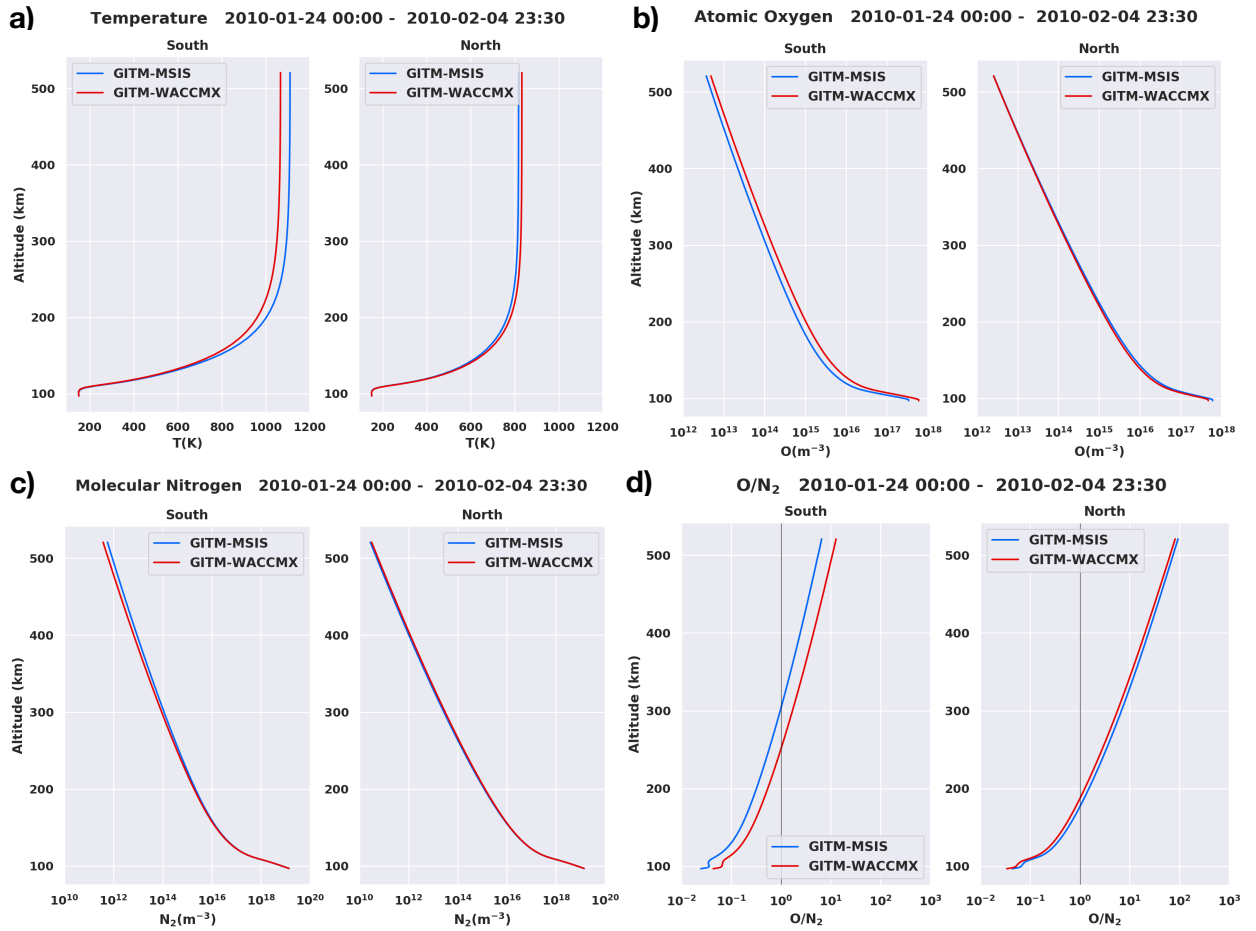


Figure 8. Height profile for a) Temperature (K), b) Atomic Oxygen (m^{-3}), c) Molecular Nitrogen (m^{-3}), d) O/N_2 averaged for 01/24/2010 - 02/04/2010. The x-axis indicates the values of each parameter while y-axis is the altitude. The red (blue) curves are for GITM w/ WACCM-X (MSIS). Each parameter is divided into northern and southern hemisphere, and cosine-weighted averaged for latitudes $30^\circ - 90^\circ$. The black vertical line in d) indicates where O/N_2 is 1

Percentage Difference in Means (WACCMX-MSIS) 2010-01-24 00:00 - 2010-02-04 23:30

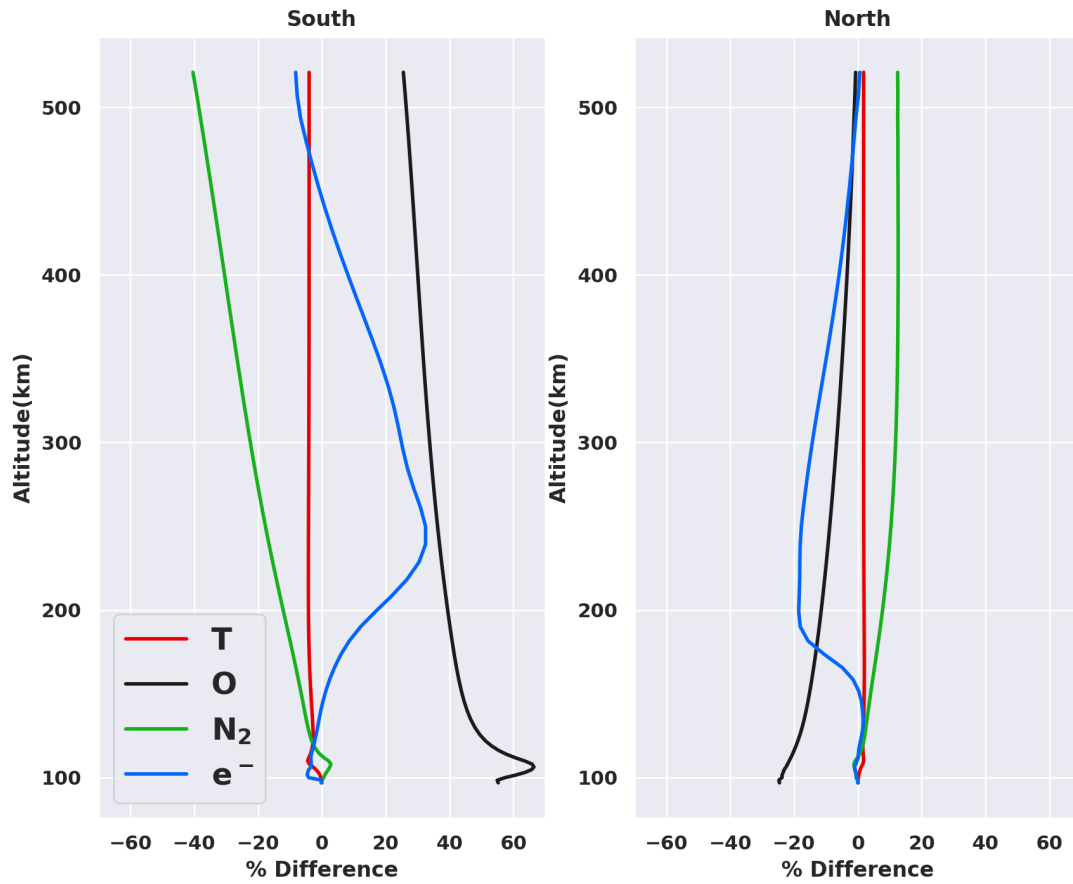


Figure 9. Height profile for the percentage difference in GITM w/ WACCM-X - GITM w/ MSIS for Temperature (red), O (black), N₂ (green), electron density (blue). These profiles are averaged for 01/24/2010 - 02/04/2010 and cosine-weighted averaged for latitudes 30° - 90° and divided into northern and southern hemisphere.

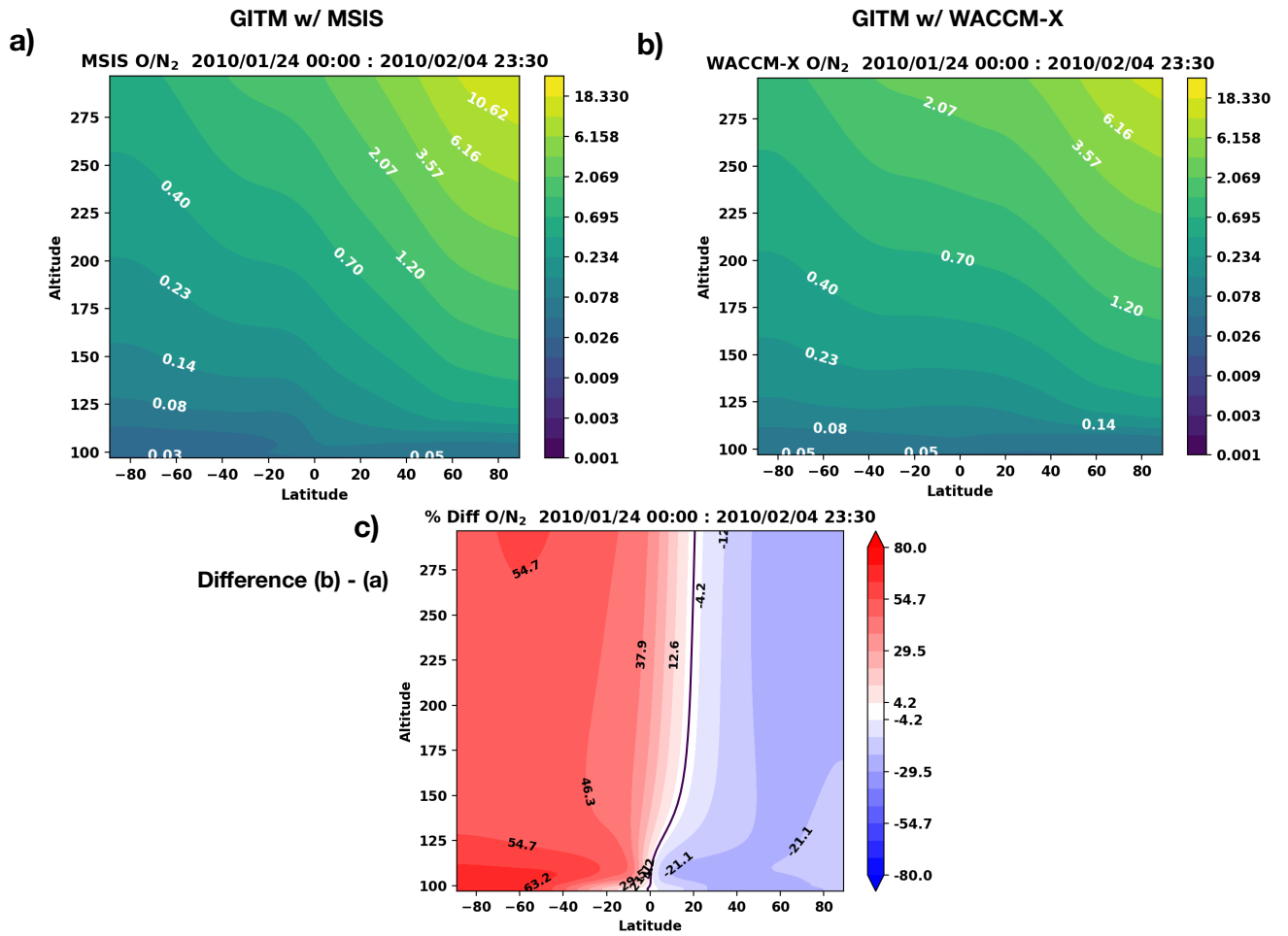


Figure 10. a) The contours indicate the O/N₂ for GITM w/ MSIS averaged for 01/24/2010 - 02/04/2010 using a logarithmic colorscale. b) Similar to a) but for GITM w/ WACCM-X. c) Averaged Difference in O/N₂ GITM w/ WACCM-X (b) - GITM w/ MSIS (a). Note the thicker black contour line. This is the zero line where no difference is seen.

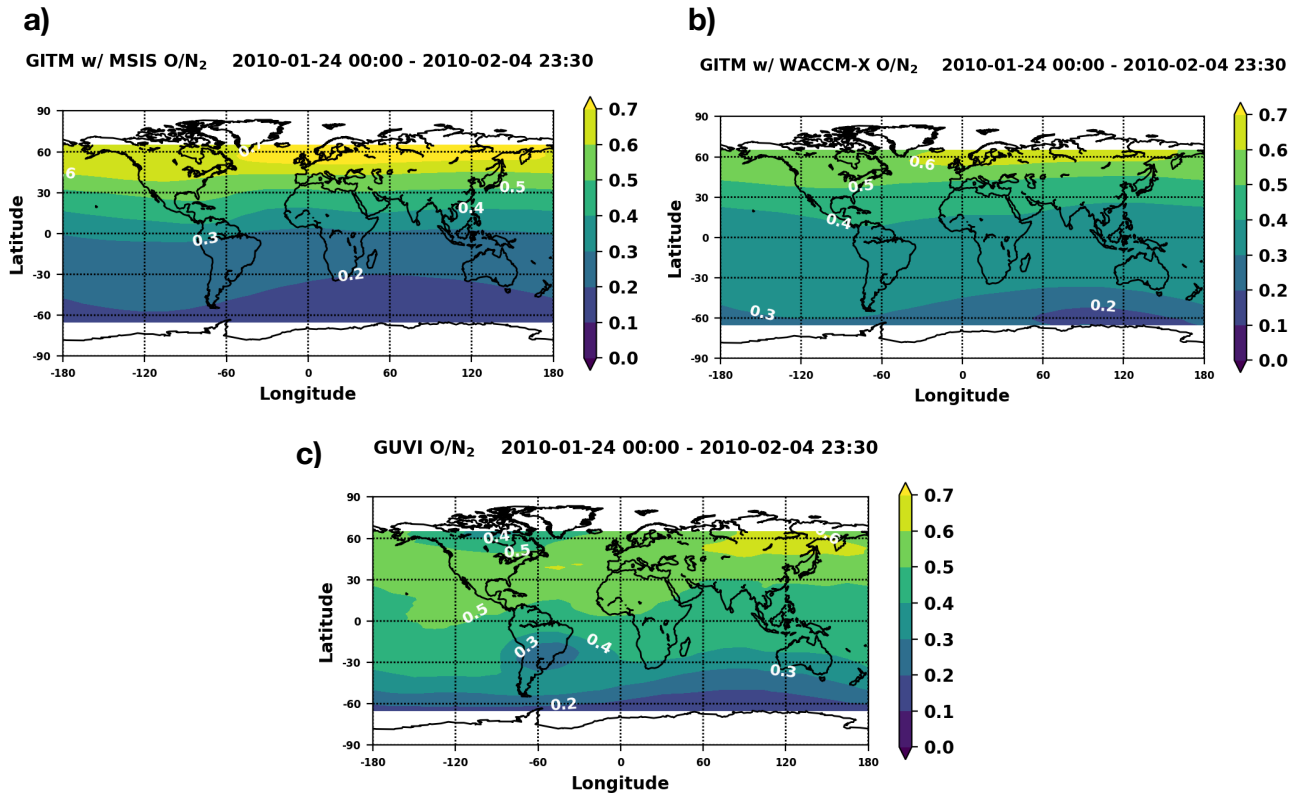


Figure 11. Integrated O/N₂ with a reference altitude of 10^{17} cm^{-2} for a) GITM w/ MSIS, b) GITM w/ WACCM-X, c) TIMED GUVI data. The O/N₂ in GITM are sampled at GUVI times and locations.

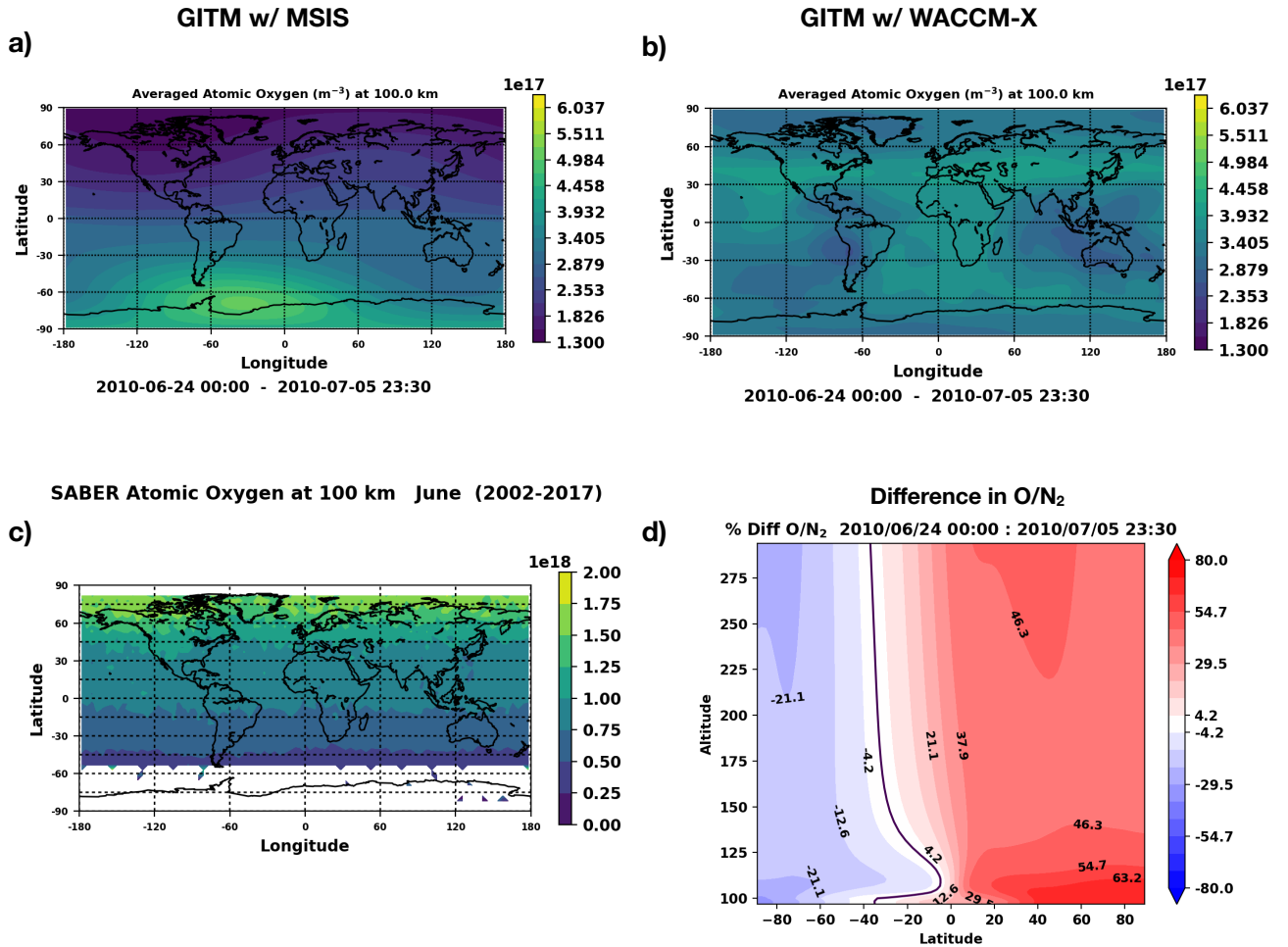


Figure 12. Atomic Oxygen (m⁻³) at 100 km averaged from 06/24/2010 - 07/05/2010 for a) GITM w/ MSIS, b) GITM w/ WACCM-X. c) Atomic Oxygen for SABER in m⁻³ interpolated at 100 km for the month of January binned together for the years 2002-2017. The bin size is 4° × 4°. d) Averaged Difference in O/N₂ GITM w/ WACCM-X - GITM w/ MSIS for 06/24/2010 - 07/05/2010. Note the thicker black contour line. This is the zero line where no difference is seen.

Figure 1.

Author Manuscript

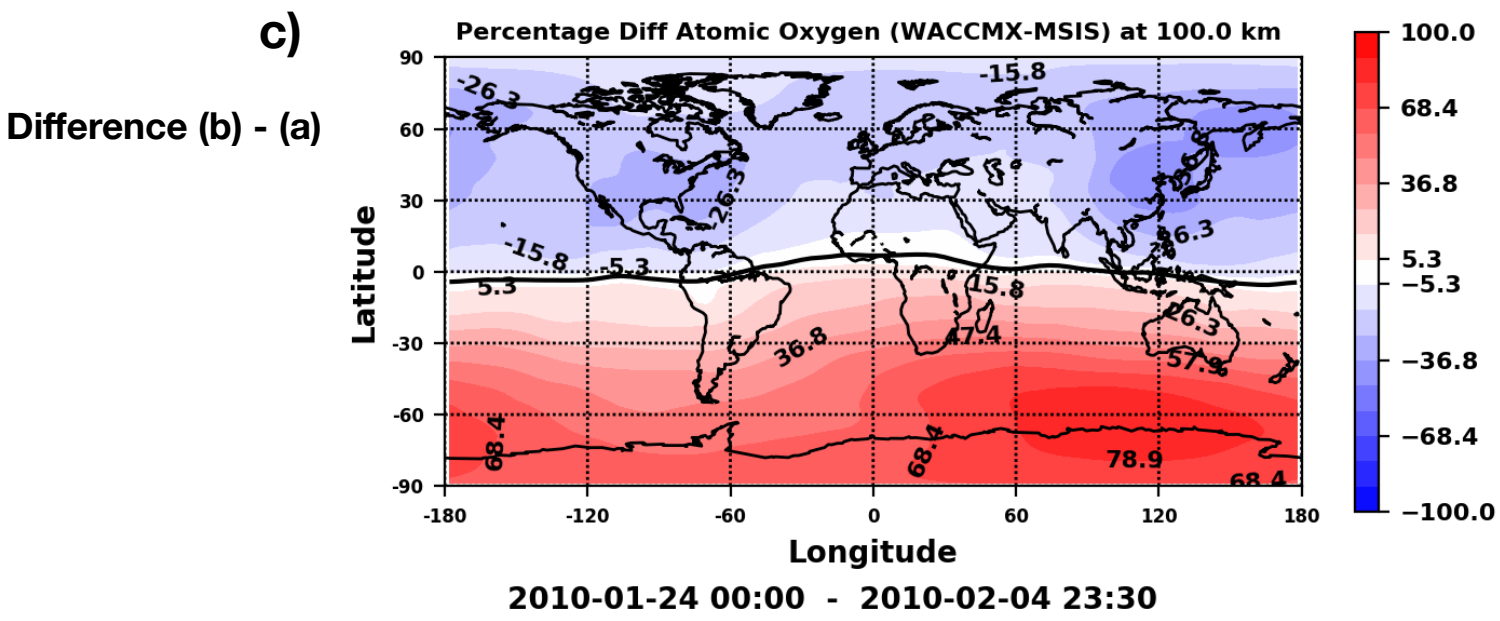
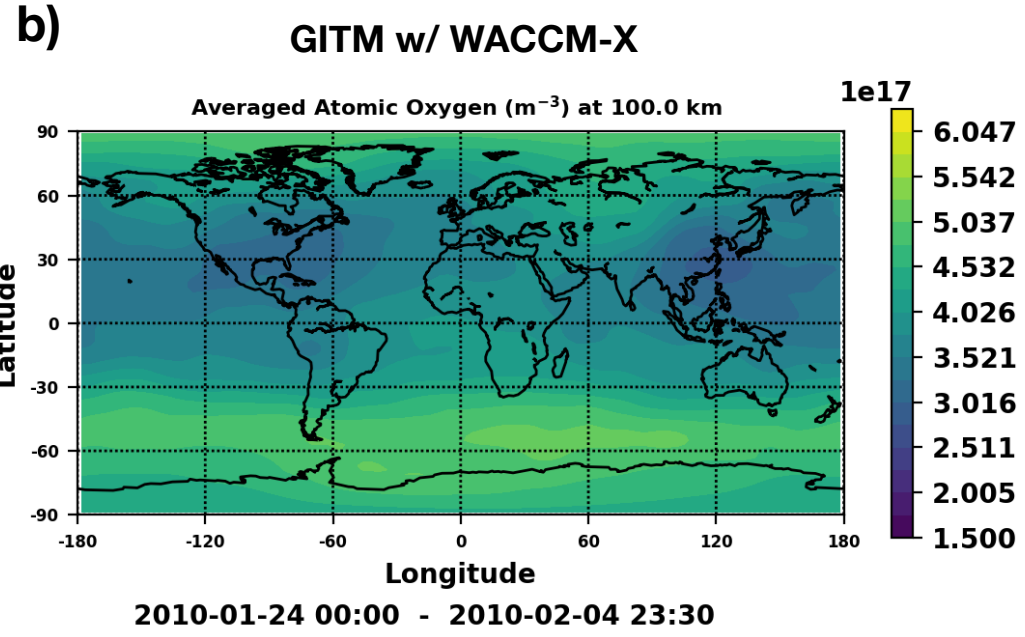
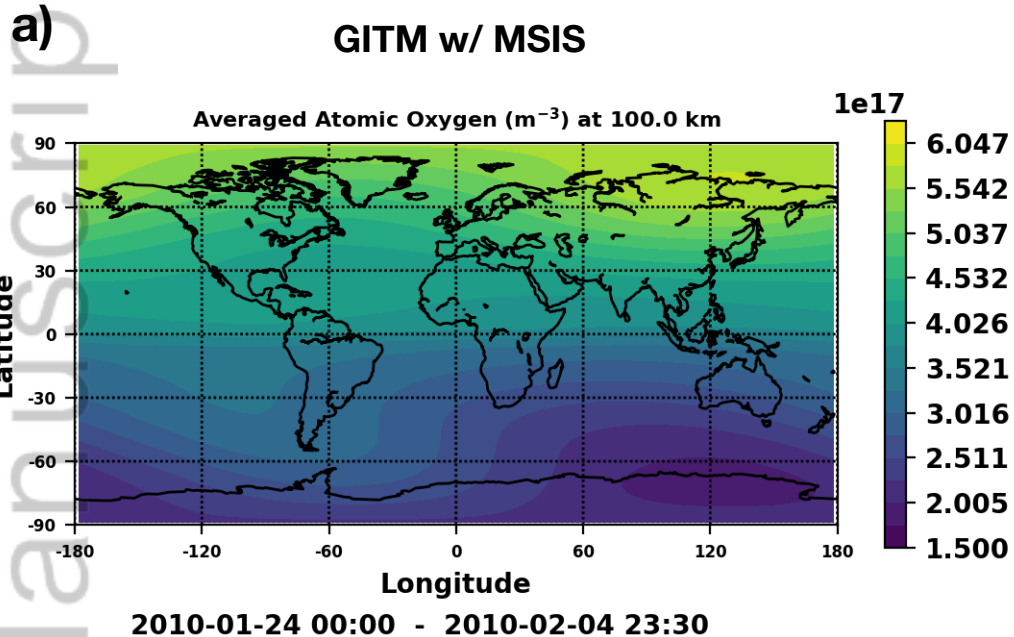
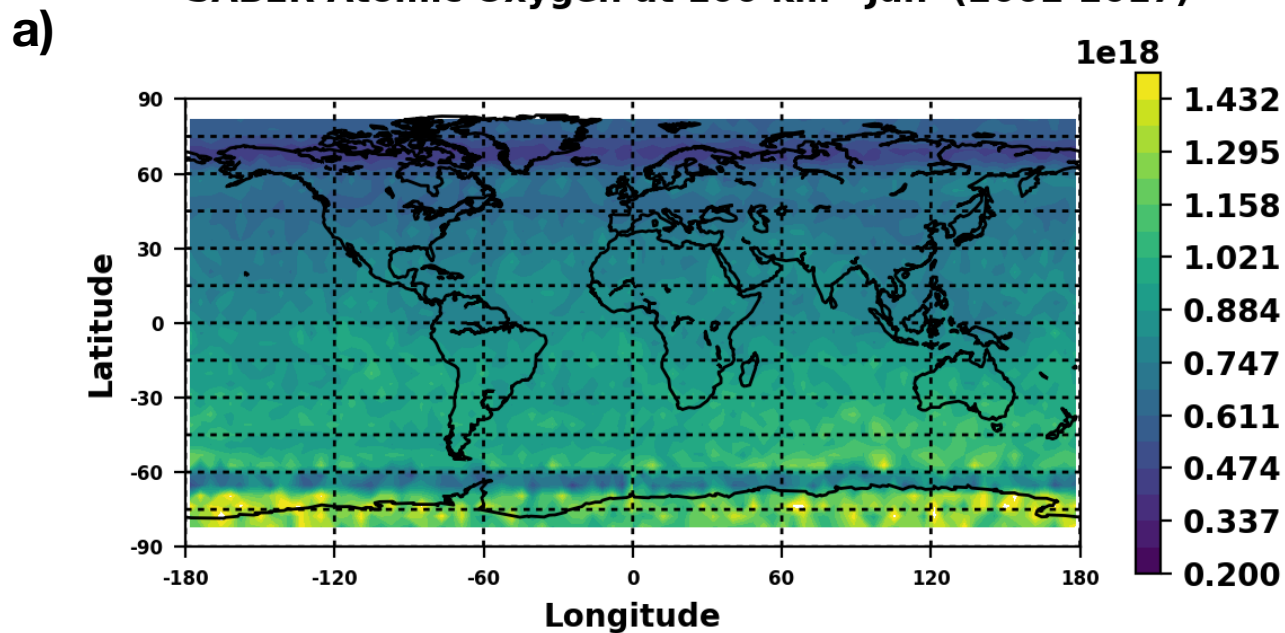


Figure 2.

Author Manuscript

SABER Atomic Oxygen at 100 km Jan (2002-2017)



SABER Measurements Jan (2002-2017)

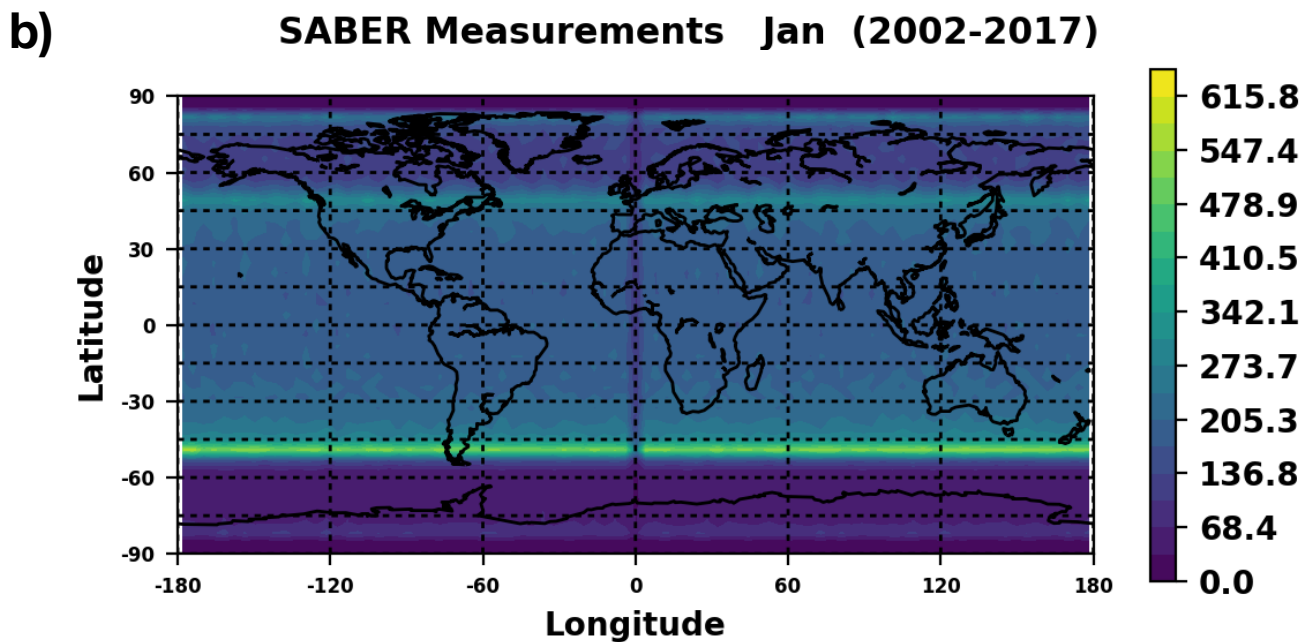


Figure 3.

Author Manuscript

GITM w/ MSIS

GITM w/ WACCM-X

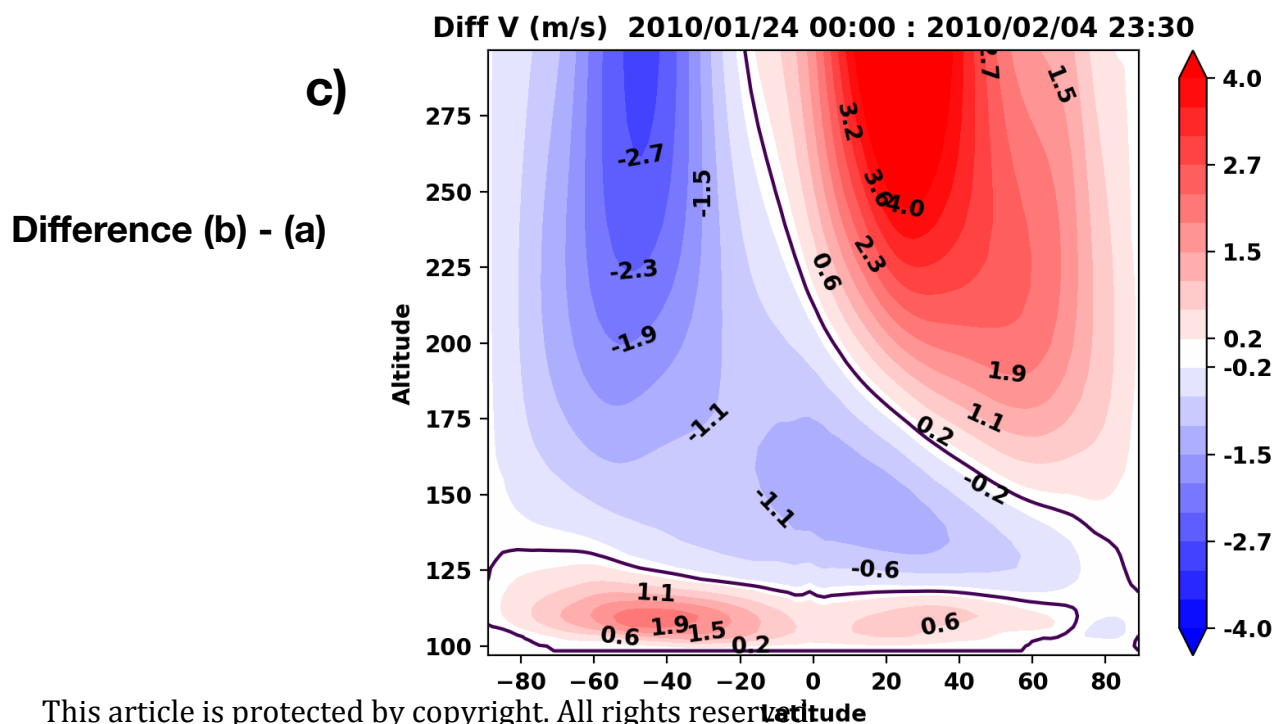
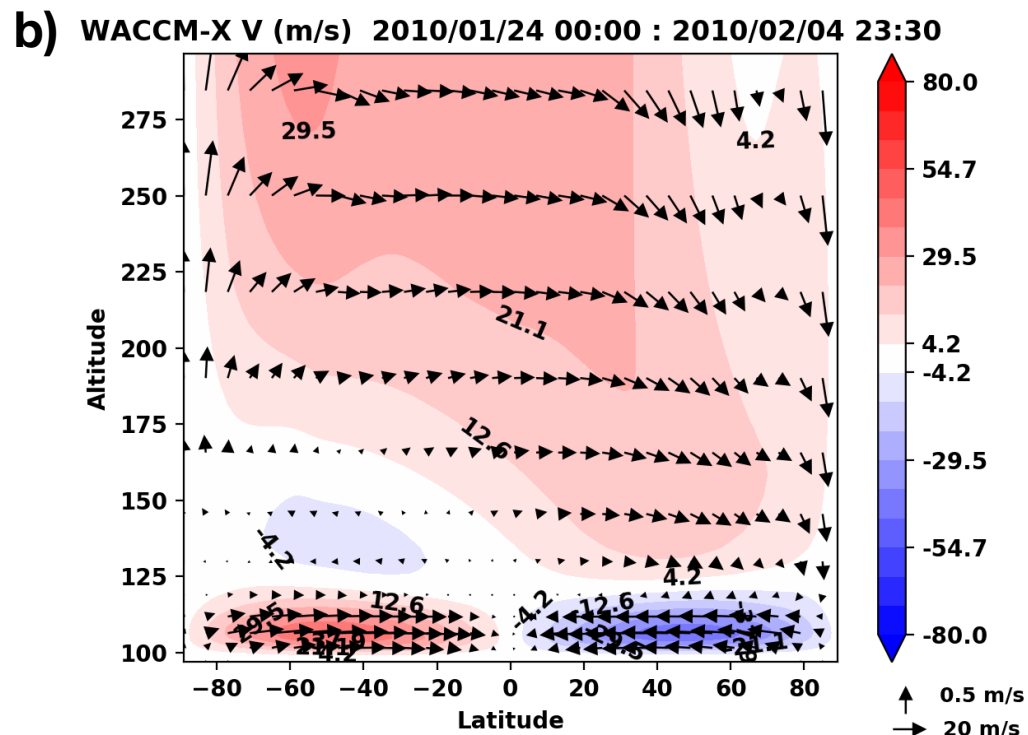
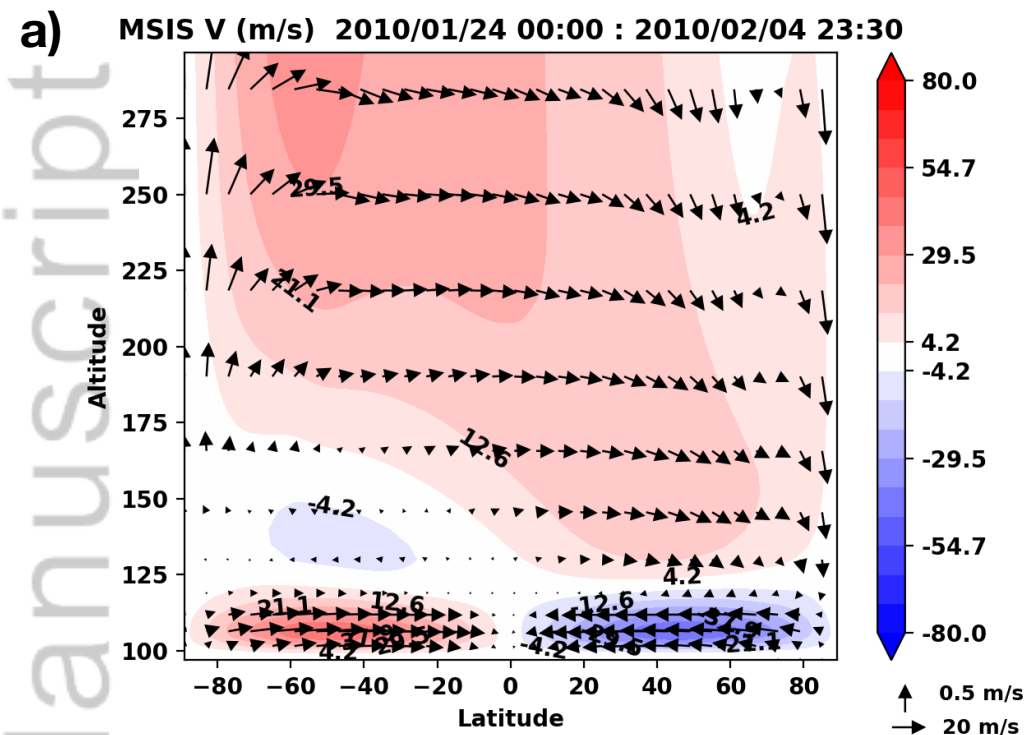


Figure 4.

Author Manuscript

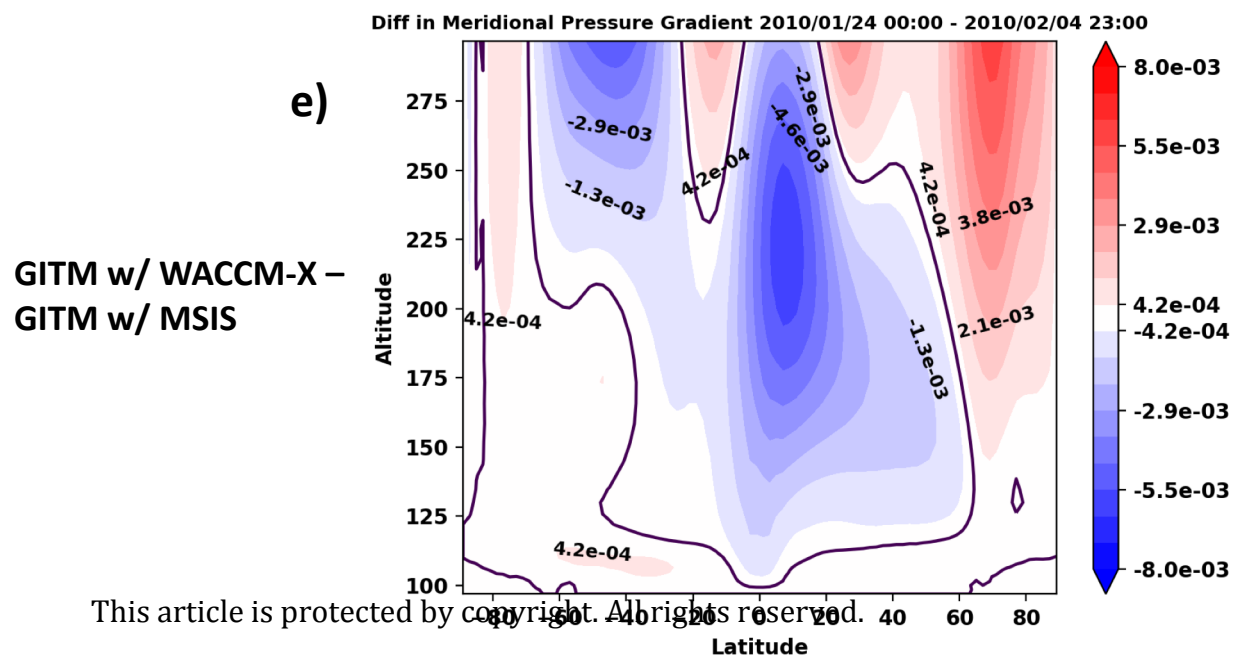
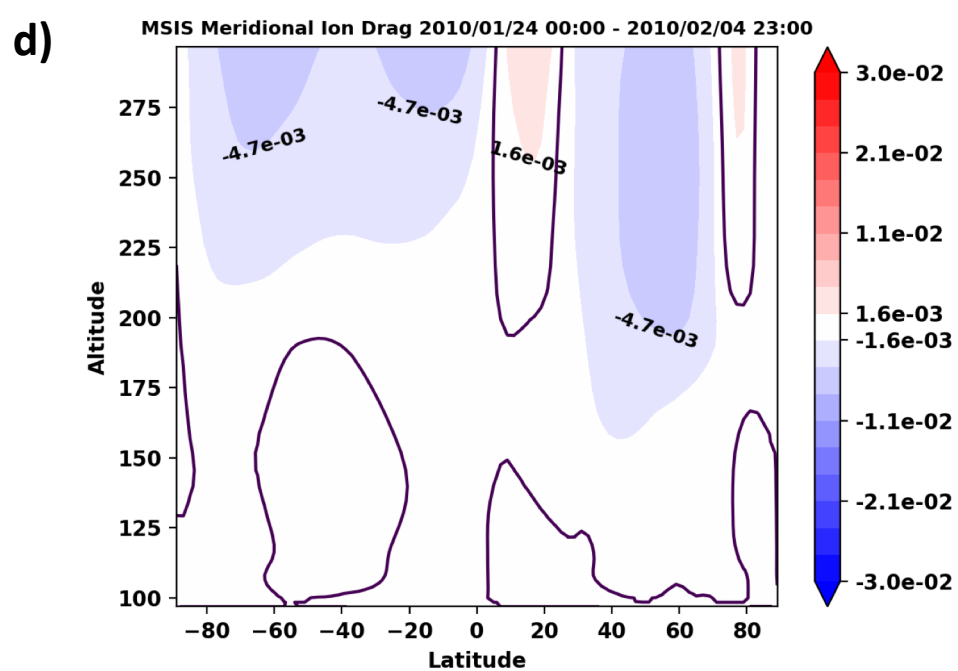
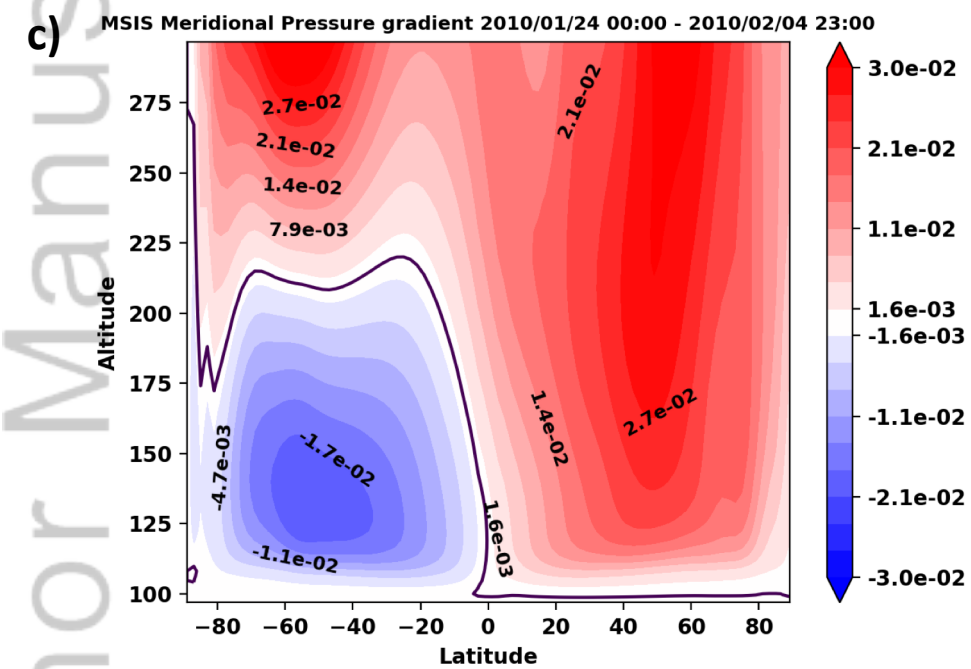
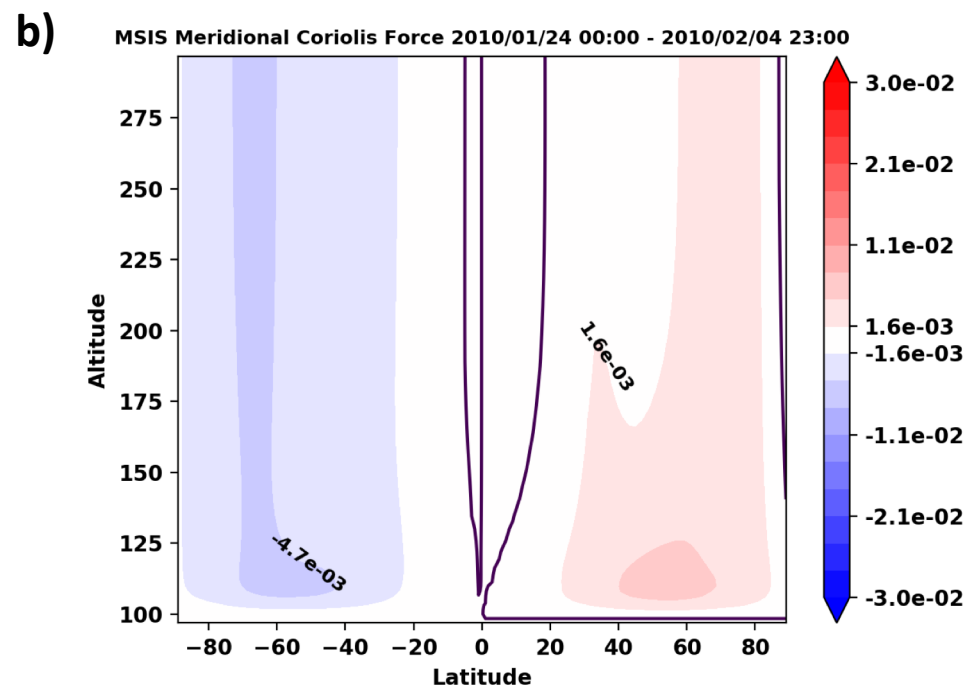
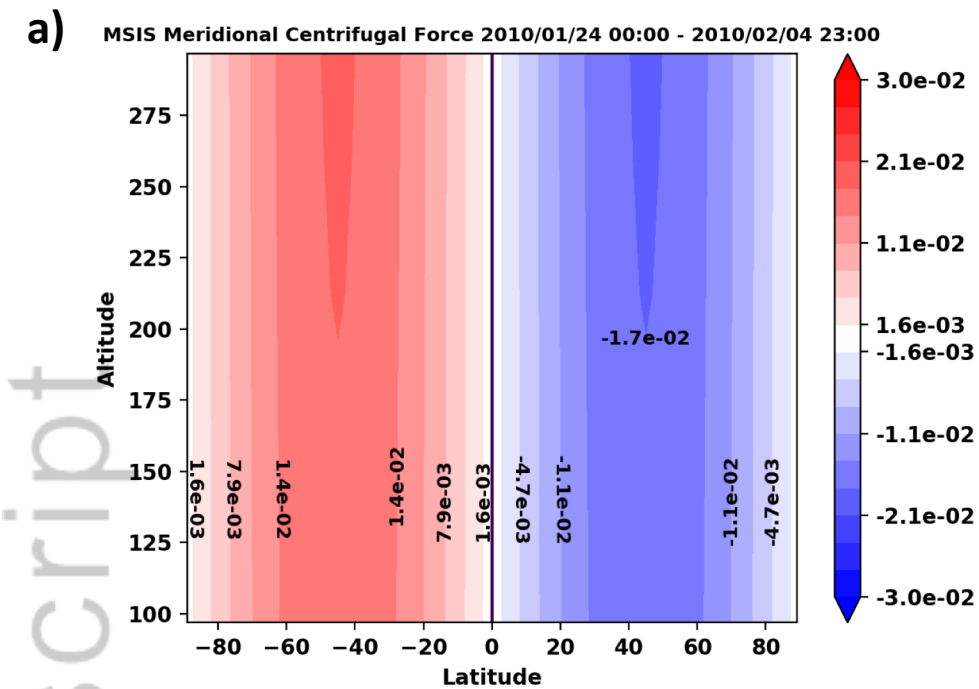


Figure 5.

Author Manuscript

GITM w/ MSIS

GITM w/ WACCM-X

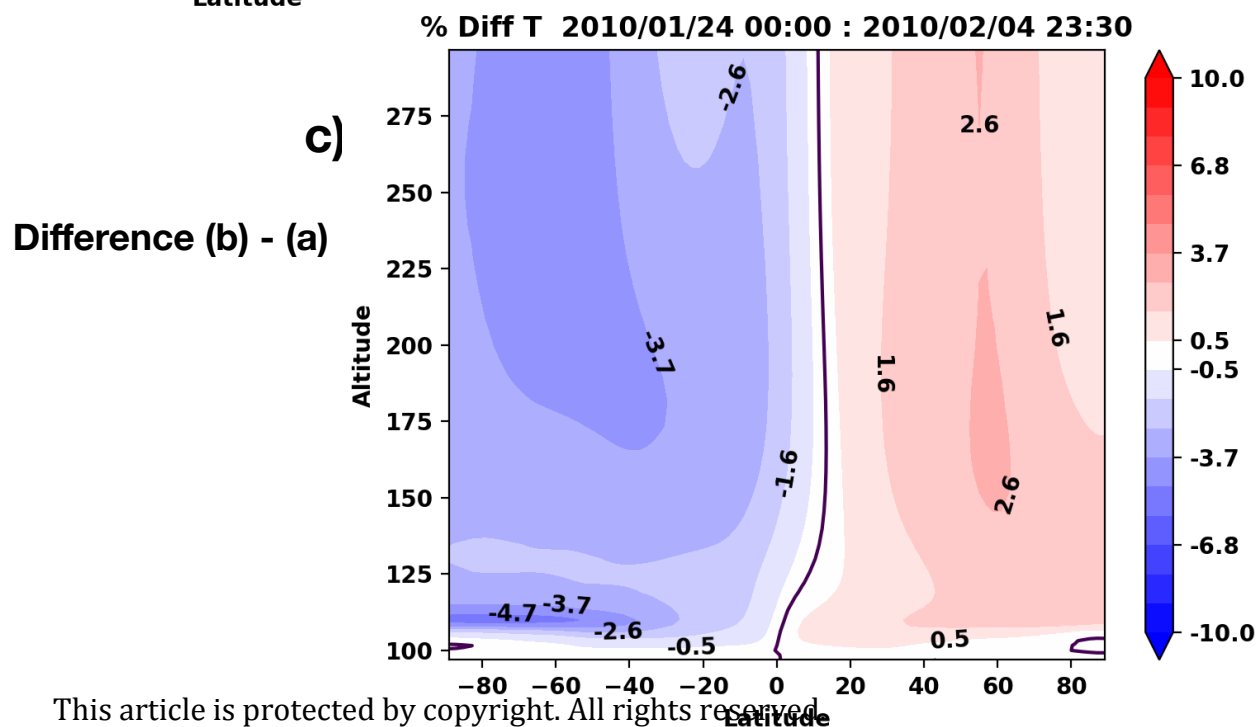
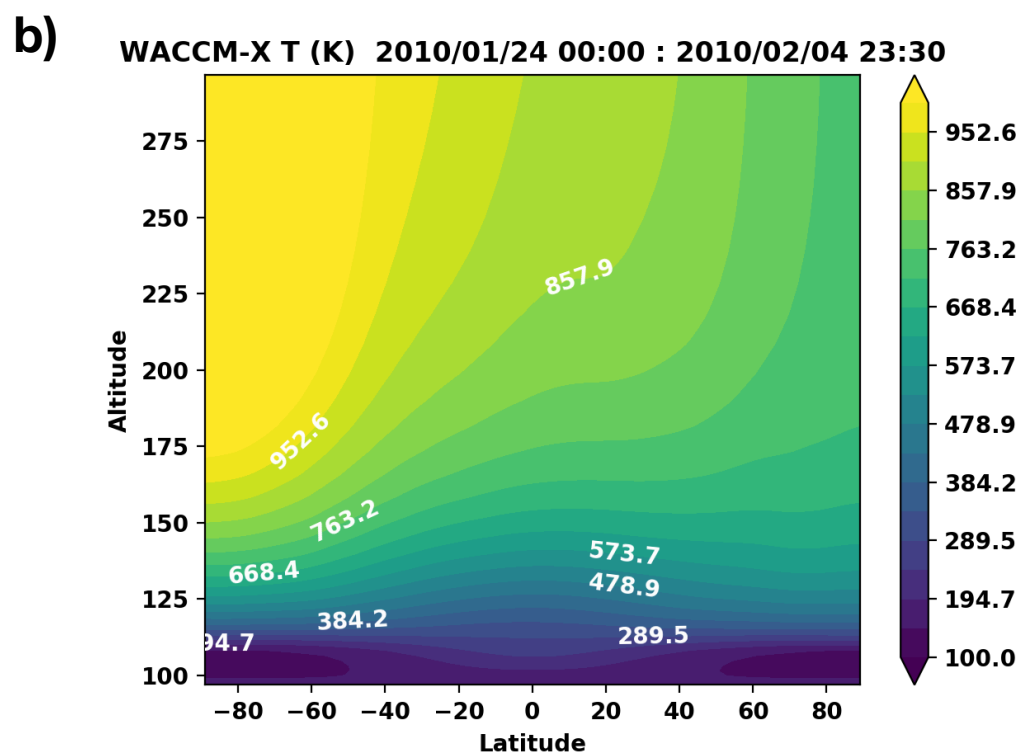
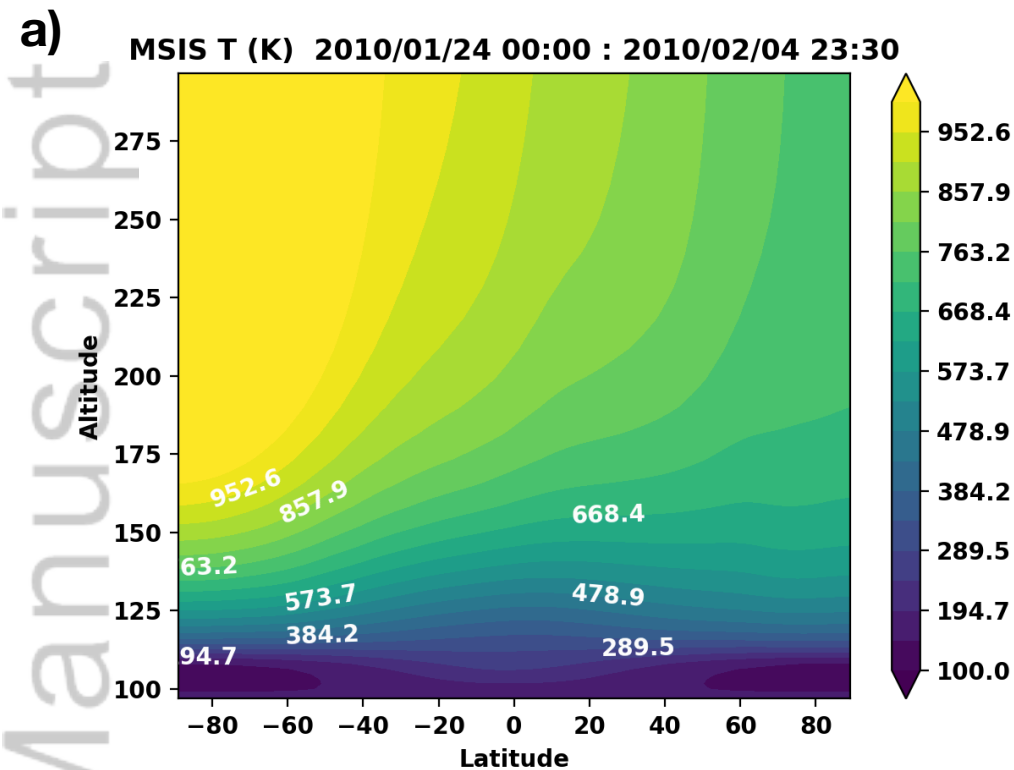


Figure 6.

Author Manuscript

GITM w/ MSIS

GITM w/ WACCM-X

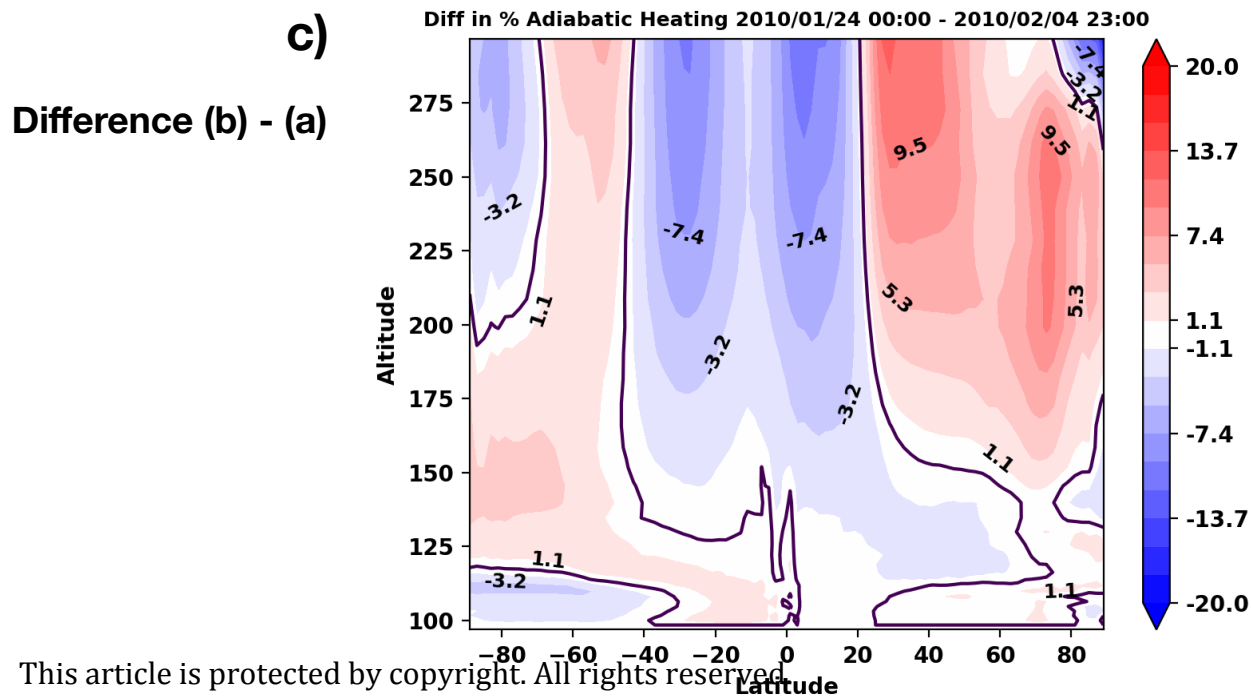
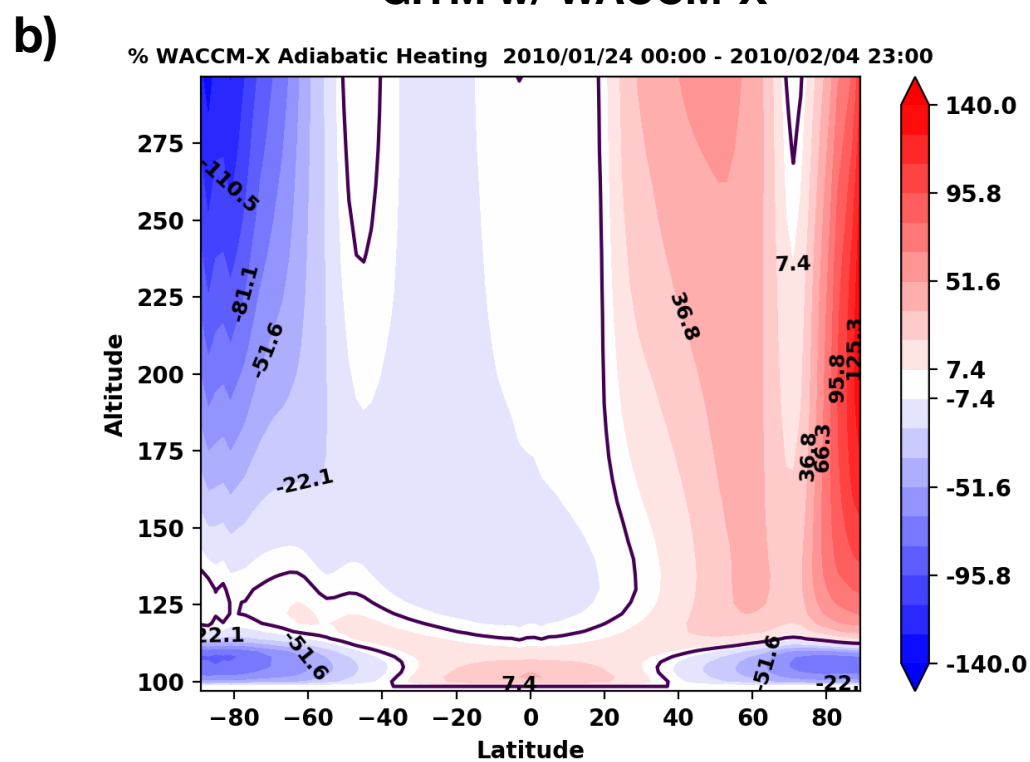
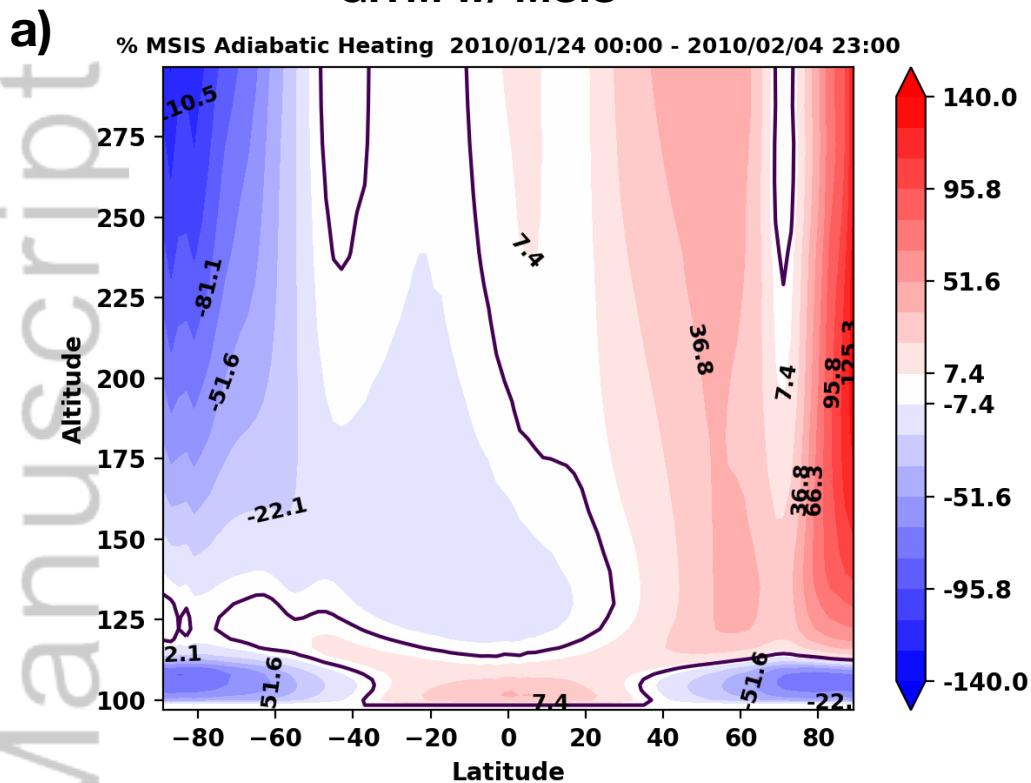
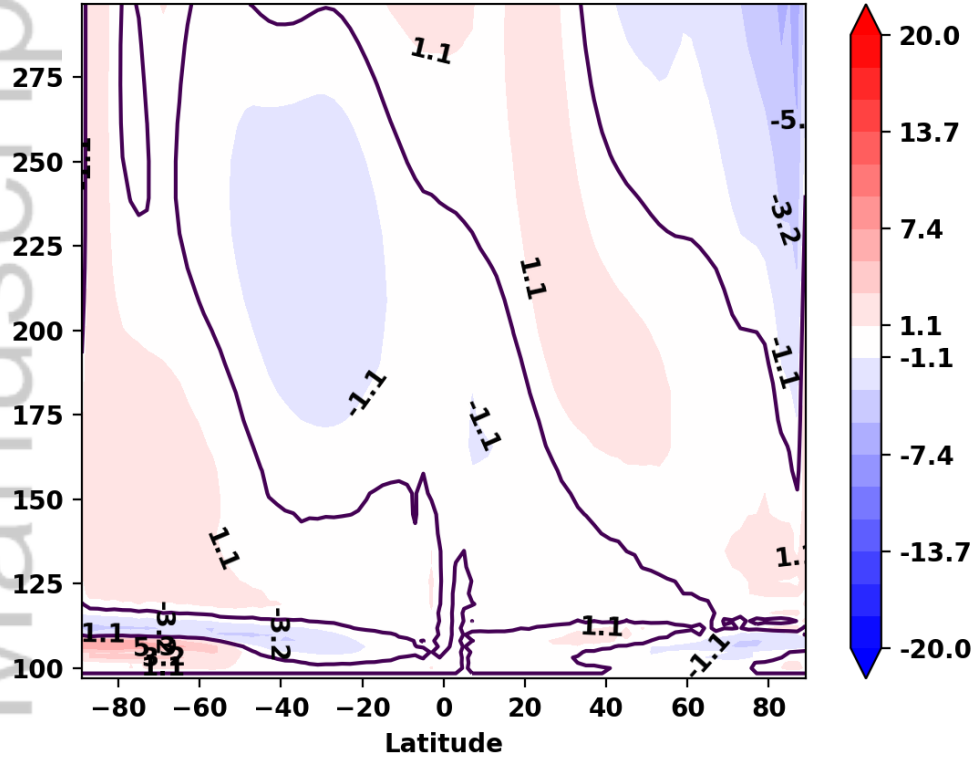


Figure 7.

Author Manuscript

a) GITM w/ WACCM-X - GITM w/ MSIS

Diff in % Advective Heating 2010/01/24 00:00 - 2010/02/04 23:00



b) GITM w/ WACCM-X - GITM w/ MSIS

Diff in % Total Radiative Heating 2010/01/24 00:00 - 2010/02/04 23:00

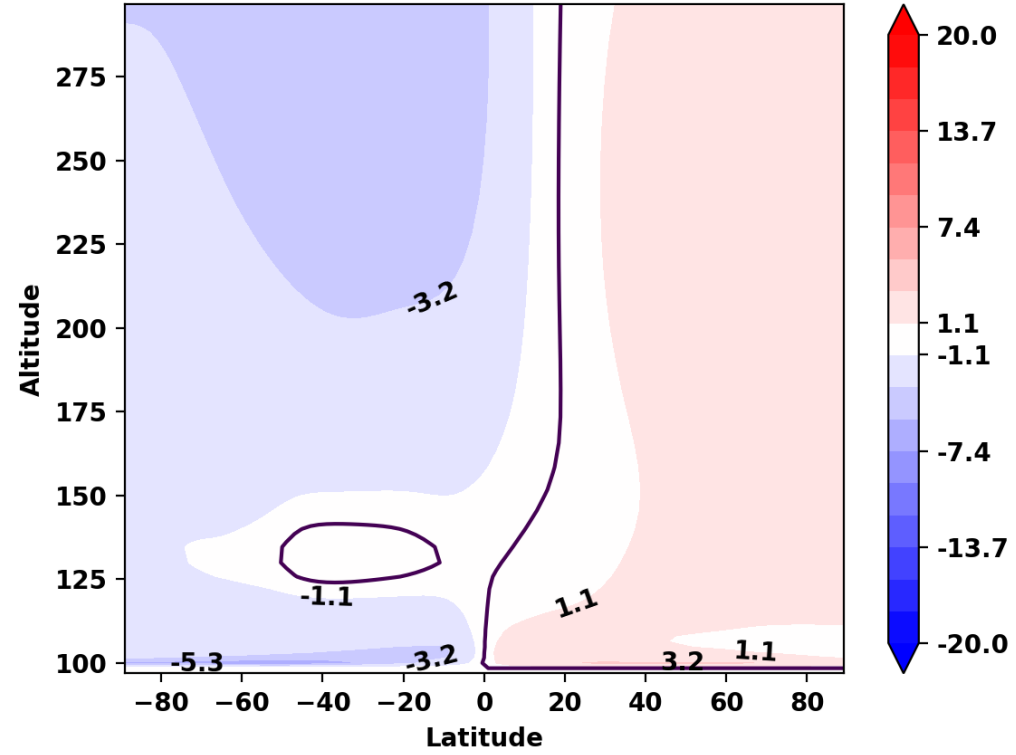


Figure 8.

Author Manuscript

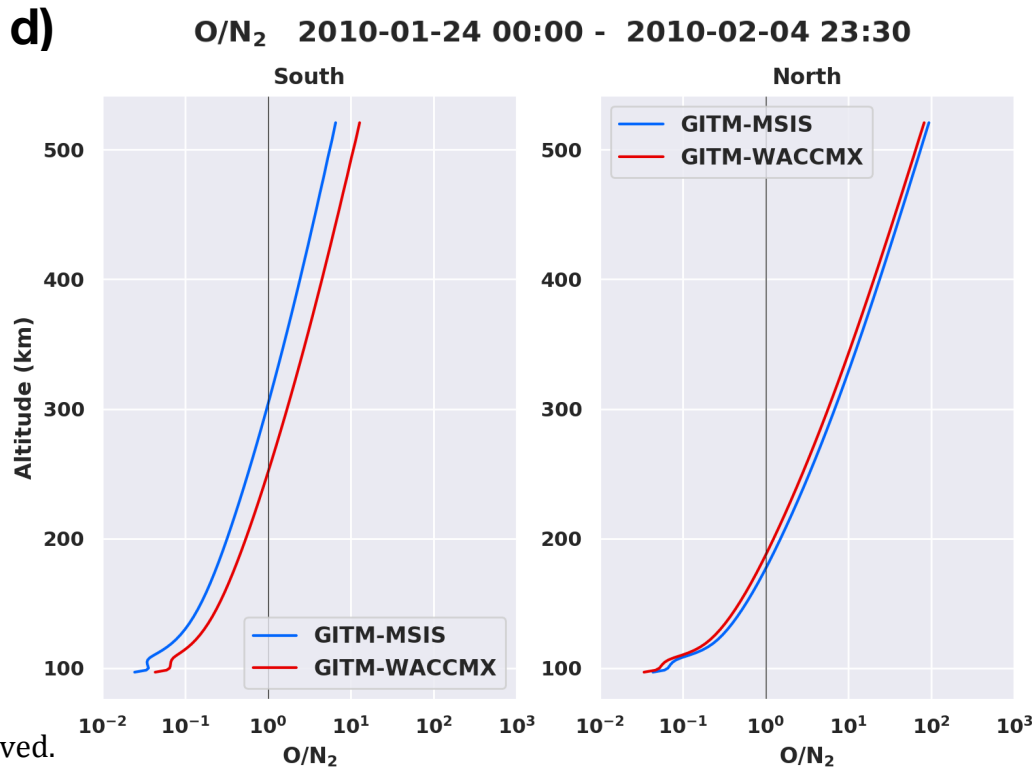
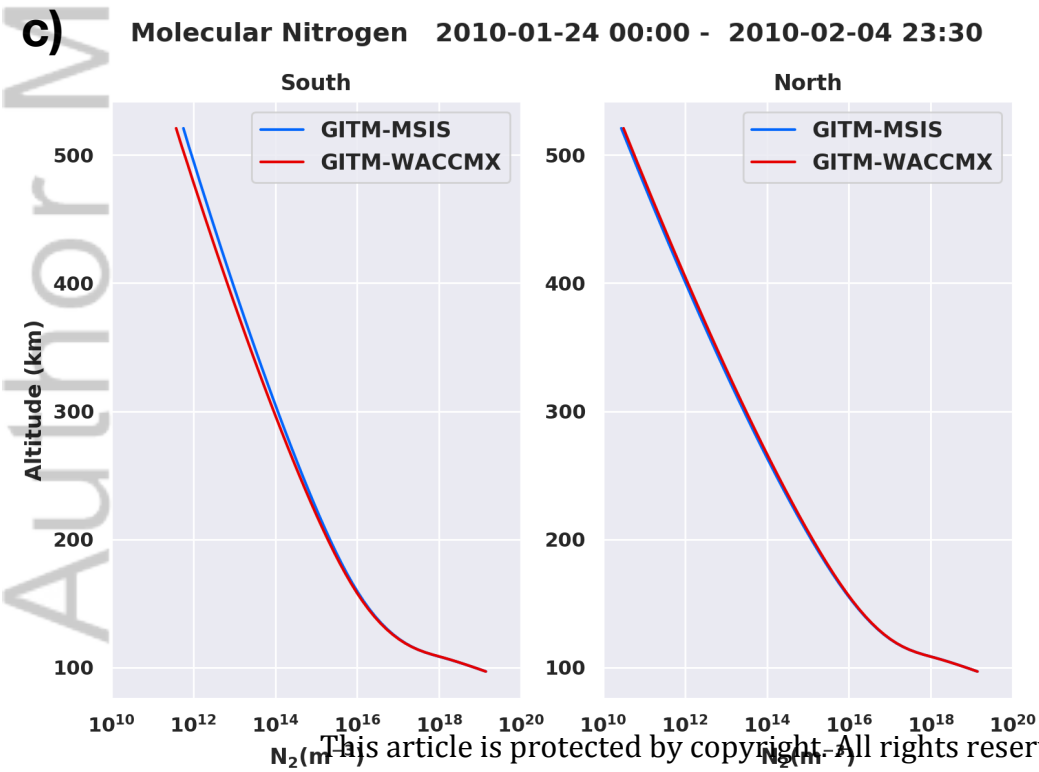
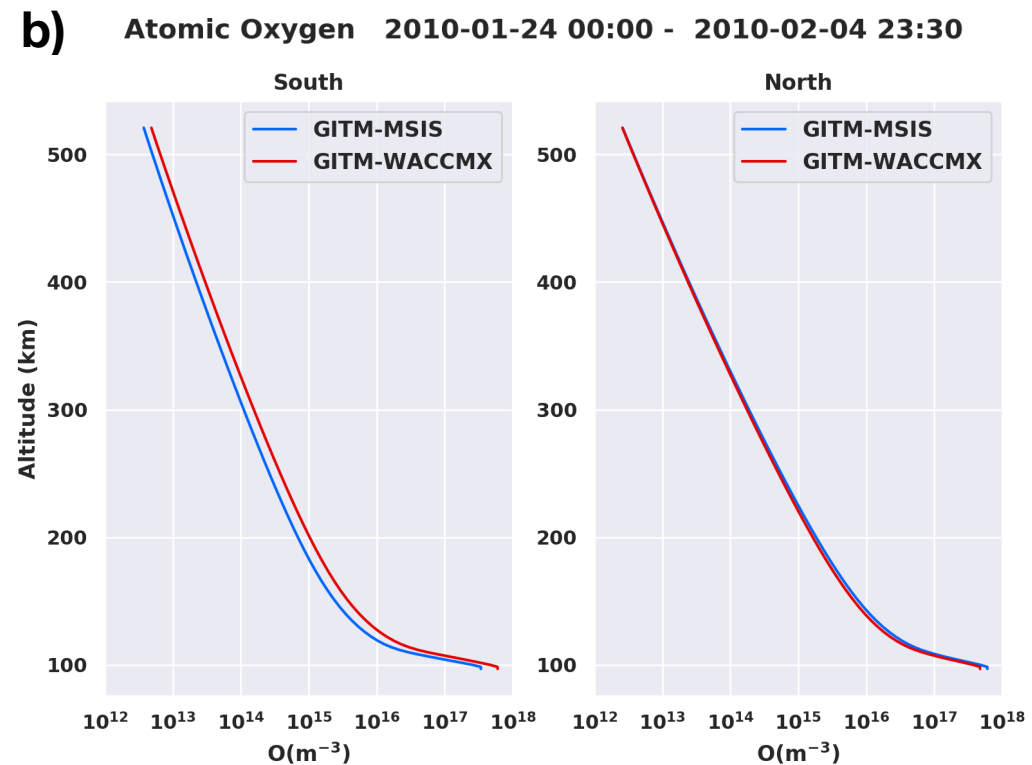
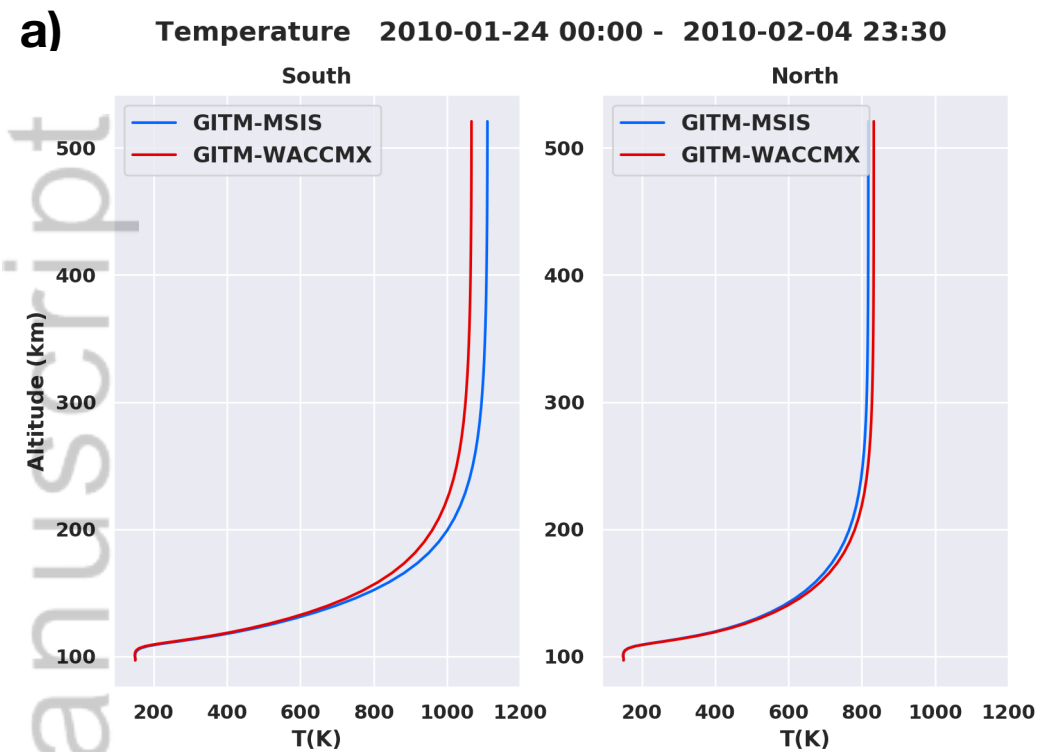


Figure 9.

Author Manuscript

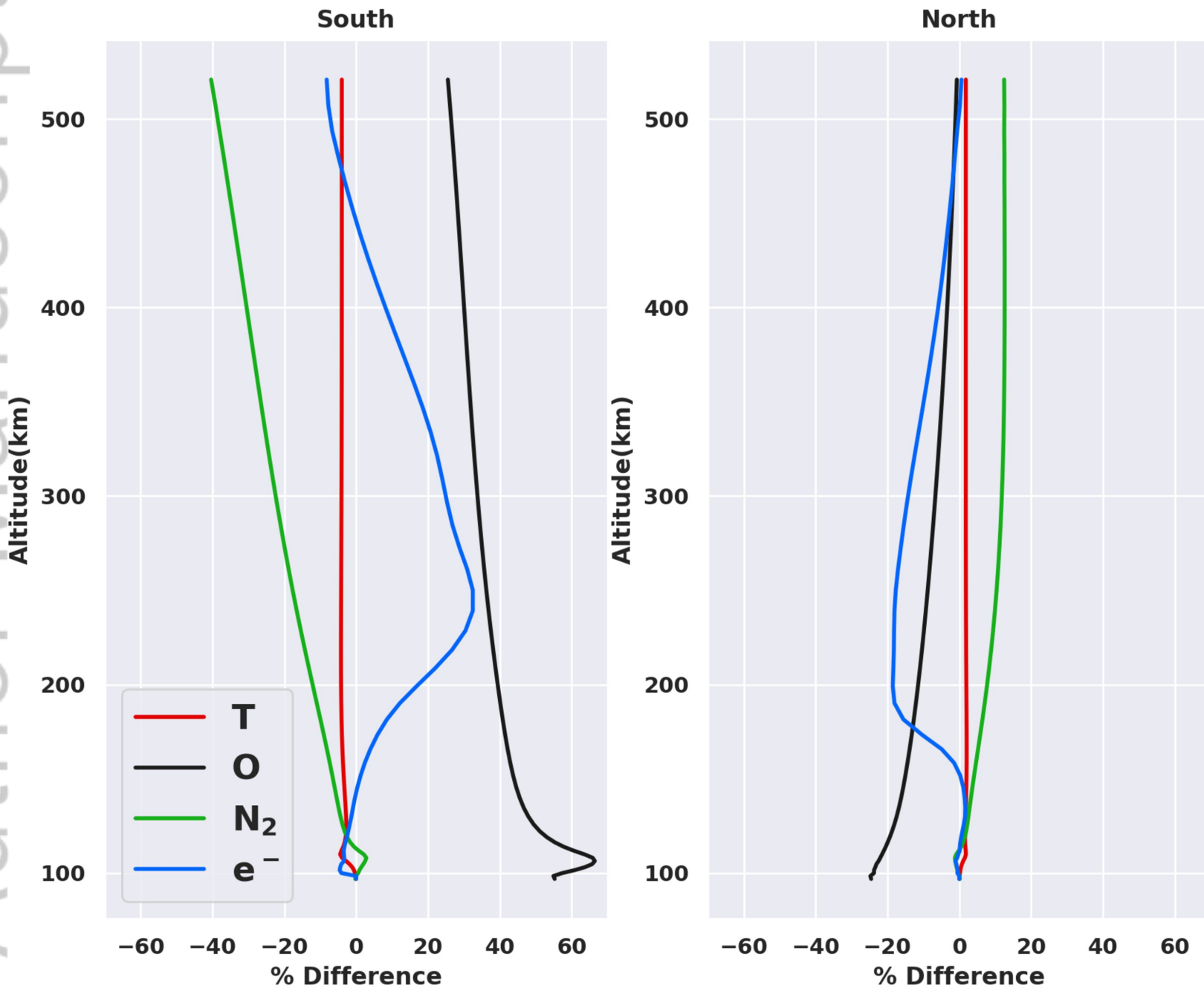


Figure 10.

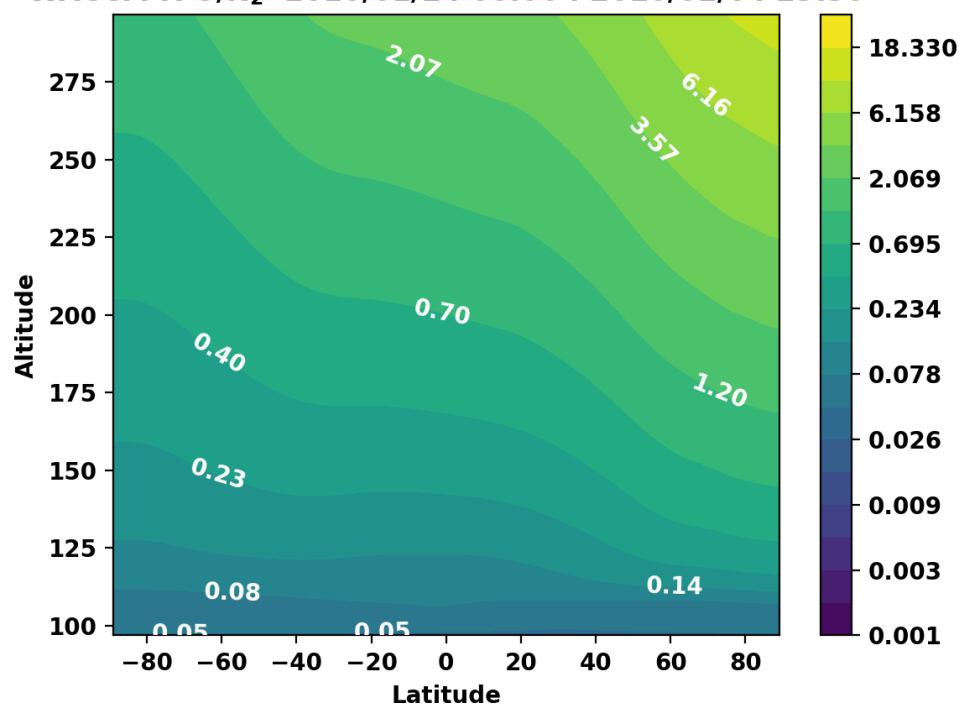
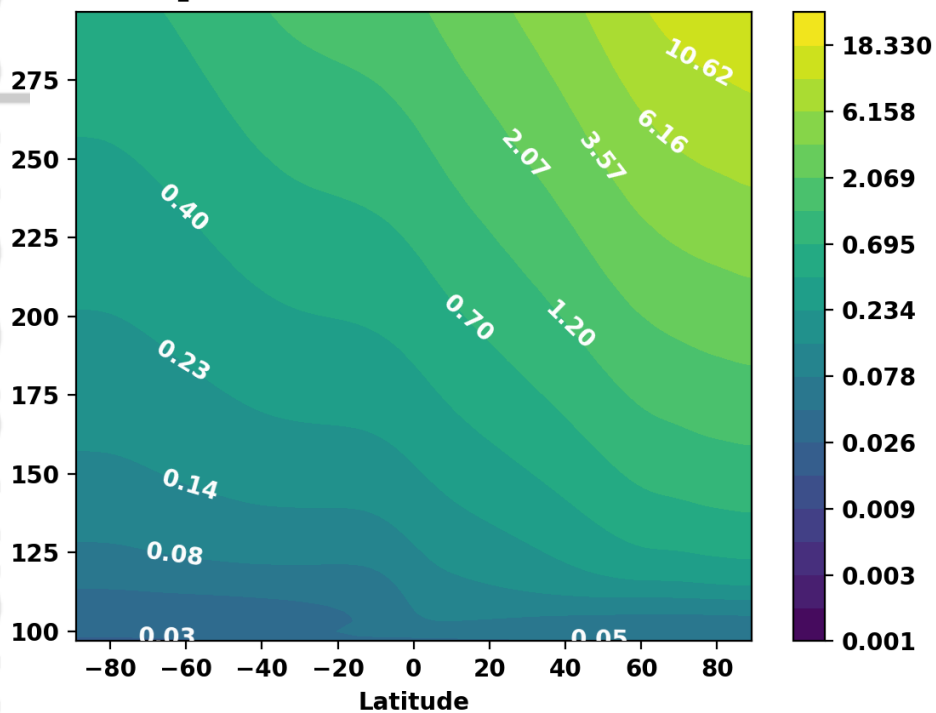
Author Manuscript

GITM w/ MSIS

GITM w/ WACCM-X

a) MSIS O/N₂ 2010/01/24 00:00 : 2010/02/04 23:30

b) WACCM-X O/N₂ 2010/01/24 00:00 : 2010/02/04 23:30



c) % Diff O/N₂ 2010/01/24 00:00 : 2010/02/04 23:30

Difference (b) - (a)

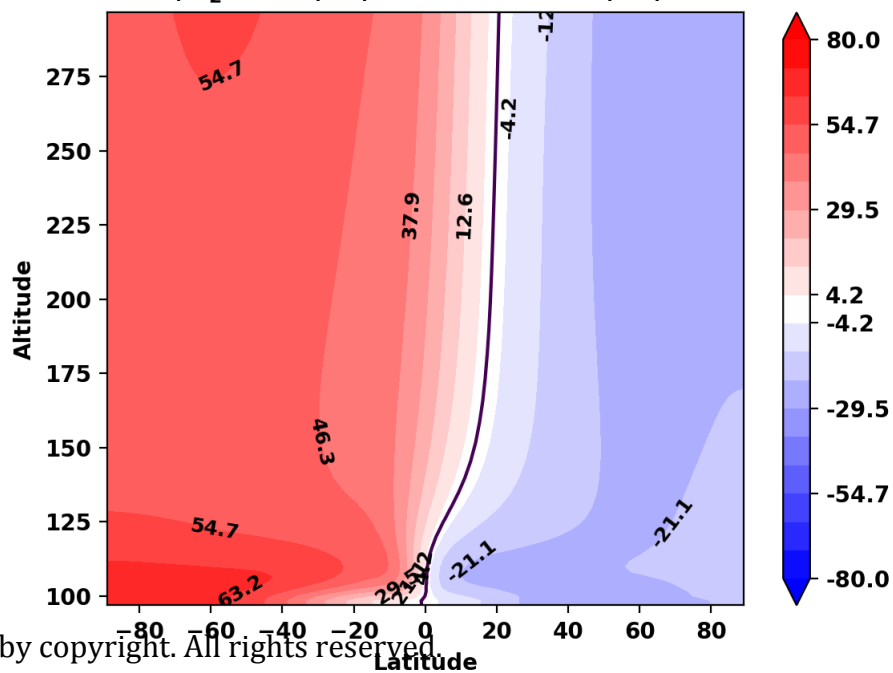
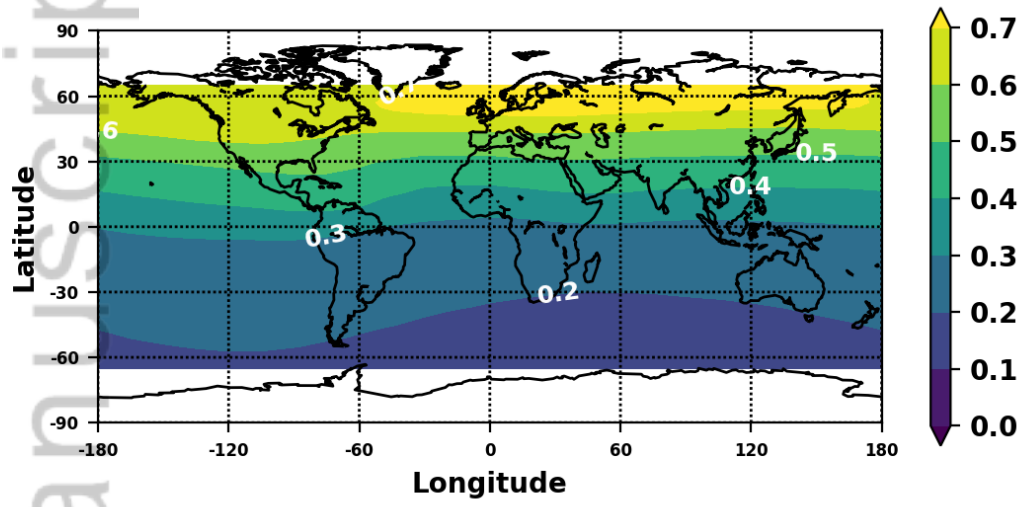


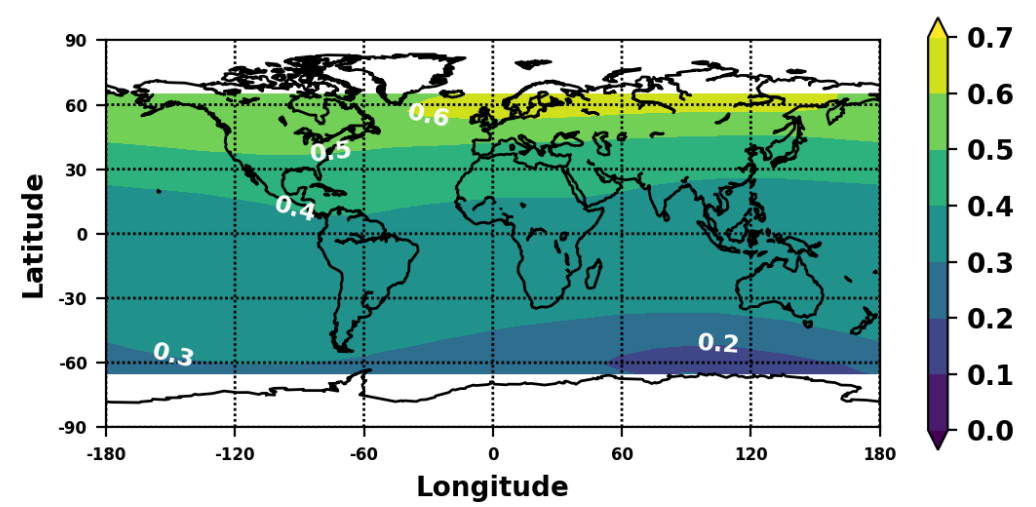
Figure 11.

Author Manuscript

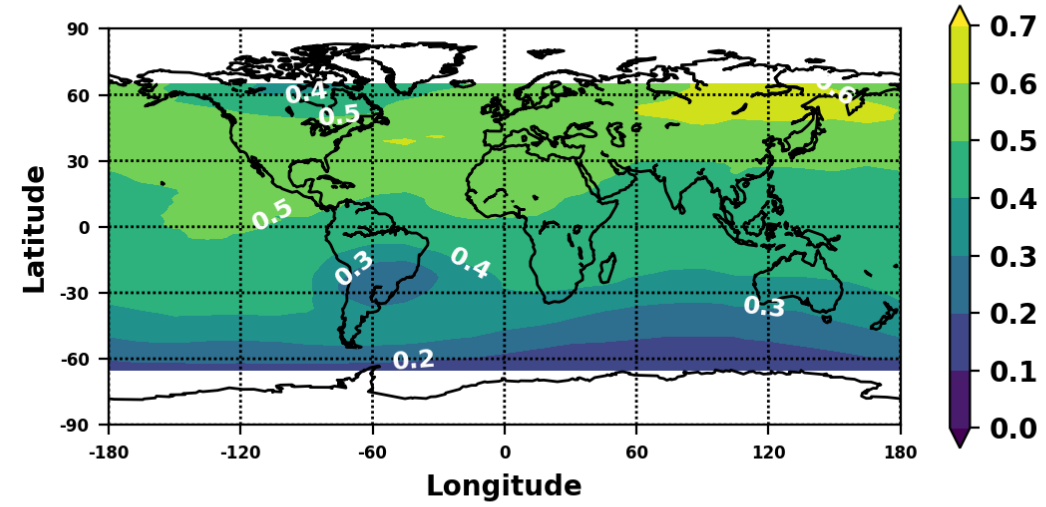
a) GITM w/ MSIS O/N₂ 2010-01-24 00:00 - 2010-02-04 23:30



b) GITM w/ WACCM-X O/N₂ 2010-01-24 00:00 - 2010-02-04 23:30



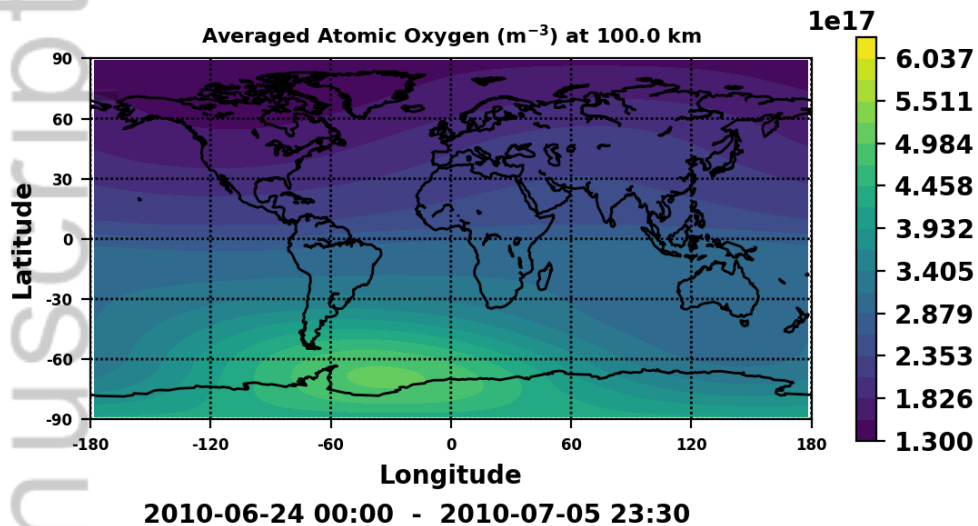
c) GUVI O/N₂ 2010-01-24 00:00 - 2010-02-04 23:30



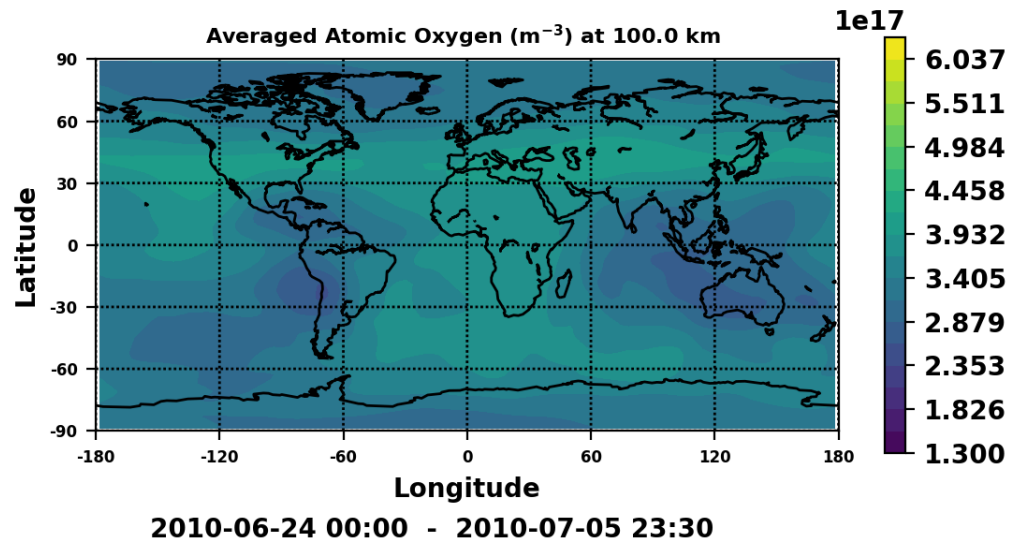
GITM w/ MSIS

GITM w/ WACCM-X

a)

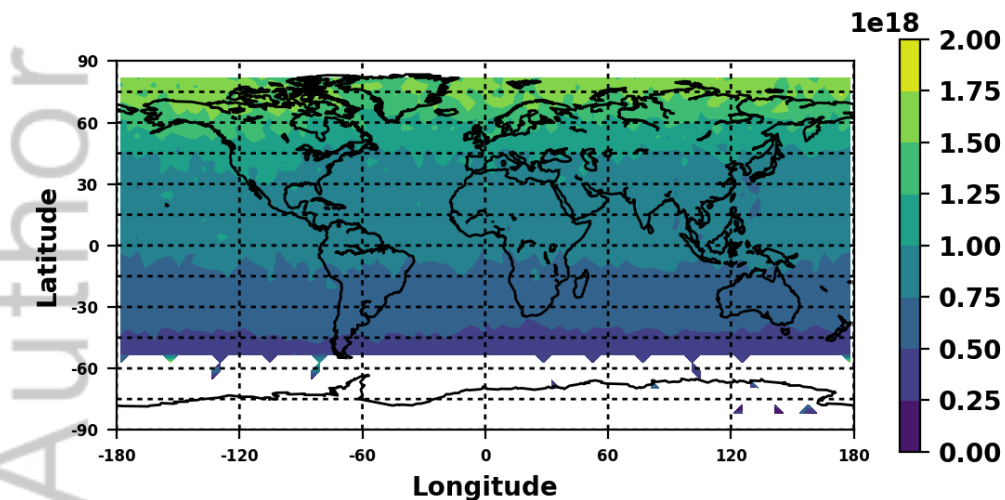


b)



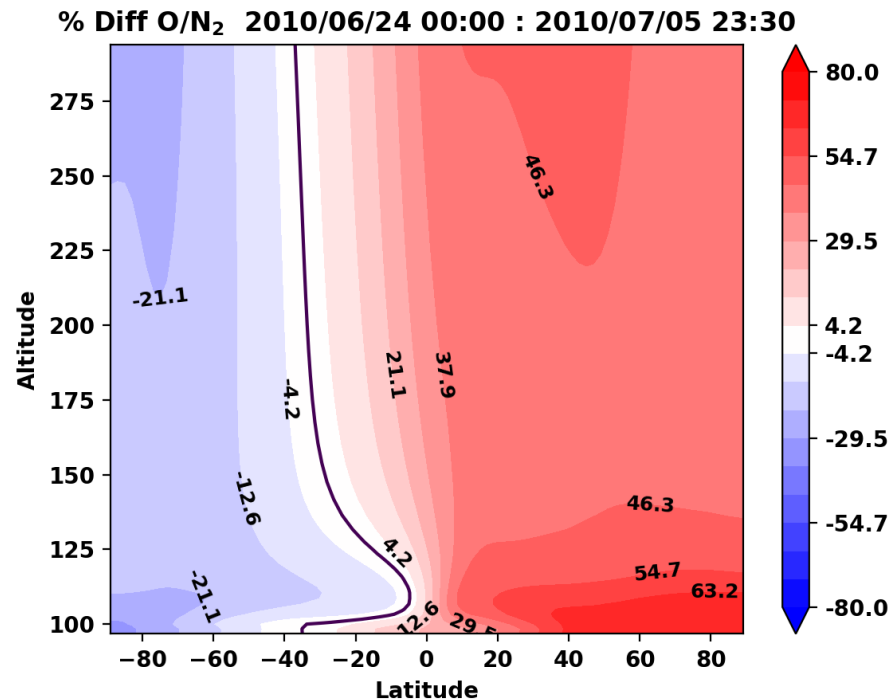
SABER Atomic Oxygen at 100 km June (2002-2017)

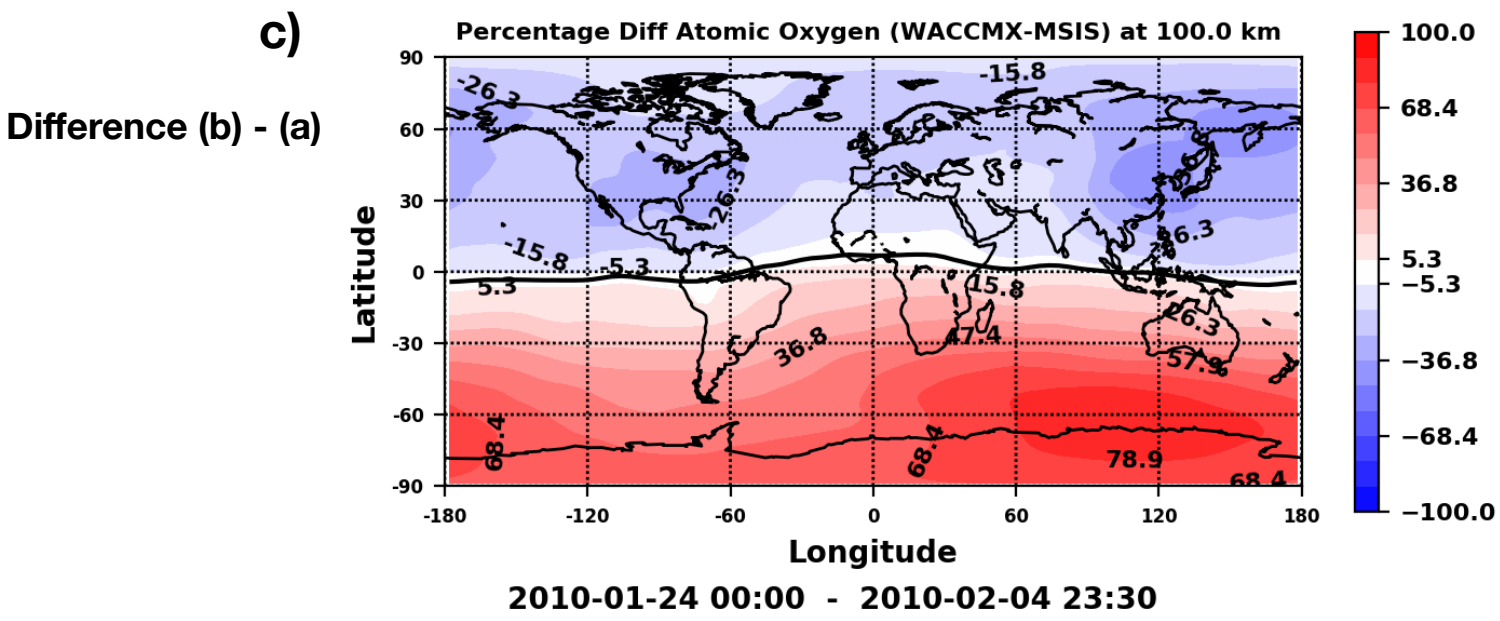
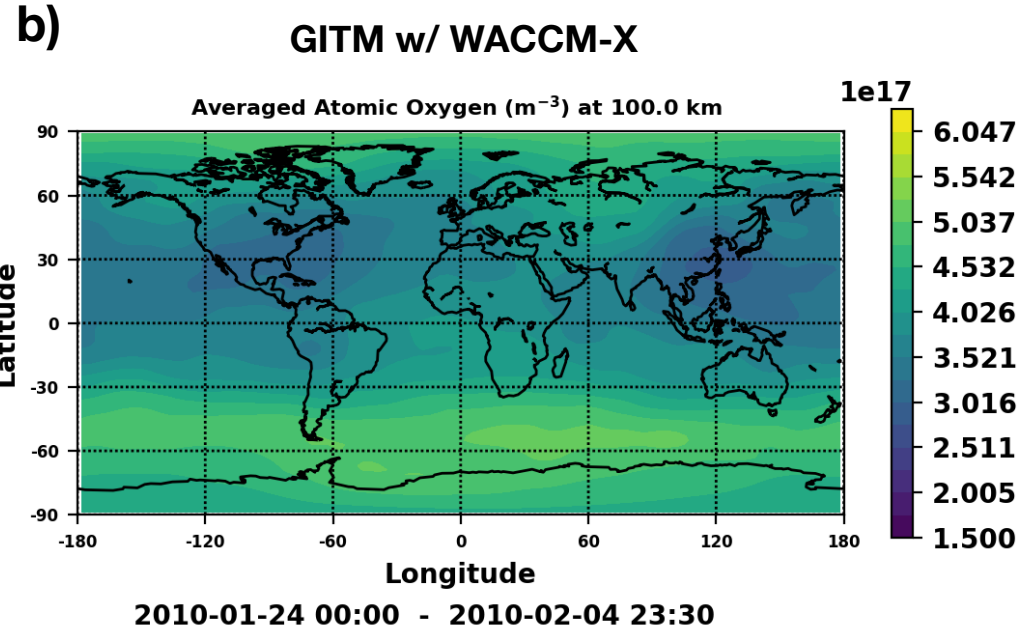
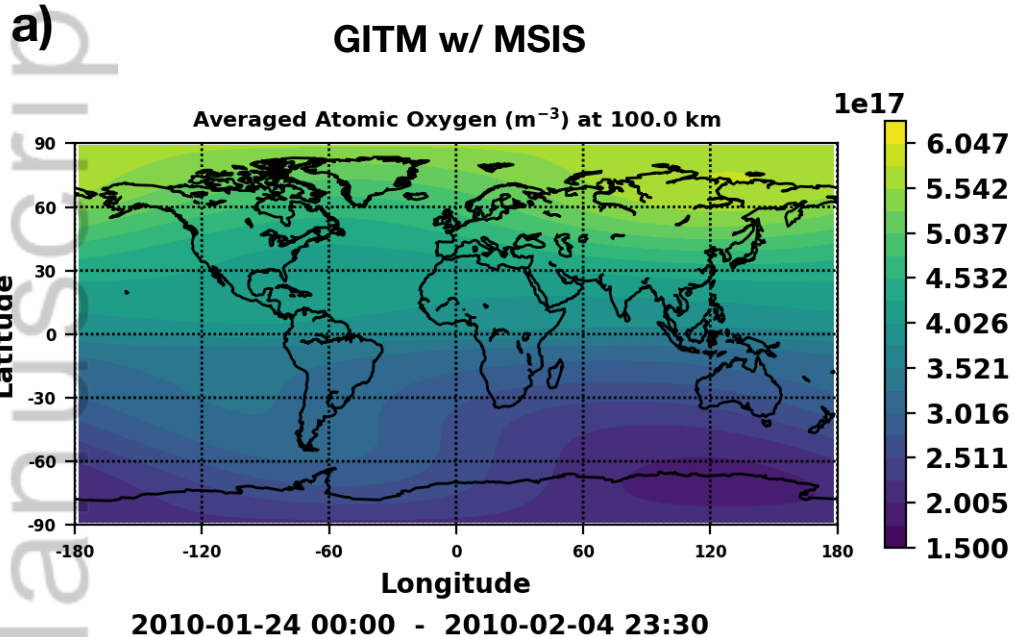
c)



Difference in O/N₂

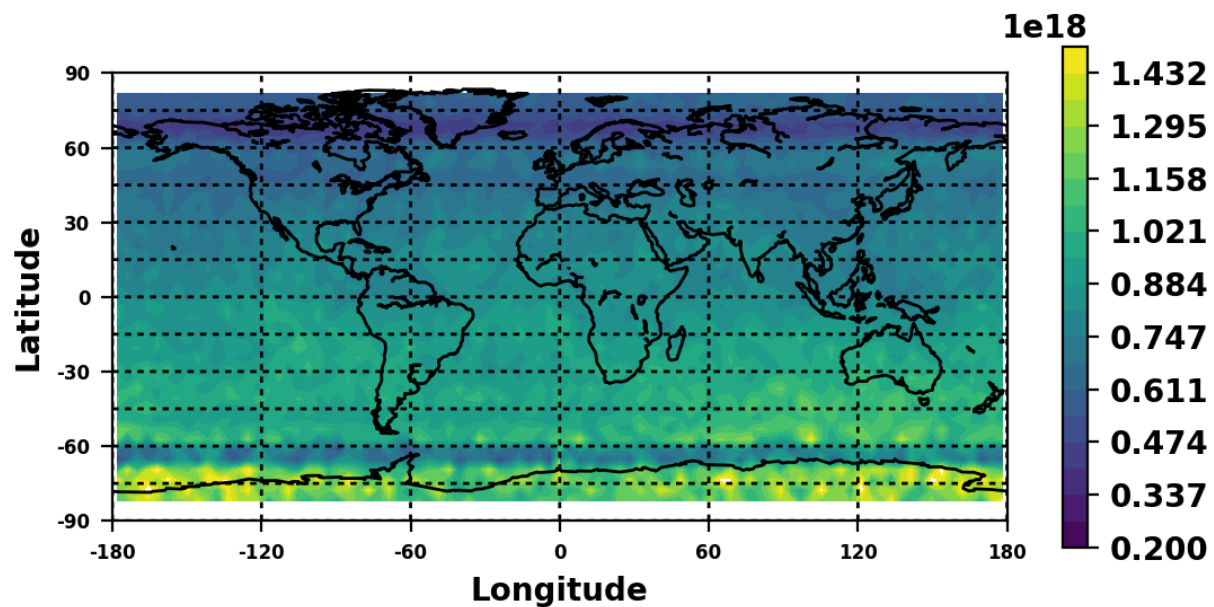
d)





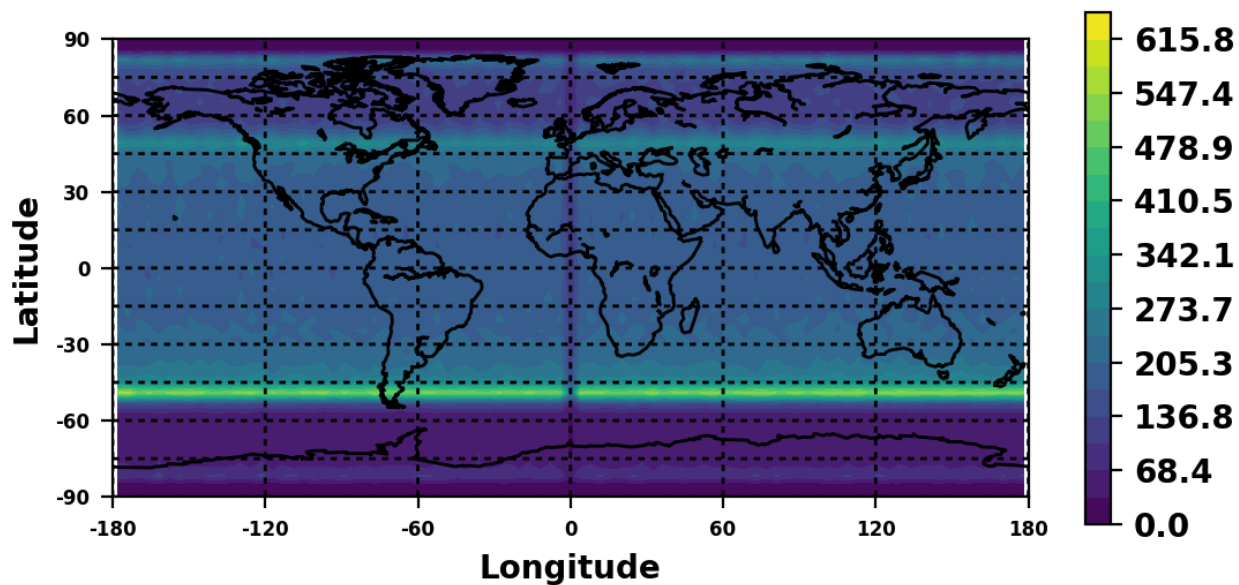
SABER Atomic Oxygen at 100 km Jan (2002-2017)

a)



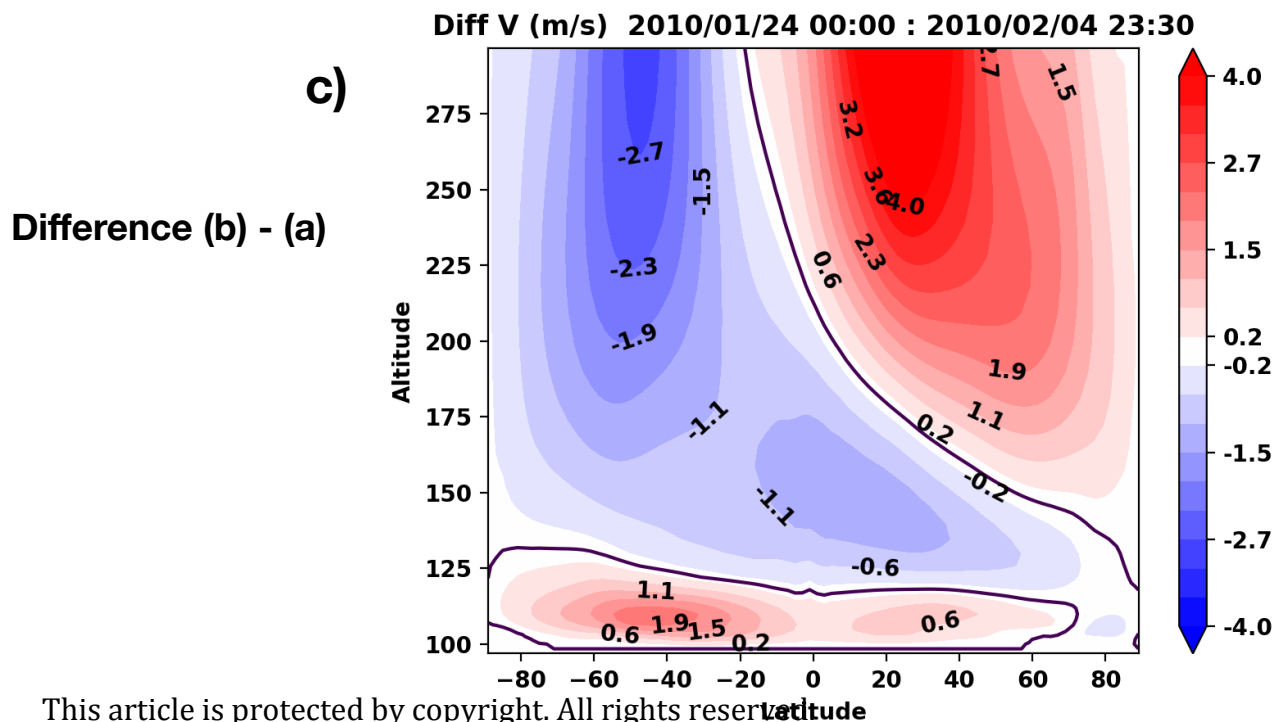
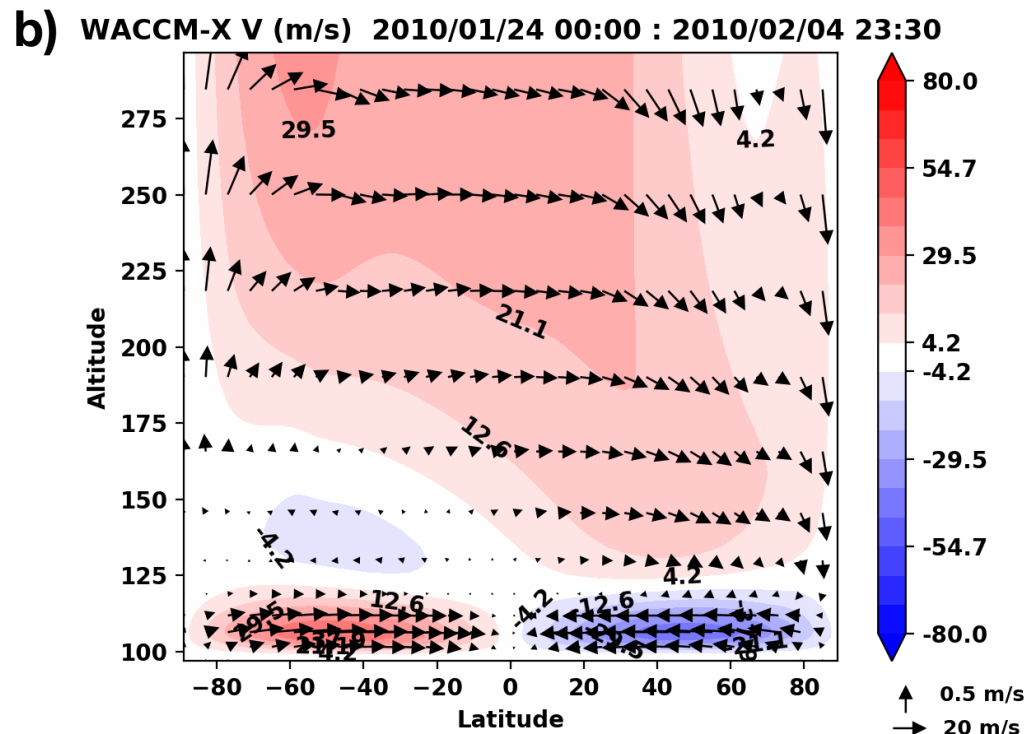
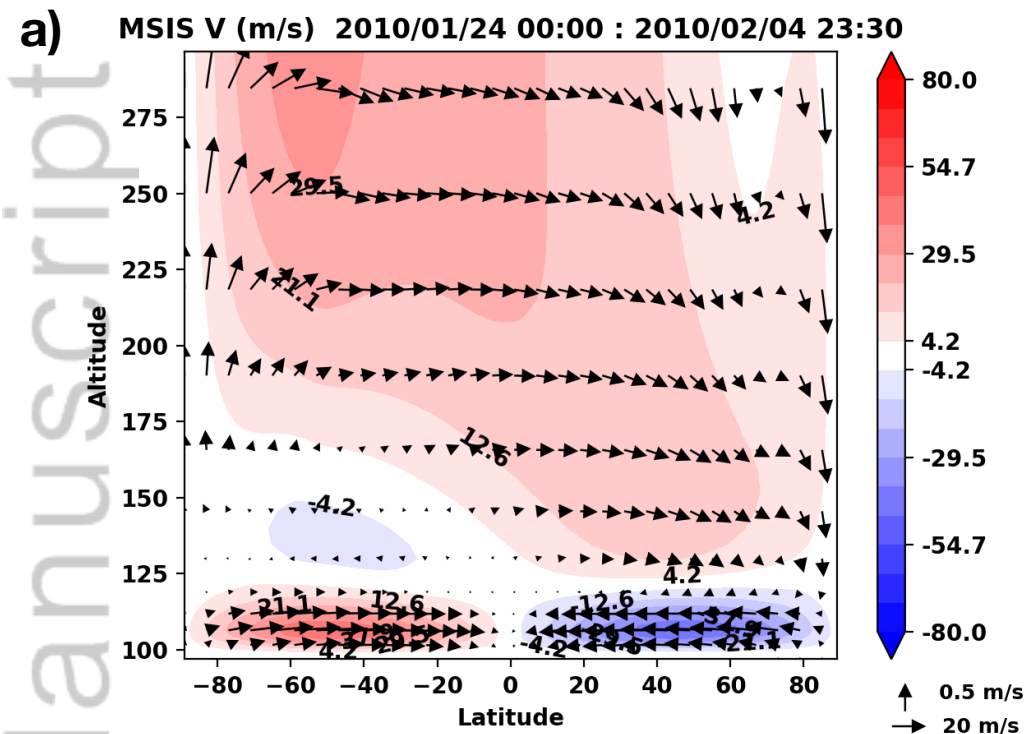
b)

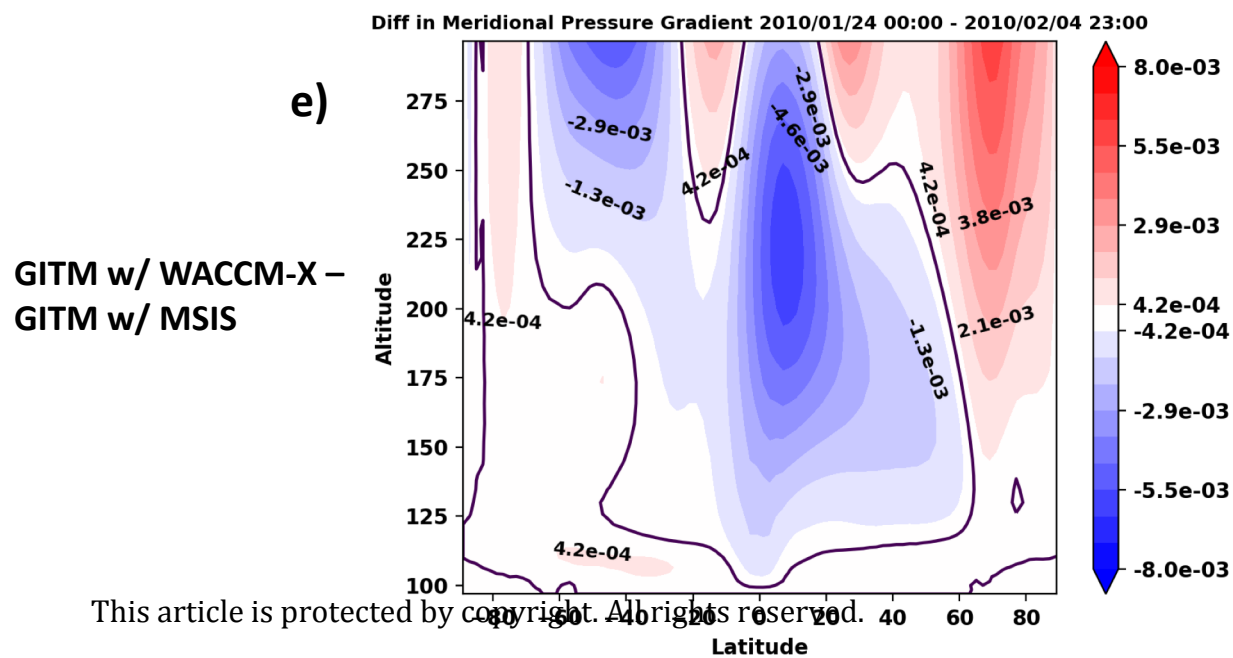
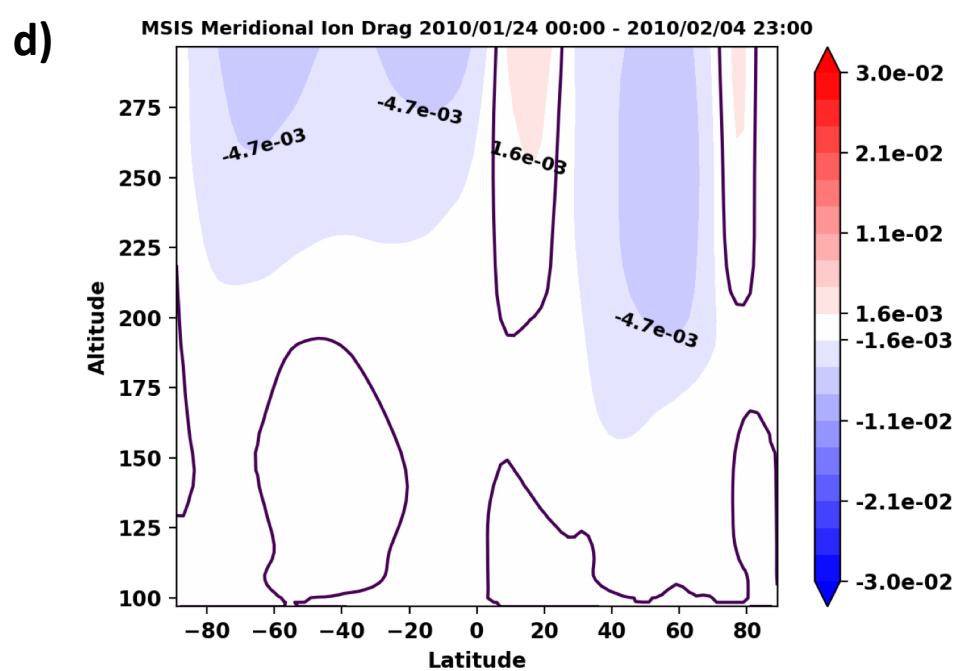
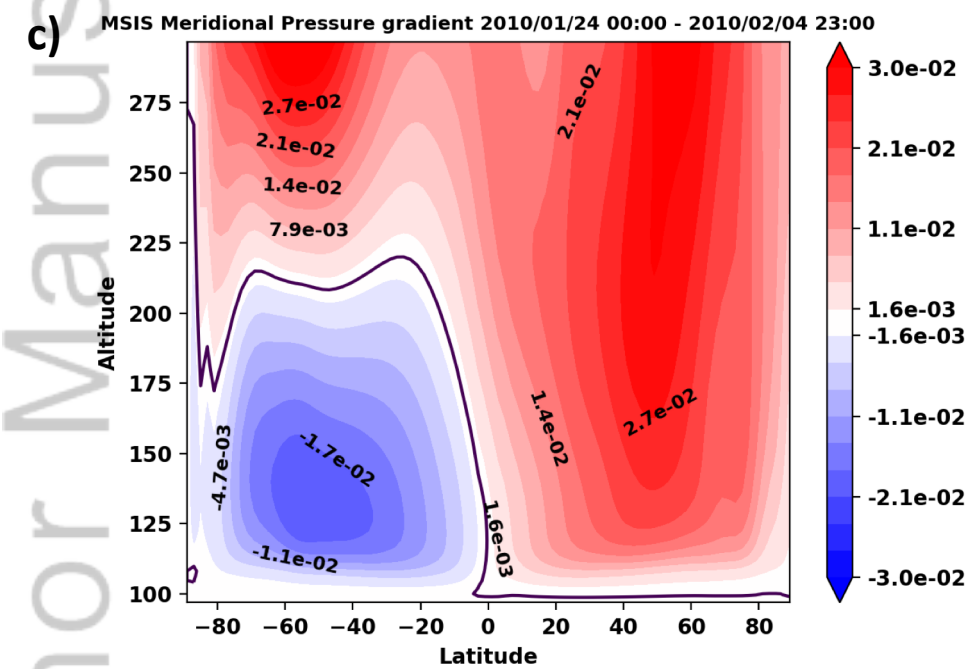
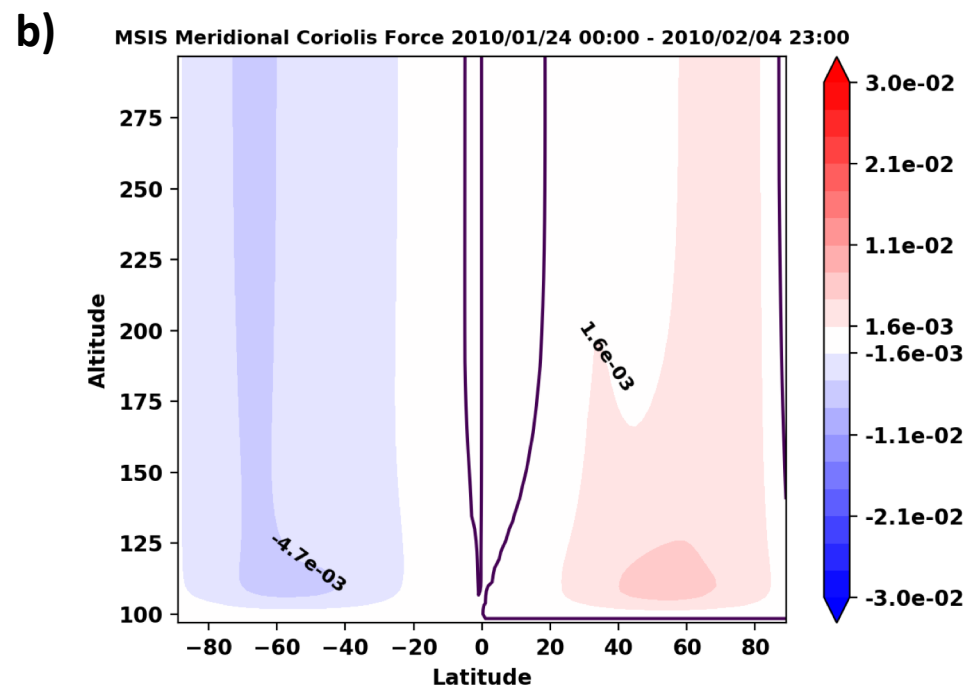
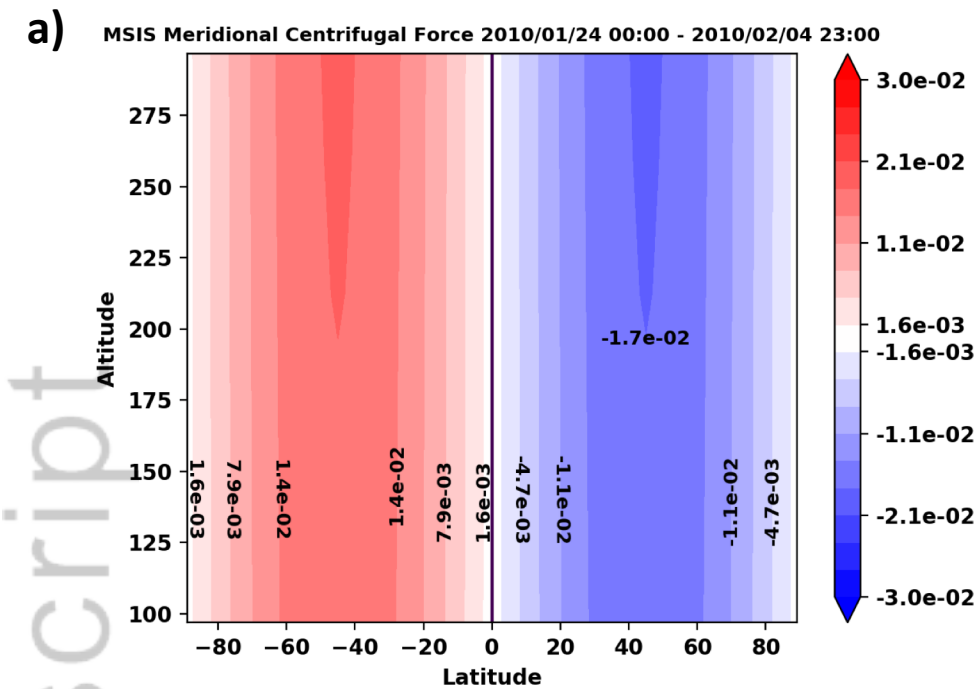
SABER Measurements Jan (2002-2017)



GITM w/ MSIS

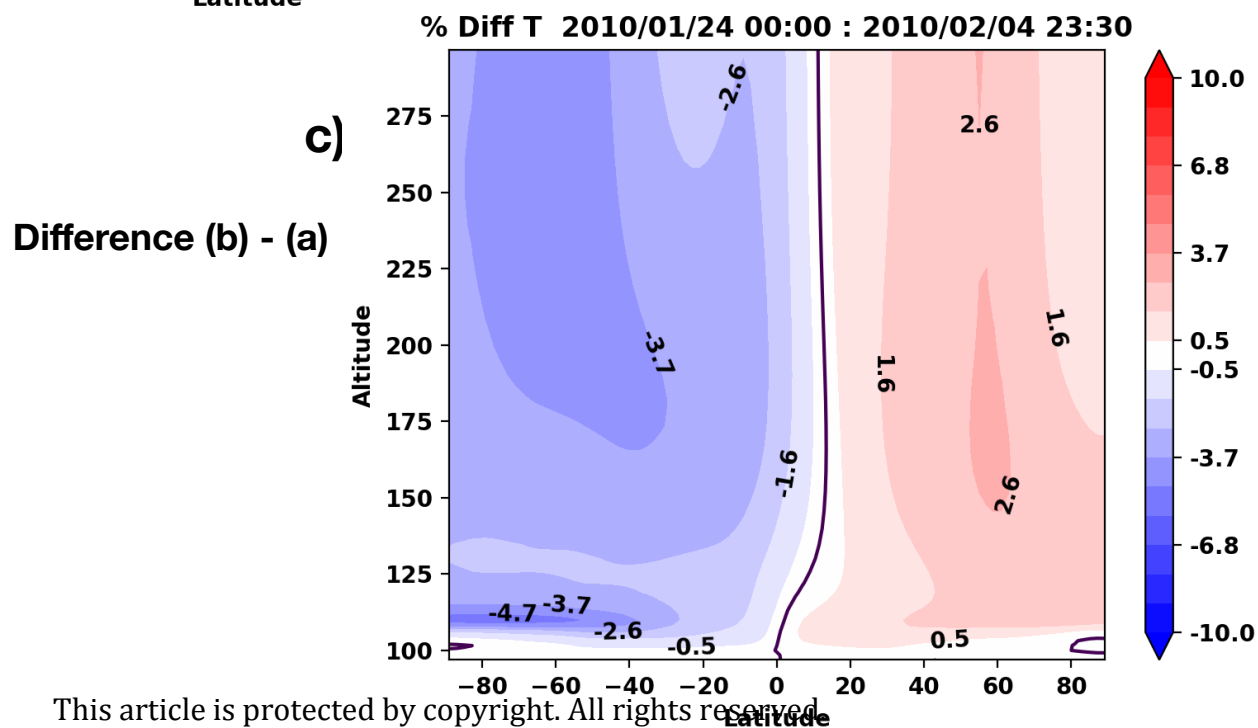
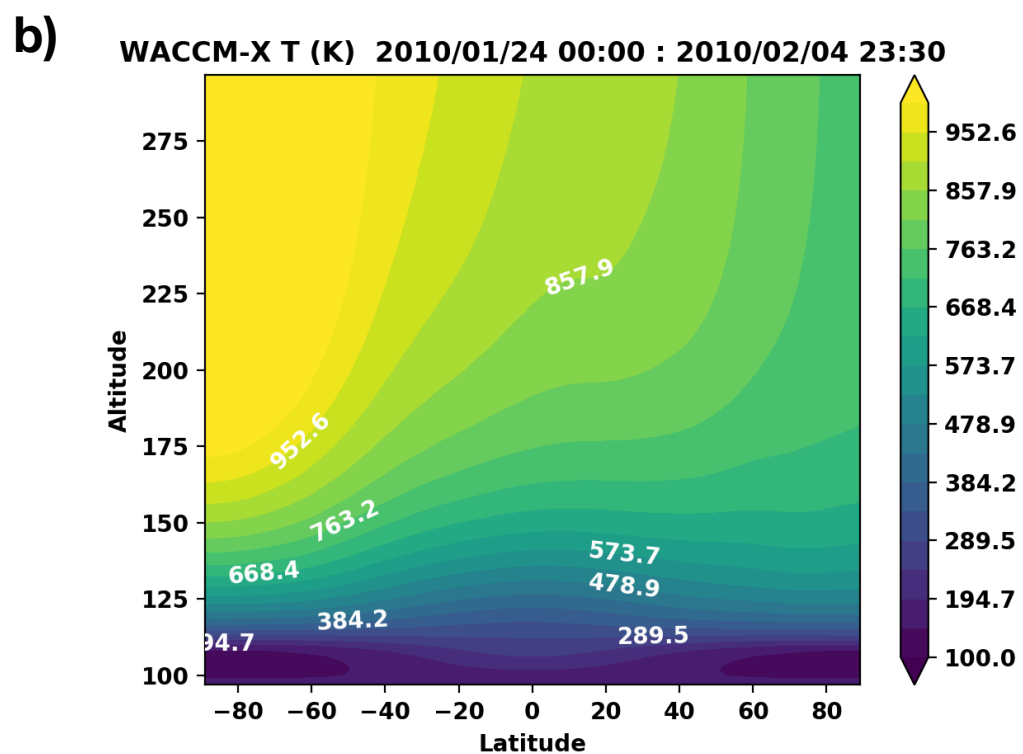
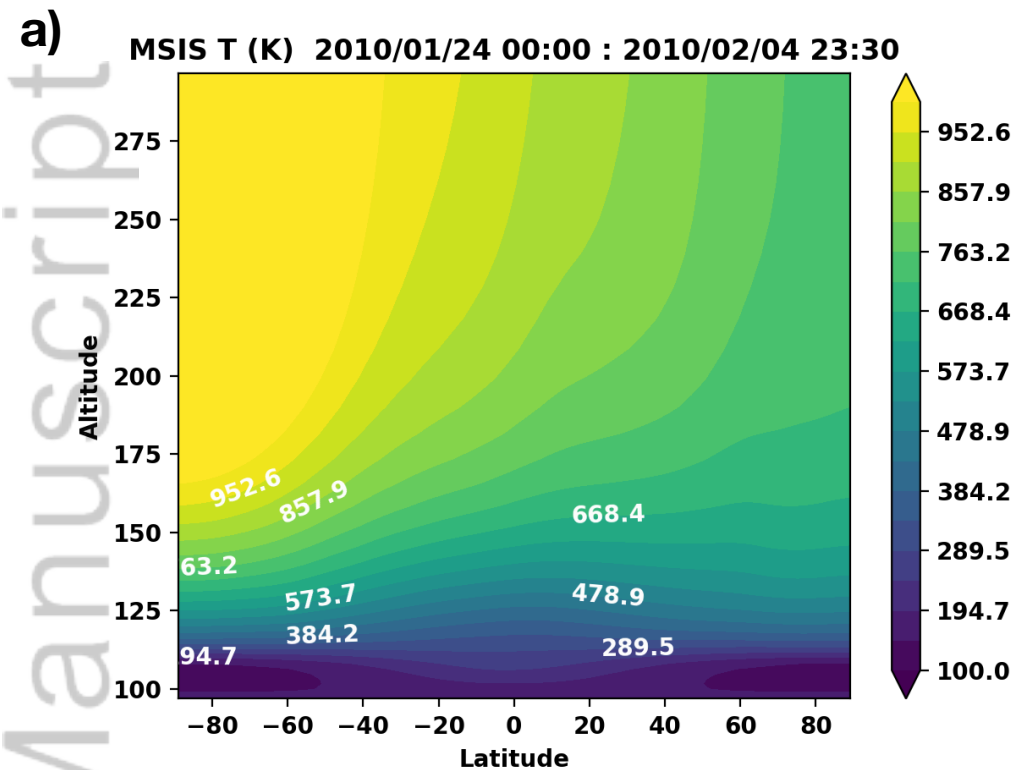
GITM w/ WACCM-X





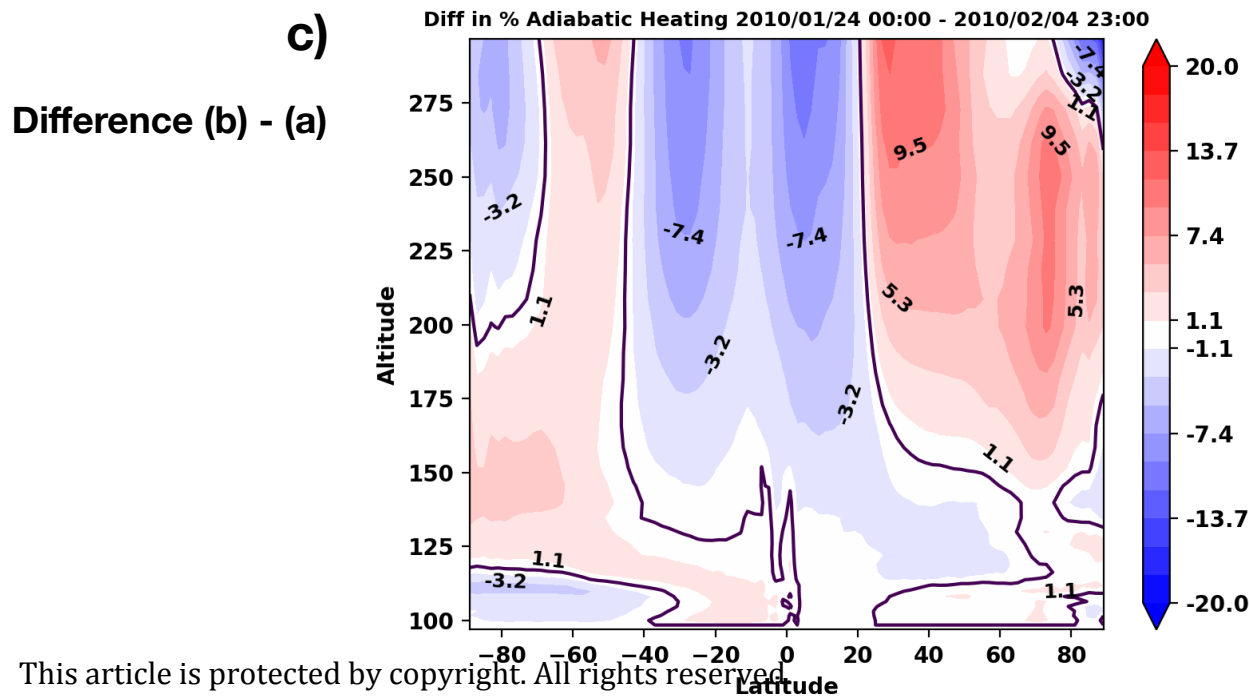
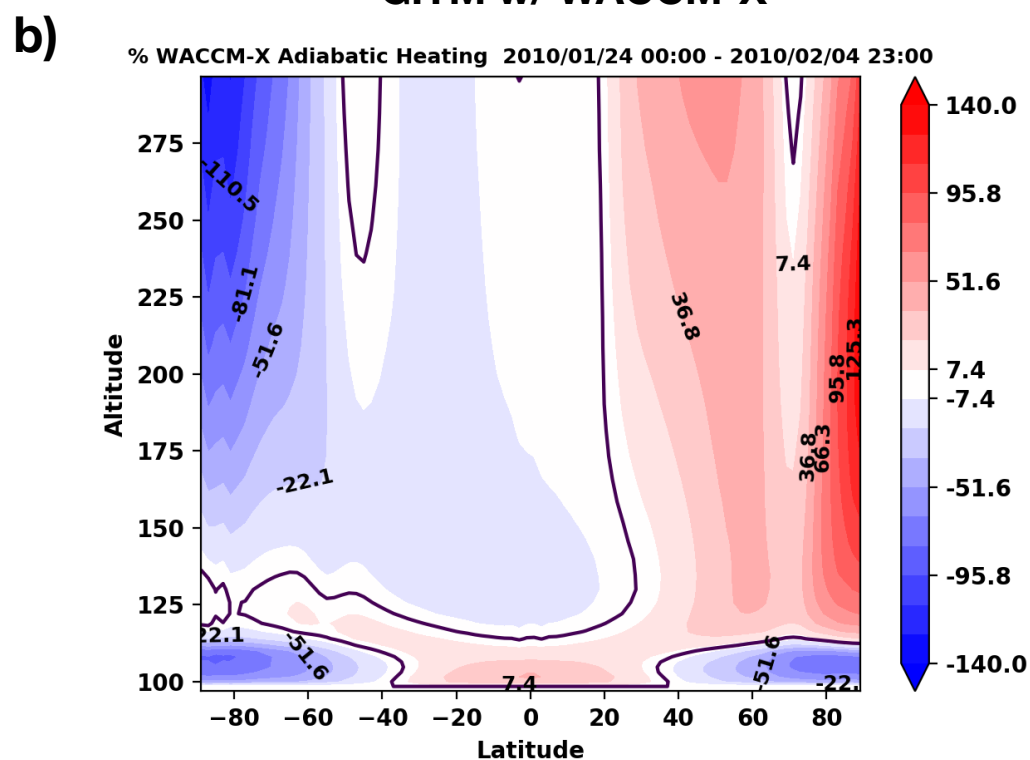
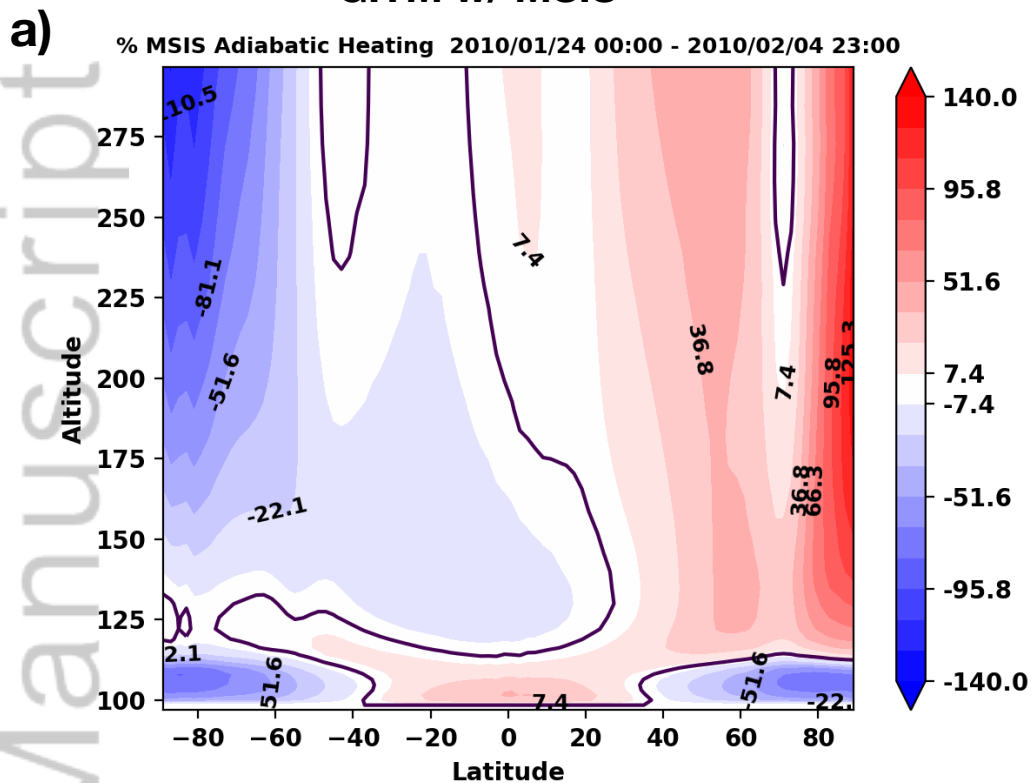
GITM w/ MSIS

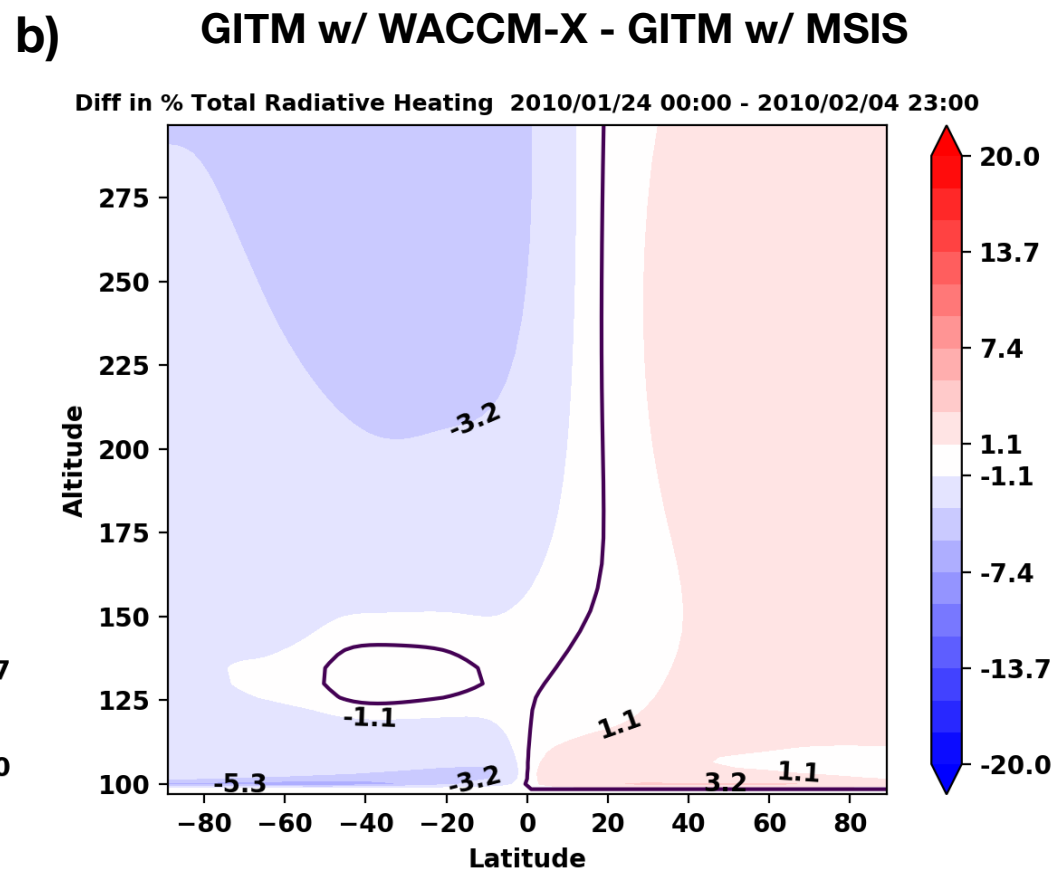
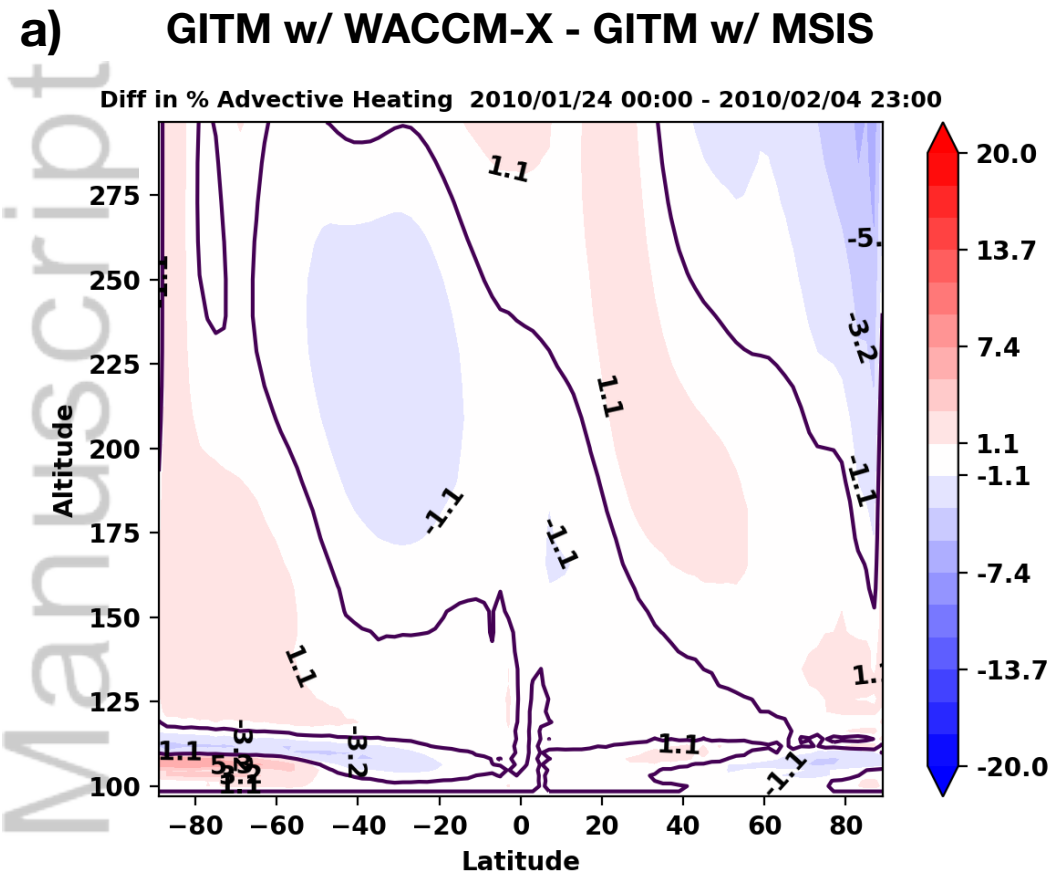
GITM w/ WACCM-X

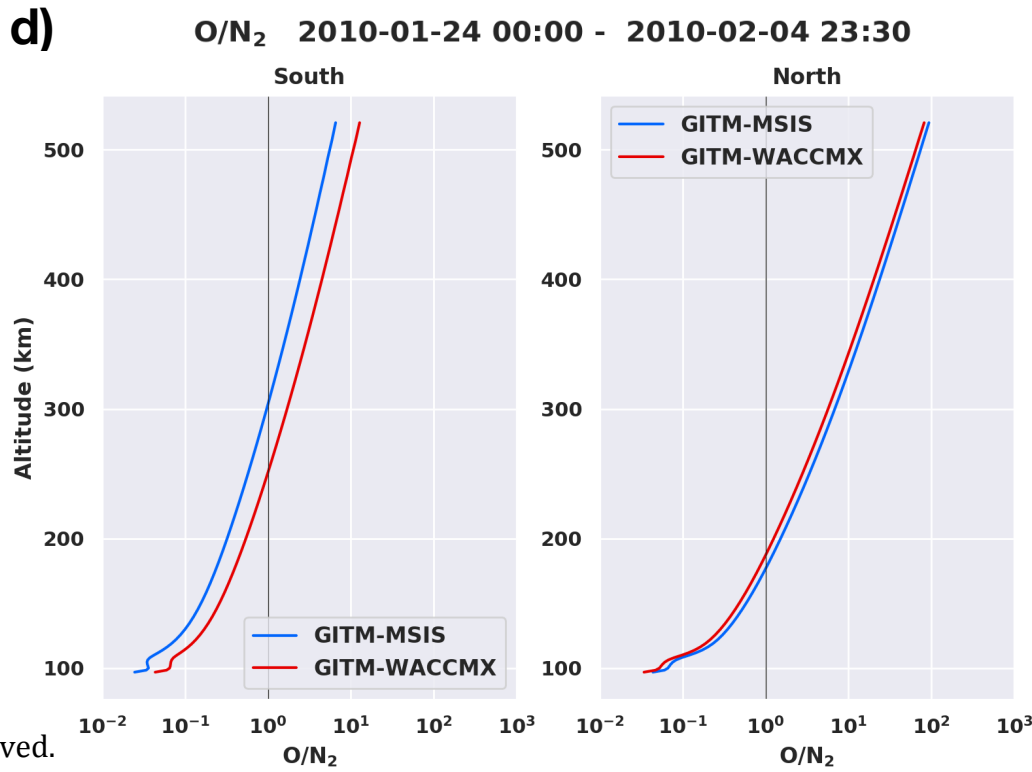
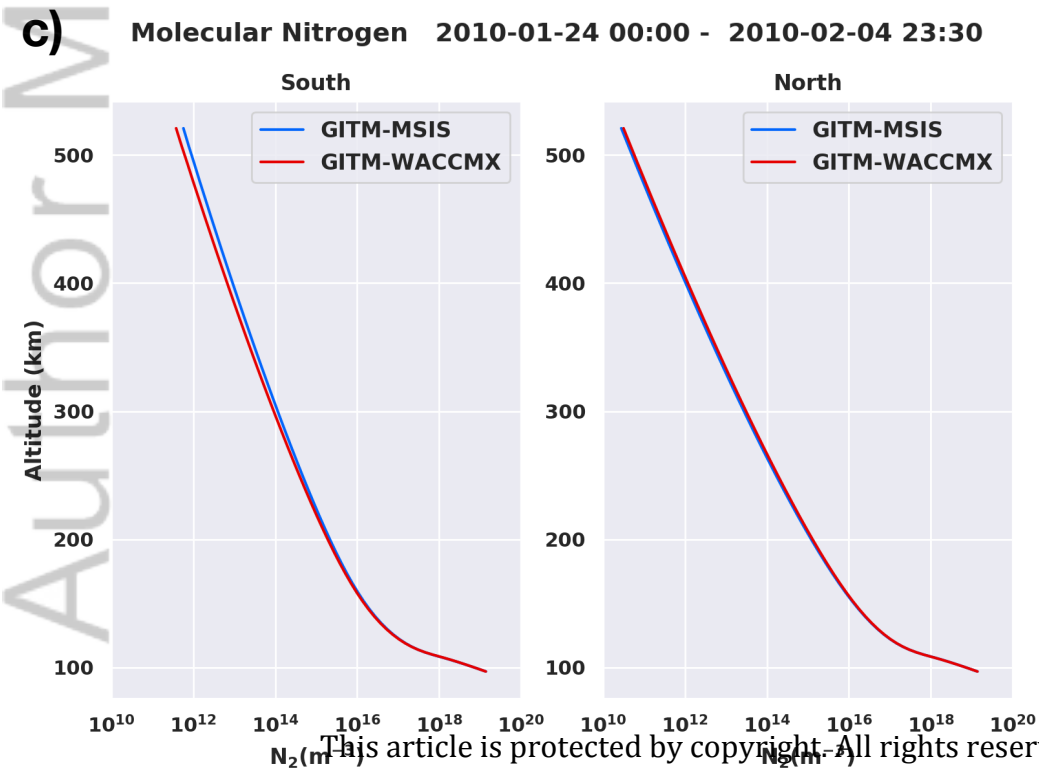
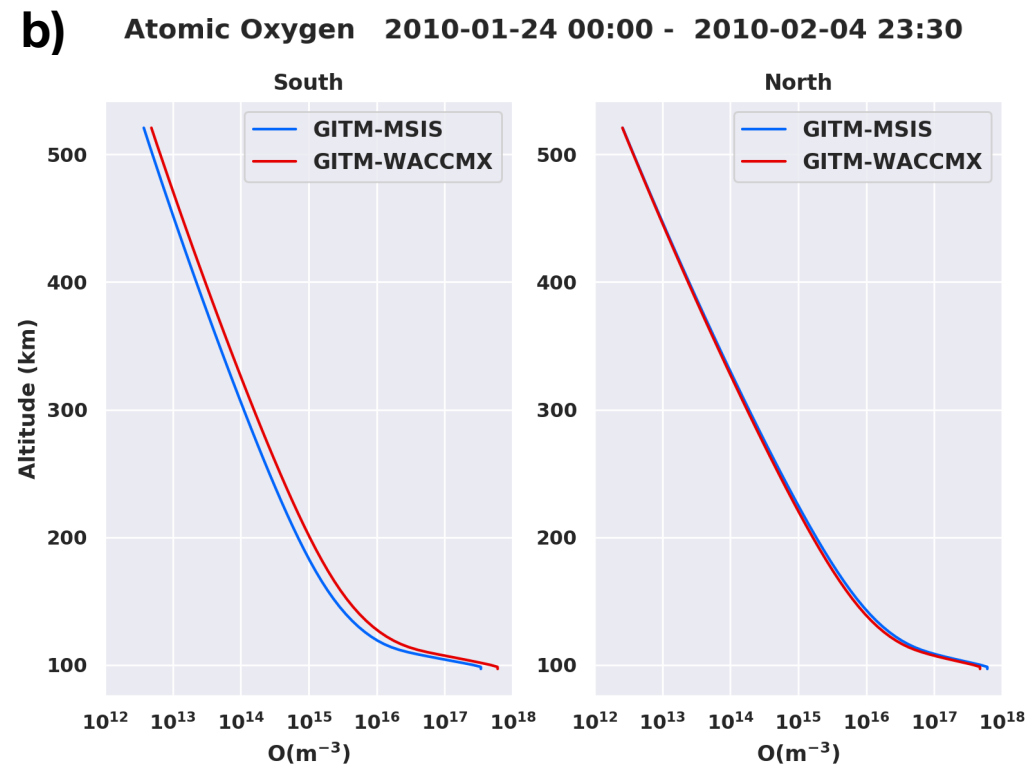
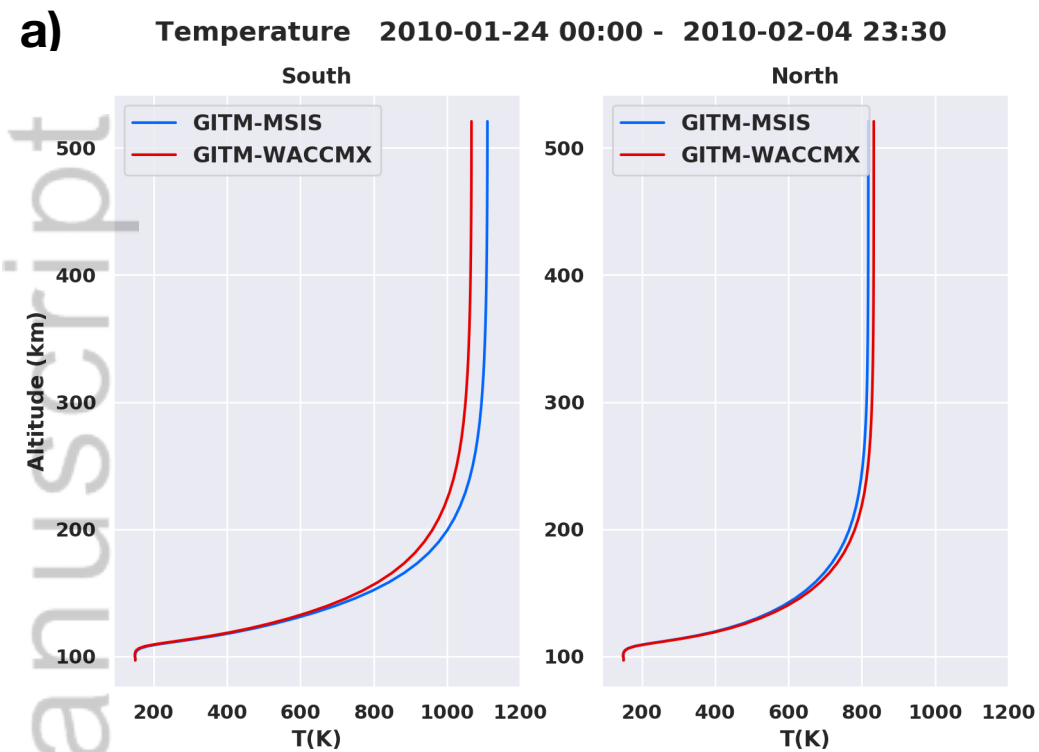


GITM w/ MSIS

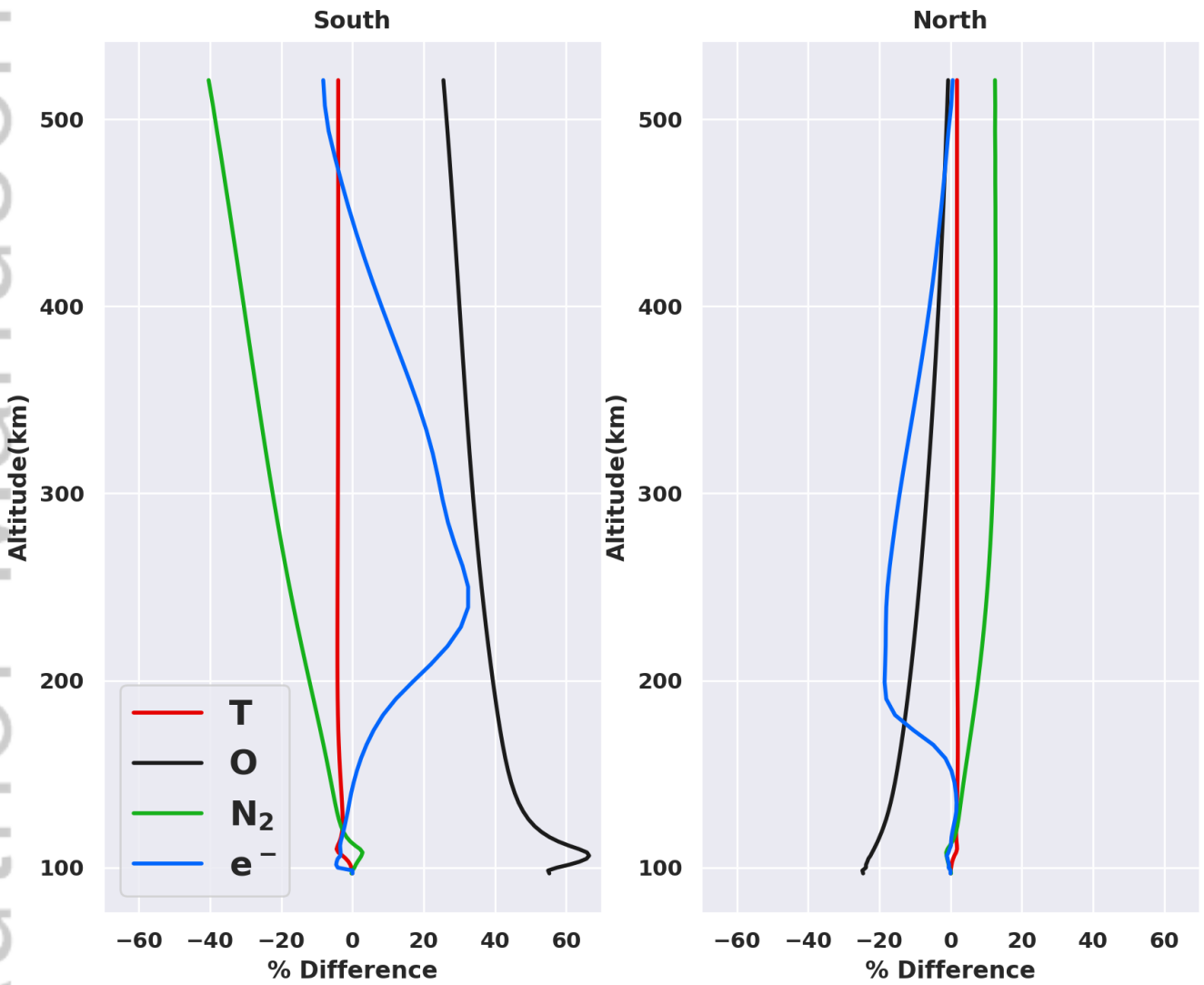
GITM w/ WACCM-X







Percentage Difference in Means (WACCMX-MSIS) 2010-01-24 00:00 - 2010-02-04 23:30



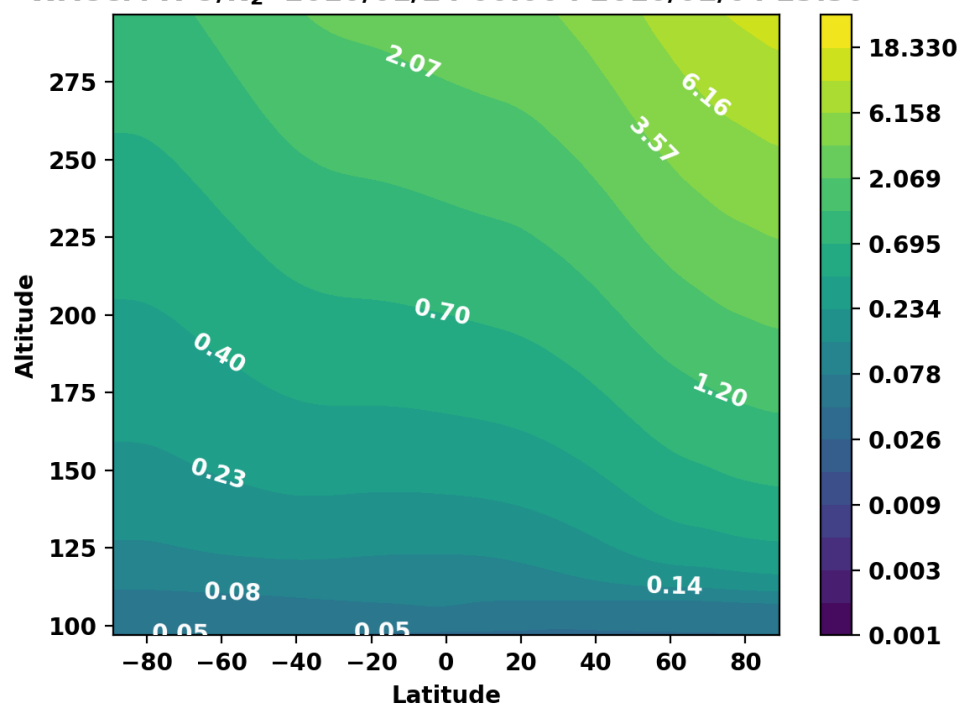
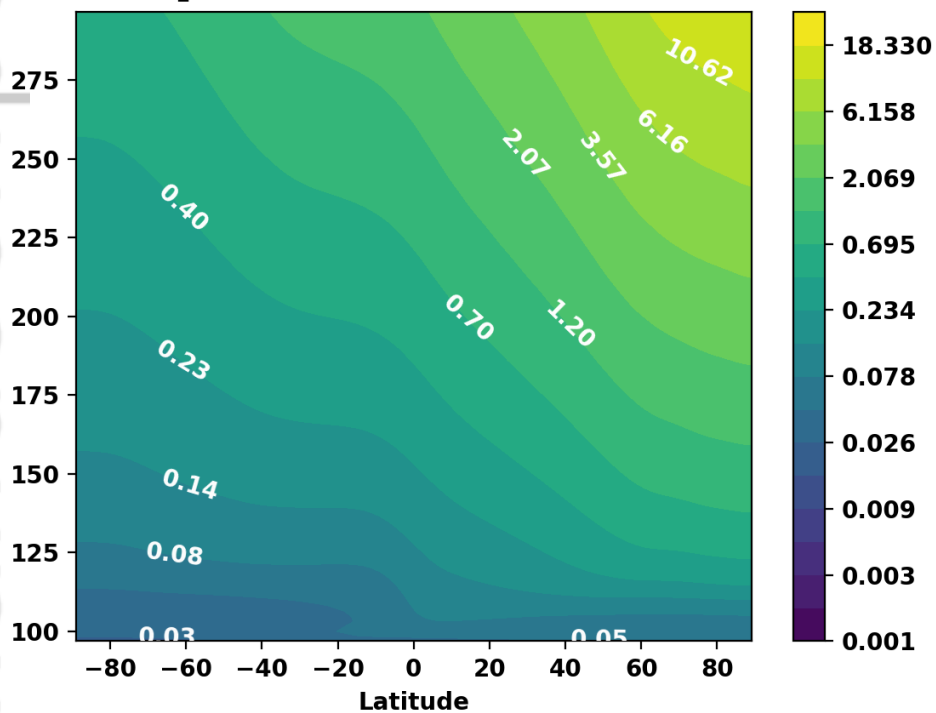
2020JA027877-f09-z-.png

GITM w/ MSIS

GITM w/ WACCM-X

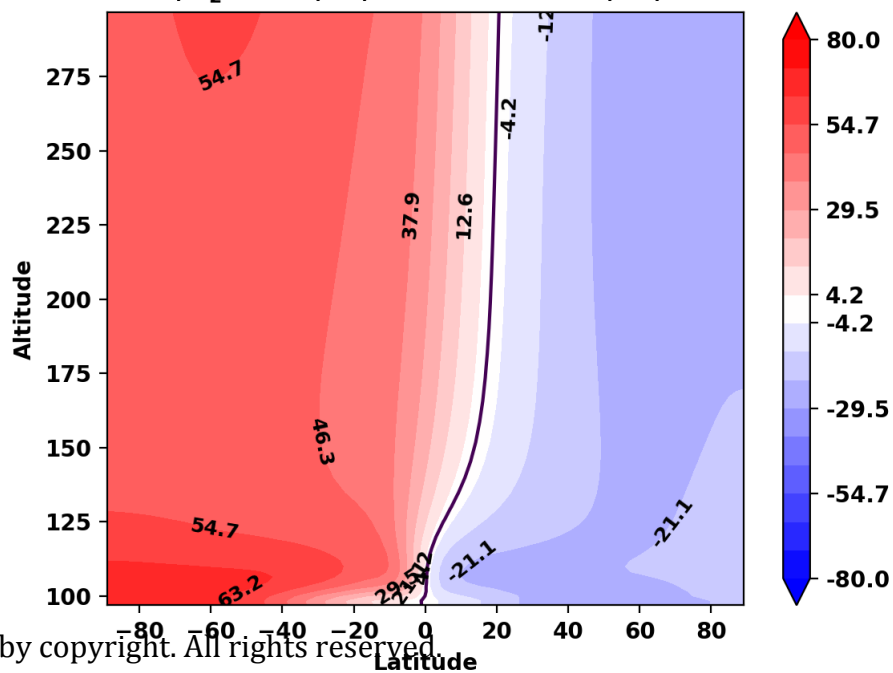
a) MSIS O/N₂ 2010/01/24 00:00 : 2010/02/04 23:30

b) WACCM-X O/N₂ 2010/01/24 00:00 : 2010/02/04 23:30

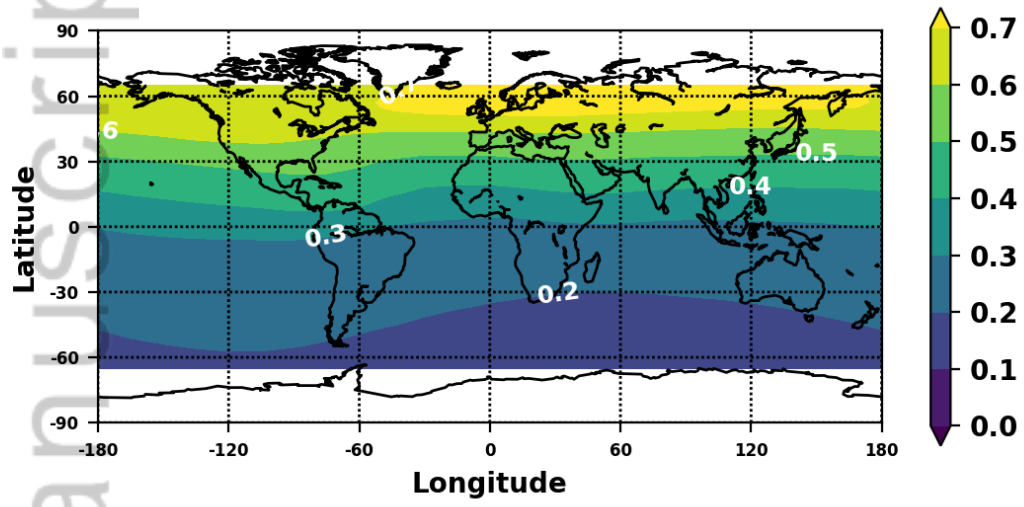


c) % Diff O/N₂ 2010/01/24 00:00 : 2010/02/04 23:30

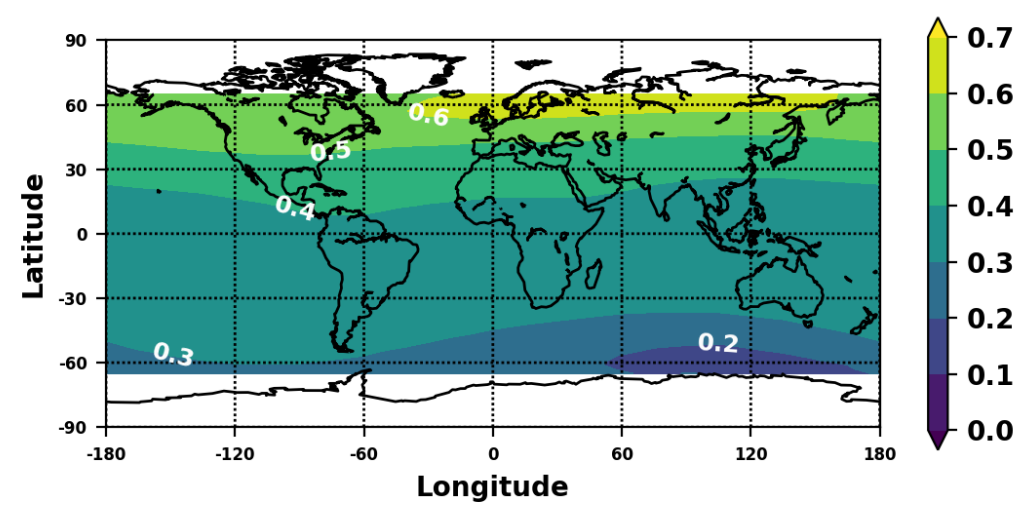
Difference (b) - (a)



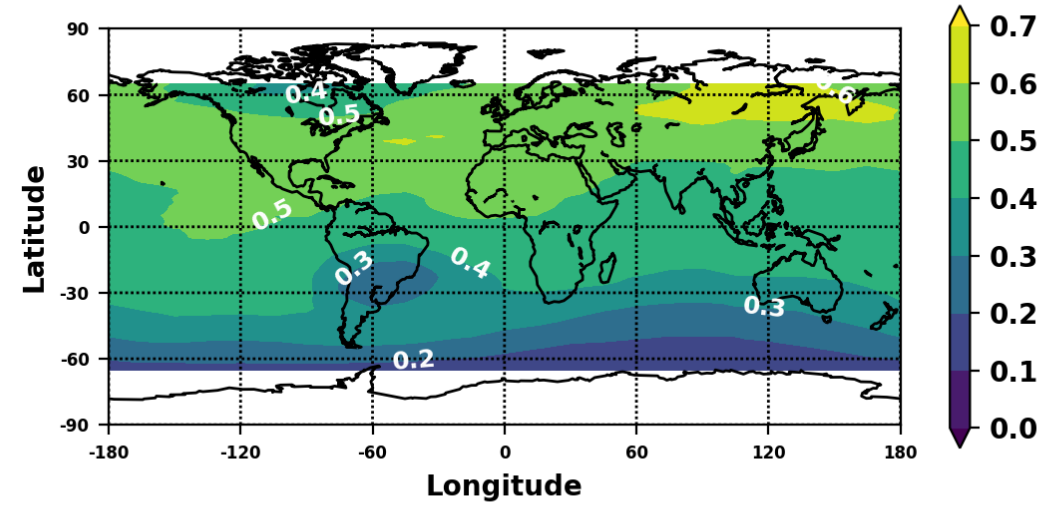
a) GITM w/ MSIS O/N₂ 2010-01-24 00:00 - 2010-02-04 23:30



b) GITM w/ WACCM-X O/N₂ 2010-01-24 00:00 - 2010-02-04 23:30



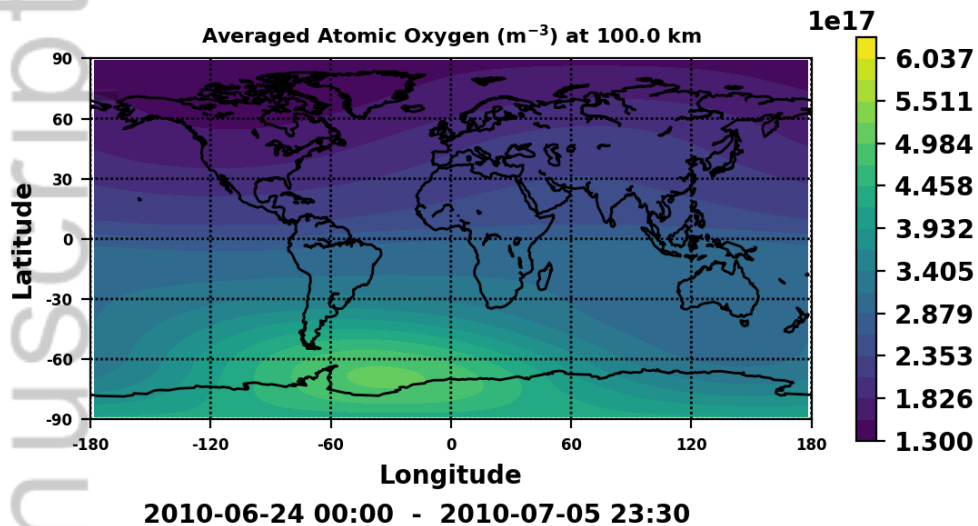
c) GUVI O/N₂ 2010-01-24 00:00 - 2010-02-04 23:30



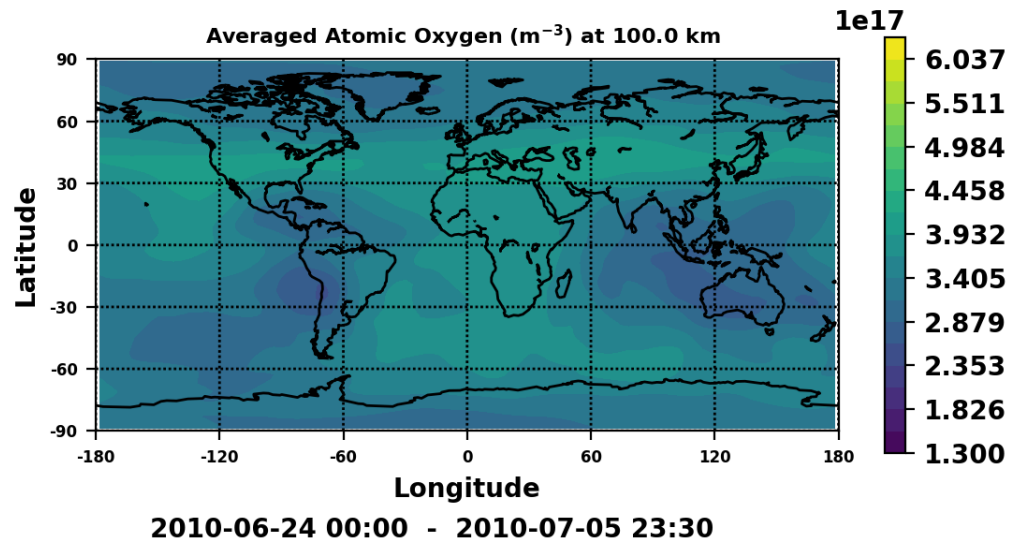
GITM w/ MSIS

GITM w/ WACCM-X

a)

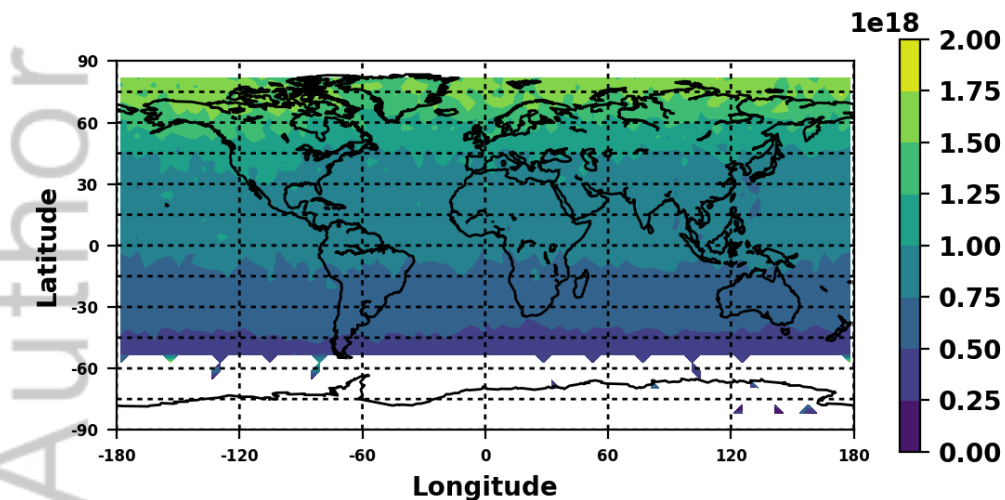


b)



SABER Atomic Oxygen at 100 km June (2002-2017)

c)



Difference in O/N₂

d)

